TIME AND FREQUENCY RESOLVED PHOTOCONDUCTIVITY STUDIES ON AMORPHOUS SEMICONDUCTORS

A thesis presented by
Dennis Patrick Webb (M.Sc.)
to the University of Abertay, Dundee
(collaborating establishment: the Department of Engineering, University of Cambridge)
in partial fulfilment of the requirements
for the degree of Doctor of Philosophy
October 1994

I certify that this thesis is the true and accurate version of the thesis approved by the examiners.

Signed [redacted] Date 23.5.95

(Director of Studies)

A.M.D.G.

To my parents, with love,
and in memory of T.C.Myers

Acknowledgements

I would like to thank my supervisors Dr Charlie Main and Dr Steve Reynolds for their constant support, advice, generosity with their time, enthusiasm and repeated explanations of simple analogue circuit theory. I would also like to thank my external supervisor Dr W.Milne.

Thanks are also due to the following:

The Department of Electronic and Electrical Engineering, University of Abertay, Dundee,

The technical staff of the department of Electronic and Electrical Engineering,

Professor W.Bloss and staff of the I.P.E. Universität Stuttgart for provision and characterisation of samples, and for hospitality during my visit,

Dr Rudi Brüggemann for friendship and hospitality,

Dr G.Adriaenssens for providing the a-As_2Se_3 samples,

The late Science and Engineering Research Council for provision of a research studentship.

Finally I would like to thank Wei Gao and his predecessor Dr Colin Soutar for friendship and being congenial people with whom to share a laboratory.

Statement of Objectives

The objectives pursued in the course of this work were:

(i) To investigate the photoconductive properties of amorphous materials by means of experimental measurements of photoconductivity of thin films of the materials in both time and frequency domains.

(ii) To elucidate the above properties in terms of photocarrier transport, trapping and recombination kinetics.

(iii) To use the understanding thus obtained to develop a spectroscopy of the density of localised states in the mobility gap.

(iv) To carry out complementary computer modelling of electronic processes in amorphous materials in support of the above.

TIME AND FREQUENCY RESOLVED PHOTOCONDUCTIVITY STUDIES ON AMORPHOUS SEMICONDUCTORS

Patrick Webb

Time and frequency domain photoconductivity experiments and analysis assuming the multiple trapping transport model are used in a complementary fashion to investigate the density of states (DOS) and associated trapping and recombination parameters of amorphous semiconductors. The solution of the linearised multiple trapping rate equations is straightforward in the frequency domain, and it is simple to invert the modulated photoconductivity (MPC) response to obtain an accurate DOS. It is proposed that a novel, wide energy range, accurate DOS probe is realisable by applying the Frequency domain inversion to the Fourier transform of *transient* photoconductivity (TPC) data. A numerical Fourier integral procedure appropriate to the nature of TPC data sets is described and tested.

Application of the Fourier transform method to TPC measurements on undoped a-Si:H produces a calculated DOS distribution covering half the mobility gap. The DOS consists of an 0.03 eV exponential band-tail, and a bump of $4.4\times10^{16}cm^{-3}$ states at 0.65eV below E_c, attributed to dangling bonds. The method detects the bump despite there being no related emission feature in the TPC decay. The accuracy of the calculated DOS is demonstrated to depend on the size of the missing contribution to the Fourier integral from the signal at times shorter than the experimentally observed minimum.

An *undershoot* or sign reversal of TPC measured with optical bias on undoped a-Si:H for steady state generation rate $G_{ss}\geq10^{18}cm^{-3}s^{-1}$ is observed at a time t_{us} which varies inversely and sublinearly with G_{ss}. From the linearised frequency domain analysis such an undershoot is expected for bimolecular recombination and recombination coefficient $C_R>C_n$, the band-tail trapping coefficient. The analysis predicts a related sign reversal in the imaginary part of the *Fourier transform* spectrum at a frequency $\omega_- \propto C_R$, which is also observed. Values for C_R mostly in the range $1\text{-}3\times10^{-8}cm^3s^{-1}$ are calculated.

Undoped a-Si:H MPC spectra exhibit a *phase peak* at a frequency ω_{peak} which varies superlinearly with G_{ss}. The phase peak accompanies a transition in the MPC response from DOS dependent to DOS independent behaviour for $\omega<\omega_{peak}$, in which régime the calculated DOS varies as $\omega^{0.43}$. For a DOS consisting of a single trap species it is expected that the transition frequency be around 100× smaller than observed and the calculated DOS be proportional to ω at low frequency. Assigning a trapping coefficient of $10\text{-}100C_n$ to defect states accounts for the transition frequency but not the variation of the calculated DOS for $\omega<\omega_{peak}$. The calculated DOS for $\omega>\omega_{peak}$ matches the DOS calculated from TPC data.

Steady state photoconductivity measurements on a-As_2Se_3 are interpreted to indicate a set of defects sited at 0.66eV above E_v. TPC measurements exhibit no related emission feature. The DOS calculated from the Fourier transform method is a featureless exponential but is unreliable because of the limited measurement bandwidth. The magnitude of the TPC is too small for the DOS to consist solely of an exponential tail extending to the band edge. The DOS calculated from MPC measurements is also a featureless exponential but it is suggested that the MPC response is in the DOS independent régime.

Table of contents

Statement of objectives iv
Abstract v
Symbols and abbreviations list ix

1. Introduction to amorphous semiconductors 1
1.1 Rationale 1
1.2 Atomic structure 1
1.3 Electronic state structure 2
1.4 Thermodynamic equilibrium charge transport 5
1.5 Activation energy of extended state conductivity 6
1.6 Dangling bonds 6
1.7 Steady state photoconductivity 8
1.8 The "standard" model of the DOS of a-Si:H 12
1.8.1 Summary of the standard model 12
1.8.2 Band tails 13
1.8.3 Defect states 14
1.8.4 Conclusions 16

2. Transient photoconductivity 17
2.1 The experiment 17
2.2 Multiple trapping 18
2.3 The TROK model 19
2.3.1 Application to an exponential DOS 20
2.3.2 TROK procedure for obtaining the DOS from measured TPC 22
2.3.3 Limitations of TROK 22
2.3.4 Saturation and recombination 23
2.3.5 Emission rate treatment of recombination controlled TPC 24
2.4 Volterra equation method 26
2.5 The time of flight (TOF) experiment 27
2.5.1 Dispersion 28
2.6 Numerical computer simulation 29

3 The modulated photocurrent (MPC) experiment 30
3.1 Description of the experiment 30
3.2 Multiple trapping analysis 31
3.3 Calculation of the DOS from MPC spectra 33
3.4 Low frequency analysis 34
3.4.1 Extension of Oheda analysis 34

3.4.2 Other MPC analyses 36

4 Fourier transform method 37
4.1 Mathematical basis 37
4.2 Calculation of the Fourier transform 38
4.3 Evaluation of the numerical Fourier transform 39
4.4 Use of the Fourier transform method with simulation data 44
4.5 Conclusions concerning the use of the Fourier transform method 46

5 Experimental methods 48
5.1 Sample details and characterisation 48
5.1.1 Coplanar gap cells 51
5.1.2 Sample details 51
(Table) 49
5.2 Transient photocurrent measurements 51
5.2.1 TPC system overview 51
5.2.2 The sample chamber and cryostat 53
5.2.3 The pre-amplifier 53
5.2.4 Light sources 56
5.2.5 Signal capture and processing 58
5.3 Modulated photocurrent measurements 59
5.3.1 MPC system overview 59
5.3.2 Phase sensitive detection 60
5.3.3 Sample circuit 61
5.3.4 Other sources of error 64

6 Zero bias TPC in undoped a-Si:H 65
6.1 Linear régime 65
6.2 Discussion of the deep bump interpretation 68
6.3 Validity of Fourier transform 74
6.4 Thermalisation current magnitude 75
6.5 Intensity dependence 76
6.6 Summary 78

7 TPC with optical bias in undoped a-Si:H 80
7.1 The undershoot 80
7.2 Experimental characterisation of undershoot 80
7.3 Theoretical treatment of Pandya and Schiff 83
7.4 Discussion of results of theoretical treatment 86
7.5 Comparison of theory with experiment and simulation 88

7.5.1 Computer simulation 88
7.5.2 Experiment 91
7.5.3 Alternative approach to investigating the undershoot behaviour 93
7.6 Other features of TPC with optical bias 93
7.7 Summary 95

8 Modulated photocurrent in undoped a-Si:H 96
8.1 Experimental MPC results 96
8.2 MPC spectra computed from rate equations using an assumed DOS 100
8.3 Comparison of MPC with Fourier transform TPC spectra 103
8.4 Summary 107

9 Measurements on amorphous arsenic selenide 109
9.1 Transient photocurrent measurements 109
9.2 Modulated photocurrent measurements 111
9.3 Summary 113

10 Summary and conclusions 114

Appendices
A Numerical modelling of multiple trapping processes (including modelling parameters used in this work) 118
B Treatment for MPC including hole transitions explicitly 121
C Derivation of the time at which $\delta n=\delta n^*$ 123

References 124
Publications and conference presentations arising from this work 127

Symbols and abbreviations list

μ	mobility
υ	attempt-to-escape frequency
σ	conductivity
σ_d	dark conductivity
$\sigma_{ss}=\sigma-\sigma_d$	photoconductivity
τ_n	free electron free recombination time
$\omega_n=n_{ss}C_n$, $\omega_p=p_{ss}C_p$	

C_n,C_p,C_R	electron trapping, hole trapping, recombination coefficients
E_c,E_v	conduction, valence band mobility edge
E_f	thermodynamic equilibrium Fermi level
E_{fn},E_{tn},E_{tp}	electron quasi-Fermi level, electron, hole *trap* quasi Fermi level
$\delta f_d,f$	transient deep state, steady state total occupation function
$g(E)$	density of states distribution function
g_c	conduction mobility edge density of states
$\delta G,G_{ss}$	pulse photogeneration density, steady state photogeneration rate
G_ω	modulated generation rate sinusoidal amplitude
$\delta I,I_{ss},I$	transient photocurrent , steady state photocurrent, total current
I_ω	modulated photocurrent sinusoidal amplitude
kT_c	conduction band-tail exponential distribution characteristic energy
$\delta n(t),n_{ss},n_d,(\delta p(t),p_{ss},p_d)$	transient free, steady state excess, thermodynamic equilibrium free electron (hole) density
$n_t(E)$	trapped electron density distribution function
$n_w,(p_w)$	modulated photocurrent electron (hole) sinusoidal density amplitude
$\overline{n}(E),\overline{p}(E)$	emission factor for trapped electrons, holes

DOS	density of states
MPC	modulated photoconductivity
TPC	transient photoconductivity

Chapter 1 Introduction to amorphous semiconductors

1.1 Rationale

The reality of scientific research is that the majority of effort and resources goes into those areas which look most likely to offer a return on investment. One of the most lucratively rewarding of these investments has been the study of the behaviour of electrons in materials, in particular semiconducting crystalline materials. The application of quantum mechanics invoking the symmetries of the crystalline structure has resulted in a very full and technologically useful understanding. The understanding of the behaviour of semiconductors in the amorphous state, where symmetry arguments cannot be used, has by comparison lagged behind. The technological possibilities opened up by the discovery that hydrogenated amorphous silicon (a-Si:H) can be doped have resulted in an explosion of effort in the amorphous field. Many of the resultant applications, for example photovoltaics, image sensors and electrophotography, make use of the photoconductive properties of amorphous semiconductors. In addition photoconductive measurements are a powerful probe of the electronic state structure. Thus from the point of view of applications and of fundamentals an understanding of the photoconductive behaviour of materials in the amorphous state is essential to further progress in the field.

1.2 Atomic structure

The characteristic feature of a solid in the amorphous state is the disorder of the atomic structure. This disorder is long range in nature. A crystalline structure is ordered in the sense that knowledge of the unit cell of the lattice allows the prediction of the positions of all atoms in the material over many bond lengths. On the atomic scale crystalline and amorphous structures are similar because the same chemical bonding constraints are operating, the atoms in the amorphous material being slightly displaced from their positions in the crystal. On a scale of many bond lengths the cumulative effect of the displacements is that the positions of atoms in an amorphous structure are unpredictable. This is termed a "Continuous Random Network" (CRN) and is depicted in figure 1.1. Also illustrated in the figure is a qualitatively different feature of the amorphous state, the *isolated* coordination defect or dangling bond which occurs when the network is unable to satisfy all the bonds which can potentially be formed by an atom.

Crystal lattices constitute the minimum energy configurations for atoms in a solid. The formation of the higher energy CRN is made possible by removing thermal energy swiftly enough from the system when the solid is formed from its liquid or gaseous precursor that the atoms do not have time to adopt a crystal configuration. The

thermal disorder of the precursor is thus frozen in. For glasses formation can occur through fast cooling from the melt, the solid forming at the glass transition temperature T_g. For amorphous silicon crystallisation occurs too swiftly and other methods must be used.

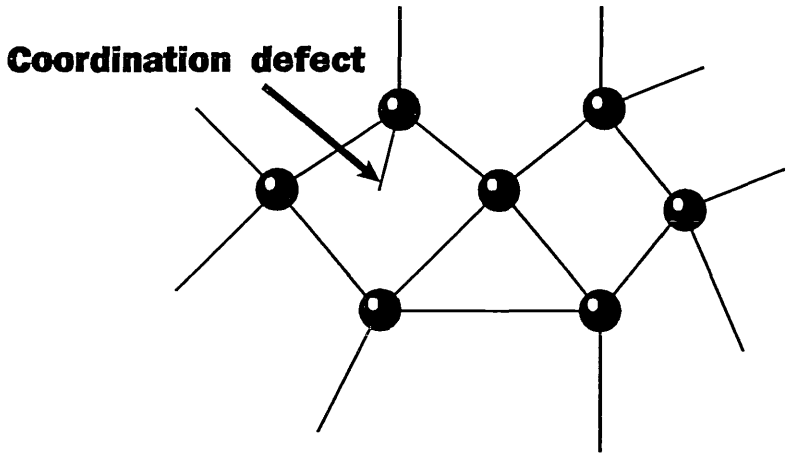

Figure 1.1 Continuous random network (CRN) model of the atomic structure of an amorphous material. Also illustrated is an isolated coordination defect or dangling bond.

A consequence of the random nature of the CRN is that it is difficult to define the optimum configuration. In fact the macroscopic properties of amorphous materials can be highly preparation dependent, a feature which has complicated comparisons between studies made in different laboratories. The frozen in CRN also shows more plasticity than crystalline structures, bonding configurations can change and the macroscopic properties can vary with the sample history.

1.3 Electronic state structure

Although the band structure of crystalline electronic theory appears as a consequence of the periodicity of the lattice it is found that the concept is applicable to the aperiodic amorphous state. An equivalent description of the band structure considers the local chemical bonding interactions. Since the local environments of an atom in a crystalline and amorphous structure are similar, and the electronic band structure is most strongly influenced by the local interactions, the crystal and amorphous band structures are also similar.

Thus in an amorphous as in a crystalline semiconductor there is a valence band and a conduction band consisting of a quasi-continuum of allowed energies for electron wavefunctions, these wavefunctions extending throughout the material so that they are said to be delocalised or extended. Where the amorphous case differs is in the amount of scattering experienced by the electrons. The electronic wavefunctions of a crystal experience scattering because of perturbations to the periodic lattice potential caused by

imperfections or thermal deformations. In the amorphous case the disorder in the potential is so strong as to cause the breakdown of the momentum selection rules for electronic state transitions. This can be seen as follows from the Heisenberg uncertainty principle if it is assumed the scattering length Δx is approximately equal to the interatomic spacing a_0;

$$\Delta k = \hbar/\Delta x \approx \hbar/a_0 \approx k \qquad (1.1)$$

where k is the electronic momentum which is of the magnitude of $1/a_0$ and Δk the uncertainty in the momentum. Since Δk is of the same order as k the momentum is not a good quantum number. Thus there are no electronic transitions in an amorphous semiconductor which are precluded by the necessity for momentum conservation. Alternatively the loss of k selection rules may be seen as a consequence of the lack of long range structure of the CRN against which to define preferred directions.

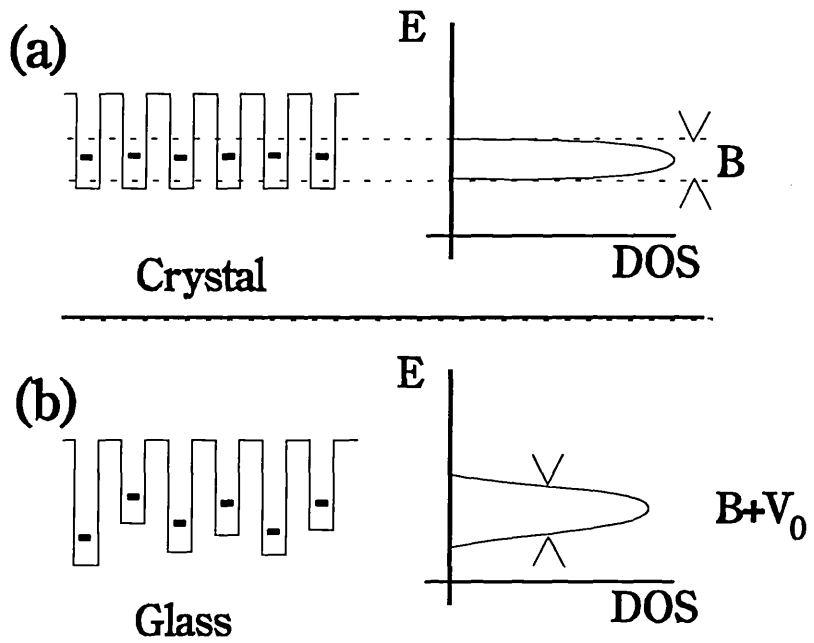

Figure 1.2 The Anderson model of the potential wells for (a) a crystalline lattice and (b) an amorphous network. V_0 is the disorder potential.

A further consequence of the disorder in the potential is the existence of *localised* wavefunctions, electron states intrinsic to the material which are confined to a small volume rather than extending throughout the material. A transition in the nature of electronic states between delocalised and localised as an order parameter is varied can be seen in a simplified theoretical model due to Anderson; for details see Mott and Davis (1979). The model begins with the tight binding approximation which represents the atoms in a crystal by a regular array of identical potential wells, figure 1.2(a). For a wavefunction of the single atom which only weakly overlaps in the array the interaction

between states broadens the state energy to form a narrow band of delocalised electron states of energy width B. The disorder of an amorphous solid is partially represented by varying the well depth by a random potential of average magnitude V_0, figure 1.2(b), which broadens the band. Anderson showed that above a critical value for the ratio V_0/B (the Anderson criterion) all the wavefunctions are localised.

For a band in which the Anderson criterion is not satisfied there are still localised states at the band edges where the density of states (DOS) is smallest and hence the separation between the volumes associated with the states the greatest, giving the smallest values for the atomic wavefunction overlap integral. For a real amorphous material the energy bands are too broad compared to the disorder potential for complete localisation but the band edges are broadened by the disorder and states there are localised. These are referred to as *tail states* or *band tails*.

The picture of the electronic state structure for an amorphous semiconductor thus built up is illustrated in figure 1.3. The figure is a schematic graph of the electron density of states (DOS) distribution with energy, symbolically represented as a function of energy as g(E) with units $cm^{-3}eV^{-1}$. The density of states will be referred to frequently in this work. The conductivity through states of energy E,$<\sigma_0>$, is finite for extended states but zero for localised states at T=0. Hence the energy E_c (E_v for the valence band) separating the band-tail localised states and non-localised or extended states is called the *mobility edge* and the region between E_c and E_v the *mobility gap*. These concepts replace the band edge and band gap of crystalline theory. As is discussed below charge transport behaviour is determined by whether the states forming the conduction path are above or below the mobility edge.

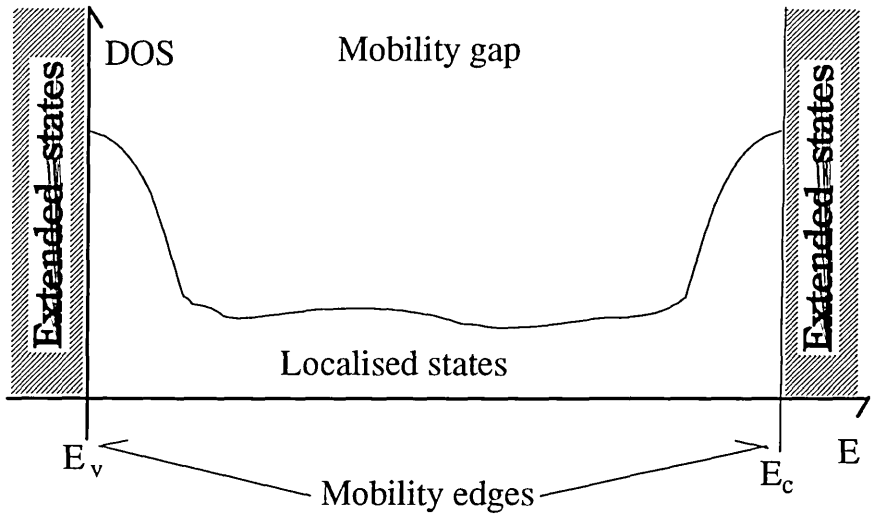

Figure 1.3 General model of the density of states (DOS) distribution of an amorphous semiconductor. There is a continuous distribution of localised states in the mobility gap, composed of tails of the disorder broadened crystalline energy bands at the gap edges and defect states deep in the gap.

1.4 Thermodynamic equilibrium charge transport

Transport via extended states is pictured as tunnelling in a region of high state density between states of closely similar energy, which can therefore occur without thermal assistance. Transport via tunnelling or *hopping* between nearest neighbour localised states can occur with the aid of electron-phonon interactions to overcome energy differences. Since phonons are always present the distinction between delocalised and localised states becomes blurred, leading to the concept of phonon induced delocalisation affecting states at the edges of the mobility gap (Mueller and Thomas, 1983).

Fermi-Dirac occupation statistics for thermodynamic equilibrium hold for non-degenerate electron states of an amorphous material. Consider conduction occurring through a conduction path consisting of a strip of energy width kT of states at E_x. The density of electron occupied states is $kTg(E_x)f_0(E_x)$, where f_0 is the occupation function, so the conductivity of the strip is

$$\sigma_x = ekT\mu_x g(E_x)\exp\left[-(E_x - E_f)/kT\right], \qquad (E_x\text{-}E_f)>>kT \qquad (1.2)$$

where μ_x is the conduction path mobility and E_f the Fermi potential. A similar equation applies to holes. It is assumed for a particular set of experimental conditions conduction is dominated by a particular conduction path for which the mobility-charge density product is greatest. Thus at higher temperatures the dominant conduction path is at the mobility edge, the path moving into localised states at lower temperatures. The transport analysis used in this work assumes conduction through extended states.

Transport in low mobility solids for both extended and localised states is most simply treated using a classical diffusion model. The resulting expression for the mobility is

$$\mu=(er^2/6kT)P \qquad (1.3)$$

where P is the probability of electron transfer between sites separated by a spacing r. For extended states P is a constant, the electronic frequency $\nu_{el}\approx10^{14}\text{-}10^{15}s^{-1}$, and r is the atomic spacing, giving an electron mobility of μ_c=10-50 $cm^{-2}(Vs)^{-1}$. The probability for hopping between nearest neighbour localised states is

$$P=\exp(-2\alpha r)\nu_{ph}\exp(-W/kT) \qquad (1.4)$$

The $\exp(-2\alpha r)$ term, r now being the average centres distance between nearest neighbour states, is related to the localised state wavefunction overlap. The $\nu_{ph}\exp(-W/kT)$ term is the probability of electrons gaining the average energy required to hop W, ν_{ph} being the phonon frequency which is of magnitude 10^{11}-$10^{13}s^{-1}$. At low enough temperatures with the conduction path at the Fermi level it is suggested that electrons hop to distant states with energies within kT of E_f, rather than to nearest neighbour sites, because of the much reduced density of states.

1.5 Activation energy of extended state conductivity

In general in this work it is assumed that charge conduction can be treated as unipolar, and that the carrier is the electron unless otherwise stated. Thus for extended state dominated conduction the conductivity from equation 1.2 can be written as

$$\sigma = \sigma_0 \exp\left[-(E_c - E_f)/kT\right] \qquad (1.5)$$

The classical diffusion expression for mobility, equation 1.3, implies the conductivity prefactor σ_0 is temperature independent. Although other expressions for μ can be assumed in general the power dependence on temperature is between 0.5 and 1 so that at most σ_0 is only weakly temperature dependent. However E_c-E_f is temperature dependent because of phonon interaction related shifts in E_c and E_v. There are also statistical shifts in E_f when the Fermi level lies in a region of rapidly varying g(E) because of the constraint of charge neutrality. Experimentally plots of σ vs. 1/T yield a straight line thus it is assumed that the effects of the reference energy shifts may be described as E_c-E_f=$(E_c$-$E_f)_0$-γT. Substituting into equation 1.5 gives

$$\sigma = \sigma_0 \exp(\gamma/k)\exp\left[-(E_c - E_f)_0/kT\right] \qquad (1.6)$$

The activation energy of the conductivity is therefore $(E_c$-$E_f)_0$ rather than E_c-E_f. σ_0 has been determined in undoped a-Si:H from conductivity measurements on high defect density material in which the statistical shift is negligible (Stuke, 1987). The remaining shift due to the temperature dependences of E_c and E_v is estimated from optical absorption measurements to have a coefficient $\gamma \approx 2.4\times10^{-4}eVk^{-1}$, giving $\sigma_0 \approx 150 - 200(\Omega cm)^{-1}$. In this work a value of σ_0=200$(\Omega cm)^{-1}$ is used to estimate E_c-E_f in undoped a-Si:H.

1.6 Dangling bonds

A further contribution to the density of states in mid-gap comes from the coordination defects or dangling bonds mentioned in §1.2 and illustrated in figure 1.1.

Dangling bonds are amphoteric, i.e.; are able to act as donors or acceptors, because they consist of an unpaired electron in the neutral state. When unoccupied a dangling bond has no charge and is designated by the symbol D^0, when occupied by a hole it is positively charged and designated by D^+ and when occupied by an electron it is negatively charged and designated by D^-. For amorphous silicon it is expected that the energy of the D^- state is further from E_v than D^0 and D^+, i.e.; that the energy required to remove an electron from a D^- state is smaller, because of the electrostatic repulsion between the two electrons on the site. The difference between the D^0/D^+ and the D^- energies is called the *correlation energy*, U, defined to be positive for the case above. In a-As_2Se_3 and other chalcogenide glasses it is suggested that U is *negative*, i.e.; D^- is closer to E_v, because of fast local changes in the lattice configuration when a D^- is created.

The proportions of the different charge states in thermodynamic equilibrium cannot be described by the same statistics pertaining to the single electron tail states. Taking account of the spin degeneracy and of the conservation equation

$$F^0+F^++F^-=1 \tag{1.7}$$

where $F^{0/+/-}$ is the fraction of dangling bonds in the $D^{0/+/-}$ state, the following can be obtained from considerations of thermodynamics (Adler and Yoffa, 1976), or of detailed balance (Main 1988)

$$\begin{aligned} F^0 &= \left\{1+\tfrac{1}{2}\exp\left[(E_0-E_f)/kT\right]+\tfrac{1}{2}\exp\left[-(E_0+U-E_f)/kT\right]\right\}^{-1} \\ F^+ &= \tfrac{1}{2}F^0\exp\left[(E_0-E_f)/kT\right] \\ F^- &= \tfrac{1}{2}F^0\exp\left[-(E_0+U-E_f)/kT\right] \end{aligned} \tag{1.8}$$

where E_0 is the energy of the D^0 state.

The "standard" defect model for a-Si:H places the dangling bonds in a single, disorder-broadened band in mid-gap. In the undoped material the defects dominate the charge neutrality condition so that $E_f=E_0+U/2$. Consequently from equations 1.8 with positive U the majority of the dangling bonds are in the D^0 state, although the broader is the distribution the greater is the charged state density (Okamoto and Hamakawa 1977). The more recent "defect pool" model (Winer, 1990, Schumm and Bauer, 1991, Powell and Dean 1993) postulates a creation mechanism for defects of the breaking of weak silicon-silicon bonds. From thermodynamic considerations a separate frozen-in distribution is calculated for each of the defect charge states, with D^0 and D^- below the Fermi-level and D^+ above. In undoped a-Si:H realistic model parameters yield larger charged than neutral defect densities.

1.7 Steady State Photoconductivity

Illuminating a semiconductor with a constant intensity of light of an appropriate wavelength changes the conductivity by altering the carrier densities. The *photoconductivity* σ_{ss} is defined as the difference between the observed conductivity under illumination σ and in thermodynamic equilibrium in the dark σ_d.

$$\sigma_{ss}=\sigma-\sigma_d \tag{1.9}$$

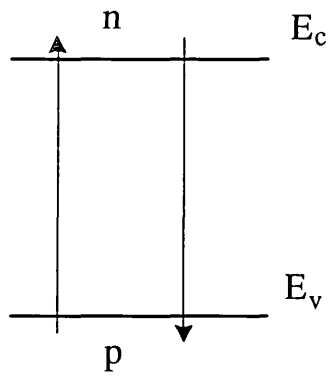

Figure 1.4 Electron transitions in a trap free semiconductor.

As an introduction to some of the basic concepts of photoconduction consider the situation of figure 1.5 of a trap free semiconductor illuminated by a constant intensity of light of photon energy greater then the band gap. In the following it is assumed electrons are the dominant carrier. The illumination excites the creation of excess densities of free electrons and holes n_{ss}, p_{ss} at a rate G_{ss} above the thermal generation rate G_d and the free carriers recombine by a reverse transition. The electron lifetime τ_n is defined as the mean time spent by *excess* electrons in extended states before recombining. In steady state the recombination and generation rates are equal so

$$G_{ss=}n_{ss}/\tau_n \tag{1.10}$$

Thus a measurement of the steady state photoconductivity $\sigma_{ss}=n_{ss}e\mu_c$ yields the product $G_{ss}\mu_c\tau_n$.

If τ_n is independent of the generation rate then the photoconductivity is simply proportional to the generation rate. The recombination time dependence on G_{ss} is determined by the nature of the recombination process and generally exhibits regimes of differing behaviour characterised by the temperature and generation rate magnitude, as is demonstrated below for the situation of figure 1.4. The recombination rate is

$$R=(n_d+n_{ss})(p_d+p_{ss})C_R=G_d+G_{ss} \tag{1.11}$$

C_R being the probability per second of an electron recombining with a given hole (the hole capture coefficient) and n_d, p_d the thermodynamic equilibrium free carrier densities. The material is electrically neutral and trap free so n=p and $n_d=p_d$, thus $n_{ss}=p_{ss}$. The thermal generation rate $G=n_d p_d C_R$. Substituting into equation 1.11 we obtain

$$G_{ss} = \left(2n_d n_{ss} + {n_{ss}}^2\right) C_R \qquad (1.12)$$

For $G_{ss} \ll G_d$ we have $n_{ss} \ll n_d$, so n_{ss} is proportional to G_{ss}, i.e.:, the probability to recombine of a single electron is determined by a fixed density of thermally generated holes. This condition, in which the recombination rate depends on the excess density of only one of the recombining species is called *monomolecular* recombination. For $G_{ss} \gg G_d$ we have $n_{ss} \gg n_d$, giving $n_{ss}=(G_{ss}/C_R)^{1/2}$ - the excess electron density varies as the square root of the excess generation. This is a consequence of the recombination rate depending on the densities of *both* the recombining species, and is termed *bimolecular* recombination.

Recombination in amorphous semiconductors is more likely to be mediated by states in the gap. The Shockley-Read mechanism (Shockley and Read, 1952), figure 1.5, entails two separate transitions from the mobility edges. For low generation such that the total density of recombination centres N_t is much more than the steady state density of electron occupied centres n_t recombination is monomolecular because $\tau_n=C_n N_t$ is independent of G_{ss}. Note that for Shockley-Read recombination in general $\tau_n \neq \tau_p$.

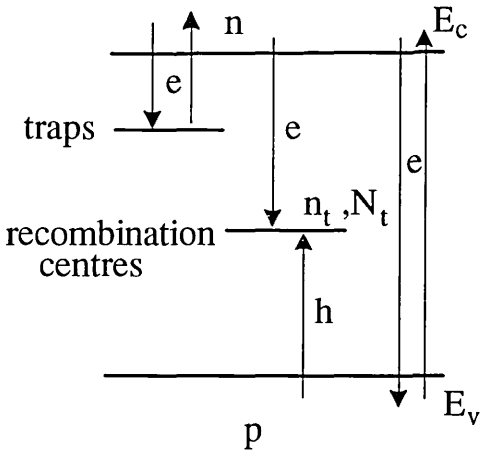

Figure 1.5 Shockley-Read recombination involving electron (e) and hole (h) transitions to level of localised states. Also shown are trapping and release electron transitions between a level of localised states at shallow energy and the conduction band.

A distinction can be drawn between states in the gap mediating recombination and the states also shown in figure 1.5 close to the band edges which act as temporary

traps of charge. Carriers captured by these states are more likely to be thermally re-emitted than to capture a free carrier of opposite sign. The presence of traps affects time resolved conductivity measurements, for example transient photoconductivity which is described in chapter 2.

The probability of thermal re-emission of a trapped carrier can be obtained by consideration of *detailed balance*, the principle that in thermodynamic equilibrium the forward and reverse rates of all processes are equal. Thus with reference to figure 1.5 for electrons

rate of capture = rate of re-emission (thermodynamic equilibrium)

$$C_n n_d N_t (1 - f_0(E_t)) = e_n N_t f_0(E_t) \qquad (1.13)$$

where e_n is the emission probability s^{-1}. Substituting for the distribution function gives

$$e_n = \nu_n \exp\left[-(E_c - E_t)/kT\right] \qquad (1.14)$$

This has the form of an attempt to escape frequency $\nu_n = C_n N_c$ multiplied by the probability of finding the energy from the thermal background to make the transition to E_c. A similar expression holds for the hole emission probability e_p. Note that 1.14 has been derived for one electron states.

The full Shockley-Read analysis obtains the occupation f under illumination of a single electron state anywhere in the gap by considering all four possible free-localised transitions for a particular set of states, figure 1.6. In steady state the sum of rates (a) and (d) must equal the sum of (b) and (c). Manipulation yields

$$f(E_t) = \frac{nC_n + pC_p}{(n + \overline{n}(E_t))C_n + (p + \overline{p}(E_t))C_p} \qquad (1.15)$$

where $\overline{n}C_n = e_n$, $\overline{p}C_p = e_p$. Note that this expression is *independent* of N_t. Simmons and Taylor showed that it is also applicable to arbitrary *distributions* of states (Simmons and Taylor, 1972).

In treatments of localised state controlled phenomena the simplifying assumption is frequently made that the capture coefficients C_n and C_p are independent of energy depth, the justification being merely the absence of specific evidence to the contrary. The assumption is used in the following and in other relevant treatments in this work. For a distribution of a particular species of localised states, defined by the ratio C_n/C_p, f(E) exhibits different regimes of behaviour for traps and recombination centres, see figure 1.7. For traps the electron release rate is much greater than the capture rate of holes so that from equation 1.15

$$f(E) \approx n/\bar{n} \tag{1.16}$$

i.e.; the occupation of traps at depth E is related to that of free states at E_c by a Boltzmann ratio. For recombination centres the capture rates are much larger than the release rates so that

$$f(E) \approx \frac{nC_n}{nC_n + pC_p} \tag{1.17}$$

i.e.; the occupation is constant.

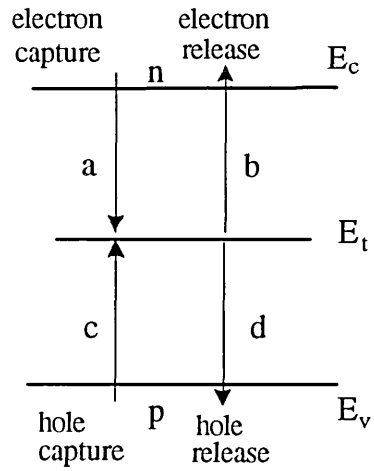

Figure 1.6 Electron and hole transitions controlling the occupation of a localised state.

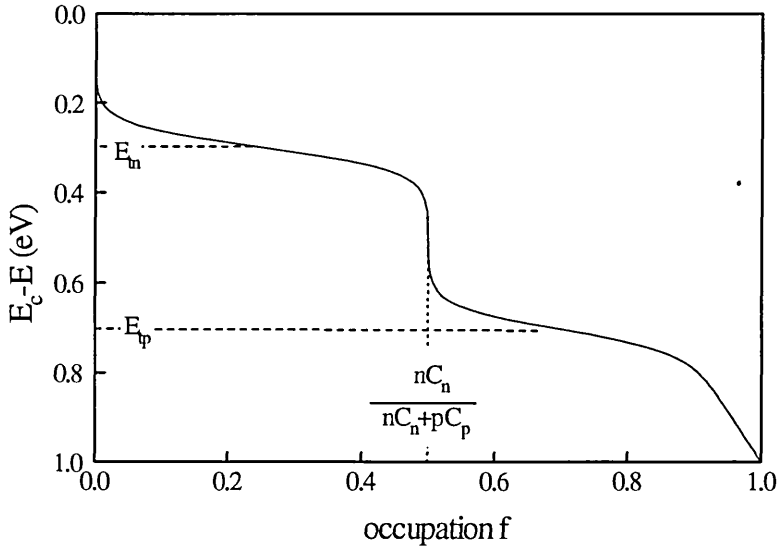

Figure 1.7 Simmons-Taylor occupation function for localised states in an amorphous semiconductor under illumination. The electron and hole *trap* Quasi-Fermi levels E_{tn} and E_{tp} mark the transition between the regions of quasi-thermal equilibrium occupation at the gap edges and constant occupation around mid-gap.

It is useful to define an energy E_{fn}, the electron quasi-Fermi level, which is related to the increased electron density under illumination by

$$n = N_c \exp\left[-(E_c - E_{fn})/kT\right] \qquad (1.18)$$

From 1.16 the occupation of *shallow* traps can be described using the same quasi-Fermi level

$$n_t(E) = g(E)f(E) = g(E)\exp\left[-(E_c - E_{fn})/kT\right] \qquad (1.19)$$

The occupation of traps is more completely described using a modulated Fermi function and an electron *trap* quasi-Fermi level, E_{tn} , defined as the energy at which the occupation is half the occupation of equation 1.17, so that E_{tn} marks the transition between states acting as traps and as recombination centres. In general E_{tn} is only slightly above E_{fn} in n-type conductors. Similarly free and trap quasi-Fermi levels E_{fp} and E_{tp} may be defined for holes. Thus when a semiconductor is illuminated the dark Fermi level is said to split, and with increasing generation rate the trap quasi-Fermi levels move away from each other towards the mobility edges so that an increasing proportion of the gap states become recombination centres.

The increase in the density of recombination centres with increase in generation rate can be used to explain the phenomenon frequently observed of a photoconductivity excitation dependence intermediate between mono- and bimolecular, $n_{ss} \propto G_{ss}^{\gamma}$, $0.5<\gamma<1.0$, in a simple model first proposed by Rose (Rose, 1963). For a form of the DOS described by

$$g(E) = g_c \exp\left[-(E_c - E)/kT_c\right] \qquad (1.20)$$

where T_c has units of Kelvin the analysis yields $\gamma=T/(T_c+T)$. The form for g(E) of equation 1.20 is frequently invoked in discussing localised states in amorphous materials, and is referred to as an "exponential tail of slope kT_c".

1.8 The "standard" model of the DOS of a-Si:H

1.8.1 Summary of the standard model

The "standard" model of the DOS of a-Si:H in the mobility gap region has a linear form for the energy distribution of the disorder broadened conduction and valence band tail states in the region of the mobility edges. This changes to an exponential form

deeper in the mobility gap. The centre of the mobility gap is occupied by defect states of with a total density, in good quality undoped material, of about $10^{16}cm^{-3}$. These are paramagnetic divalent states with a positive correlation energy and are identified as unsatisfied Silicon atom dangling bonds (see §1.6). The density of states at the mobility edges is $4\times10^{21}cm^{-3}eV^{-1}$. The experimental evidence which has contributed to the standard model is reviewed below. Much of the information in this section has been taken from Street (1991).

1.8.2 Band tails

1.8.2.1 Optical absorption

Optical measurements provide the simplest probe of the electronic state structure. It is not possible to use transmission data for band-to-band transitions alone to obtain a form for the DOS because the spectrum is a convolution of the conduction and valence band state distributions multiplied by the energy dependent transition matrix element $M(\hbar\omega)$. However transmission data does confirm some general aspects of the picture of the amorphous state. The overall shapes of the imaginary part of the transmission spectrum $\varepsilon_2(\omega)$ for crystalline Si and a-Si:H are similar because of the similar short range atomic environment in the two materials, but no sharp structure is observed in the a-Si:H spectrum because of amorphous broadening and the lack of **k** conservation. For the amorphous form there is no sharply defined energy gap. The absorption coefficient α is observed to decay continuously into the gap with an exponential energy dependence in the region of the optical gap E_g. Although this feature is observed in crystalline alkali halides it is now regarded as reflecting the shape of the disorder-broadened band-edge state distributions. The α spectrum is fitted well by the absorption spectrum calculated assuming a joint DOS calculated from time of flight (TOF) data (see below) and a constant value for the transition matrix element (Jackson et al 1985).

1.8.2.2 Electron photoemission/inverse photoemission

Electron photoemission/inverse photoemission does provide a direct measure of the DOS (Ley, 1984). Electron photoemission ejects free electrons from occupied states in the material through absorption of high energy photons. The kinetic energy distribution of the ejected electrons is directly related to the DOS, although corrections must be made for varying cross sections for emission.. A further problem is that the technique only probes to a depth of about 5nm. Inverse photoemission determines the unoccupied state distribution from the intensity spectrum of photons emitted when free electrons are trapped. The DOS in the region of the optical band edge for both the conduction and valence band is found to be linear over a range of 0.5eV down to a density of $3\times10^{21}eV^{-1}cm^{-3}$. The band tails are seen to extend continuously into the gap

but the exact shape cannot be resolved because the emission spectra are dominated by the large mid-band state densities.

The related technique of total electron yield photoemission spectroscopy (Winer and Ley, 1989) does have the required sensitivity but only probes occupied states. Electrons are ejected by photons of energy just sufficient to overcome the work function. The DOS is given by the derivative with respect to photon energy of the electron yield. The valence band tail is observed to be linear near and above the mobility edge E_V, and to be exponential (see equation 1.20) deeper in the gap over a two order fall in density with a slope of about 50meV. Deeper still the distribution of defect states is detected.

1.8.2.3 Time of Flight (TOF)

The TOF experiment is described in §2.5. The analysis of TOF data depends on the TROK model of anomalously dispersive transient photoconduction described in §2.3. Although this work points out the failings of the model the results of TROK should be valid in the time range in which TOF is performed. TOF results over a wide range in temperature are consistent with exponential tails for the conduction and valence bands over a range of about 0.2eV (Marshall et al, 1986). The slope of the valence band tail matches that found from the total electron yield experiment. TOF is the main evidence for the shape of the conduction band tail, giving a slope of 0.022-0.026 eV. TOF does not probe shallow enough energies to reveal the linear portions of the tails.

1.8.2.4 Summary

The picture of the band tails from the above experiments has a linear DOS distribution in the region of the mobility edges and an exponential variation deeper in the mobility gap. The exponential slope of the valence band tail kT_V is greater than that of the conduction band kT_C. Why the DOS distribution should have an exponential dependence on energy is unclear, but that $kT_V > kT_C$ is consistent with the greater expected effect of spatial distortions on the p-states which go to form the valence band than on the spherically symmetric s-states forming the conduction band.

1.8.3 Defect states

1.8.3.1 Electron-spin resonance (ESR)

The technique of electron spin resonance is able to detect unpaired electron spins in a material. A magnetic field is applied to remove the spin state degeneracy and the degree of absorption of microwave radiation by induced spin-flip transitions measured. In the neutral state the dangling bond defect described in §1.6 is paramagnetic and therefore should be detected by ESR. A paramagnetic defect with a g-value of 2.0055 is indeed detected in undoped amorphous silicon, which is identified with dangling bonds. ESR can detect as few as 10^{11} spins, which is just sensitive enough to resolve the

density of below $10^{16}cm^{-3}$ dangling bonds in thin films of good quality a-Si:H. ESR does not resolve the energy distribution of ESR active states but does give structural information which is used to support the identification of the g=2.0055 states as dangling bonds (Biegelsen, 1981). The dangling bond signal decreases in doped a-Si:H because charged dangling bond states do not consist of unpaired electrons and are therefore not paramagnetic.

1.8.3.2 Defect state spectroscopy from thermal emission energies.

Three techniques come in to this category all of which rely on space charge effects. These are deep level transient spectroscopy (DLTS), field effect and space charge limited currents (SCLC). The DLTS experiment consists of the measurement of the transient capacitance of a Schottky contact during recovery from forward bias. The capacitance gives information on the DOS through the recovery of the depletion layer as trapped carriers are released from progressively deeper states. DLTS is difficult in undoped a-Si:H. In n-type material a deep minimum in the DOS between defects and tailstates at around 0.5eV is revealed.

The field effect technique involves inducing space charge in the channel of a field effect transistor structure through application of a gate voltage. Most of the induced charge is trapped and this produces a shift in the (quasi)Fermi-level Thus the degree of movement of the quasi-Fermi level depends on the density of the traps through which it is moving and this may be monitored by measurement of the channel conductivity. There are several problems associated with field effect. One is the difficulty of accurate analysis. Another is that only states close to the interface are probed. DOS distributions increasing monotonically from the midgap to the conduction band edge densities are produced, in contrast to DLTS. Additionally the DOS magnitude is larger than from DLTS.

In SCLC measurements a single carrier species is injected, for example by using a n^+-i-n^+ structure. The IV characteristic of the device is controlled by trapped space charge and again a DOS distribution can be obtained by consideration of the movement of the quasi-Fermi-level as progressively more charge is injected. The deduced DOS distribution in undoped material is similar to that from field effect and differs from that of DLTS.

Thermal emission techniques therefore give contradictory evidence for the shape and density of the deep defect distributions. A comparison of DOS distributions obtained by the techniques outlined above may be found in Mackenzie et al (1982).

1.8.3.3 Defect state spectroscopy from optical transition energies

Highly sensitive experimental procedures have been evolved to measure the very small optical absorption due to transitions from defect states, for example photothermal deflection spectroscopy (PDS) and the constant photocurrent method (CPM). PDS

measures the energy absorbed in the sample (and so detects all transitions) whereas CPM detects only those transitions resulting in the creation of a free carrier, ie; electrons in amorphous silicon. The absorption spectra obtained generally give information on the valence band tail and the portion of the deep state distribution below the Fermi level. A broad absorption band is seen below the exponential portion of the absorption spectrum extending from 1.5eV to 0.5eV below E_C. The integrated density of this broad band has been shown to be proportional to the ESR signal magnitude (Jackson and Amer, 1982), which is evidence to identify deep defect states with the ESR active states.

1.8.4 Conclusions

There is good evidence for the shape and magnitude of the valence band tail and reasonable evidence for the conduction band tail. In mid-gap there is a distribution of defect states the exact nature, density and distribution of which is more problematical. From mainly ESR evidence these states are identified with the single dangling bond defect of silicon.

2.1 The experiment

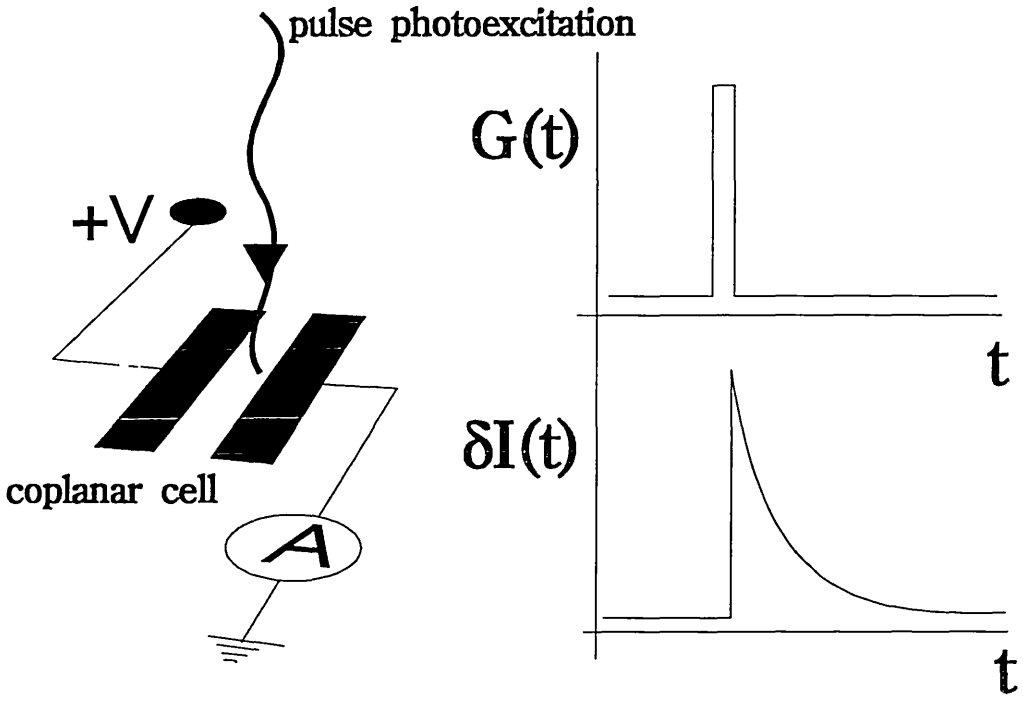

Figure 2.1 The transient photoconductivity (TPC) experiment

Figure 2.1 illustrates the transient photoconductivity (TPC) experiment. Coplanar electrodes are deposited on the top surface of the sample under examination. A potential difference is applied and a laser or led flash used to create a pulse generation of electron hole pairs in the gap between the electrodes. For a consideration of the factors determining the magnitude of the photogenerated density see §5.11. The resulting photocurrent is then measured as a function of time as it decays away. The detection equipment must be capable of resolving the photocurrent over many orders of time and magnitude. A background steady state illumination may be used and is sometimes referred to as optical bias.

The electrodes must be Ohmic at the field used in order that the number of carriers leaving the sample at any instant is balanced by an equal number entering. The transient photodecay then reflects solely the equilibration process of the excess carrier density mediated by the localised states. As a result of the equilibration process the photodecay has a form referred to as anomalously dispersive, or just dispersive, for reasons given in §2.5 on the related time of flight (TOF) experiment. In principle the decay contains information on the localised state densities and the associated trapping and recombination parameters. The TPC experiment therefore has great potential as a probe for the DOS in amorphous semiconductors if a suitable analysis can be devised.

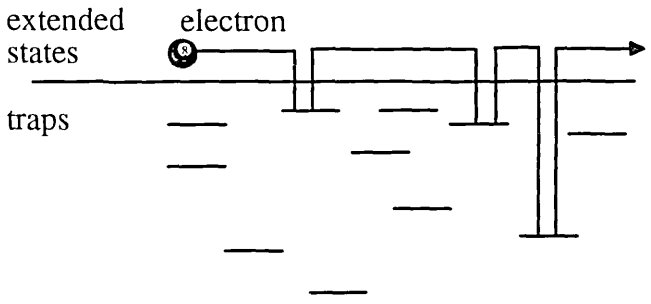

Figure 2.2 Multiple trapping conduction mechanism

Fundamental to an understanding of the equilibration process is the concept of *multiple trapping*. Figure 2.2 shows the progress of a typical carrier in extended states. It is captured and released many times by trapping states before it finally recombines. A distinction can thus be drawn between the time elapsed between generation and recombination, which is the time at which a feature linked to recombination is observed in a transient experiment, and the summed time the carrier spends in the extended states, the *free* time τ_f. It is when the elapsed free time exceeds characteristic trapping or recombination times that carriers (on average) are trapped or recombine.

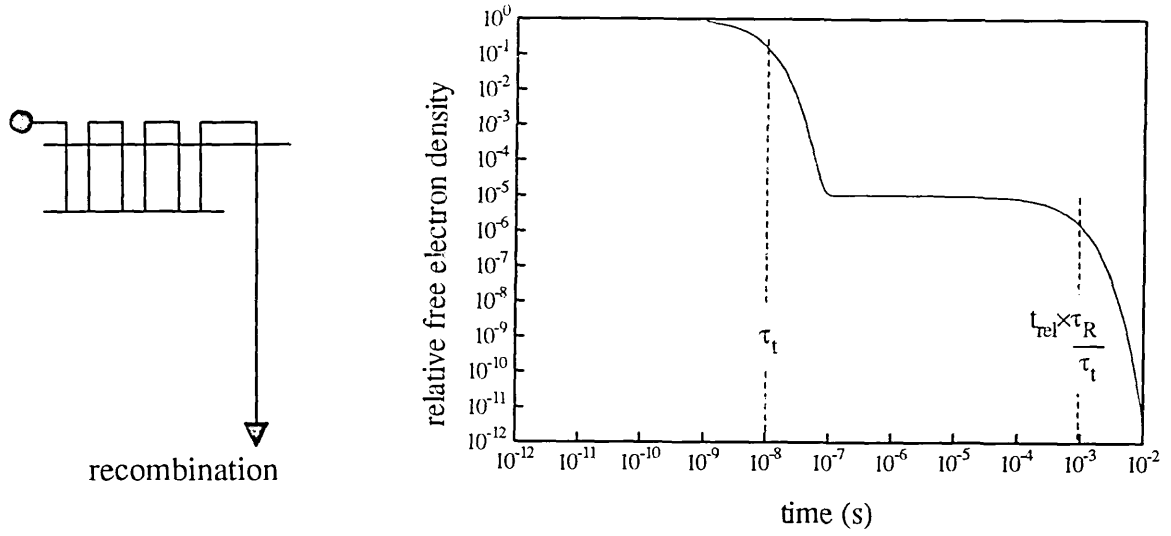

Figure 2.3 Computer simulated decay for a system having a recombination time τ_R and consisting of a single level of traps having a trapping time τ_t and release time t_{rel}.

The observed times of features in a transient decay are related to *both* the capture and release times from traps. Apart from the simplest cases however, the observed features do not coincide with *either* the capture or release times. Figure 2.3 illustrates this point with a simple system having recombination time τ_R and one set of trapping states having trapping time τ_t and release time t_{rel}, with $\tau_t << t_{rel}$. At time zero there is a pulse generation of free electrons. The free electron density n initially falls at time τ_t as

electrons are captured by the traps, until the trapping and release rates for the trap set are equal. This occurs when the trapped and free occupations are in a Boltzmann ratio. There is then a plateau region, in which a quasi-equilibrium exists between traps and extended states. Multiple trapping and release events are taking place, with negligible recombination. The recombination rate becomes significant when the average summed time spent by electrons in extended states approaches τ_R. The *observed* recombination time is $t_{rel} \times (\tau_R/\tau_t)$, because electrons on average undergo the trap-release cycle (τ_R/τ_t) times before recombining.

2.3 The TROK model

Tiedje and Rose (1980) and Orenstein, Kastner and Vaninov (1982) in separate papers devised a physical interpretation of earlier statistical work (Schmidlin, 1977) on multiple trapping non equilibrium transport in the presence of a distribution of traps, which will be referred to here as the "TROK" model, with apologies to Vaninov. There are important limitations to the range of validity, which are discussed in §2.3.3 below, but the model is useful for the insight it gives. The model will be propounded here in terms of electron conduction but it can equally well be applied to holes.

The central concept is of the *thermalisation energy* E_c-E_{th} at which traps will have on average released once in time t after a photogeneration pulse. The average release time from a set of traps is the inverse of the release probability per second e_n. Thus from equation 1.14

$$E_{th} = kT \ln(\upsilon t) \qquad (2.1)$$

The same concept was proposed by Arkhipov and Rudenko (1978).

Shallow traps, those at energies more than kT *above* E_c-E_{th}, have release times much shorter than t, so that the trapping and release rates are equal (provided the rate of change of n is slow enough) and the occupation of the traps is in a Boltzmann ratio with the free states. This quasi-thermal equilibrium distribution is maintained as the free electron density varies. Deep traps, those at energies more than kT *below* E_c-E_{th}, on average have not released at all, so their occupation is constant with energy although increasing with time. It is argued therefore that the instantaneous transient excess occupation of traps looks like figure 2.4, a modulated Fermi distribution centred on E_c-E_{th}. As the decay progresses E_c-E_{th} moves further into the gap, releasing charge which is subsequently retrapped into the deep traps thus increasing their occupation.

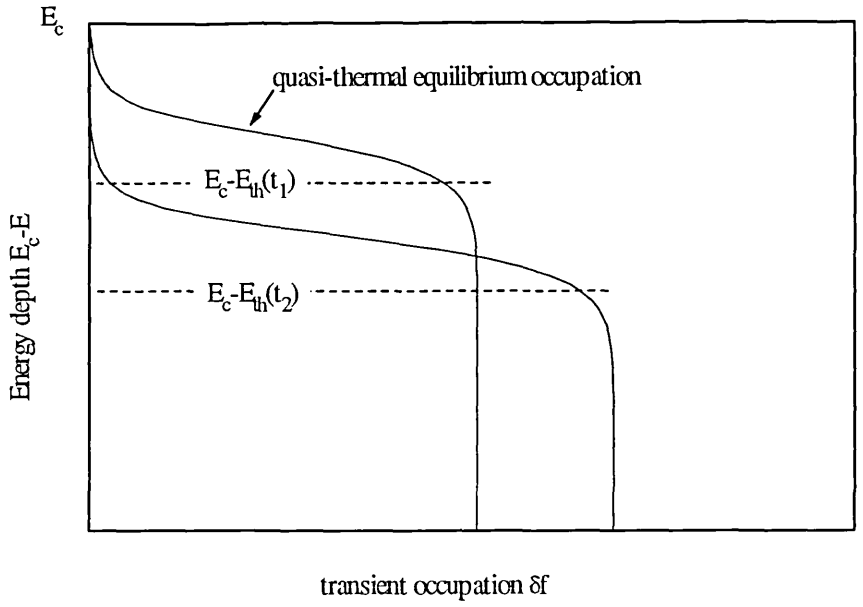

Figure 2.4 TROK transient occupation function $\delta f(E,t)$, at two successive instants $t_2>t_1$ during a photodecay.

2.3.1 Application to an exponential DOS

Figure 2.5 shows the density distribution of trapped charge in a broad (i.e.; $T_c>T$, see note at the end of this section) exponential DOS at successive instants during a computer simulated (see §2.6 and appendix A) TPC decay. The simulation is in agreement with the predictions of the TROK model for this shape of DOS. The peak of the distribution and hence the majority of the charge, spoken of as the charge packet, is in a strip of width kT at E_c-E_{th}. The charge packet is said to *thermalise* to deeper energies through the process of release of charge from states at E_c-E_{th} and recapture into the largest density of deep traps, i.e.; those forming the kT strip just below E_c-E_{th}.

An analytic form can be easily derived using the TROK model for the transient free carrier density dependence on time $\delta n(t)$ for a charge packet thermalising in an exponential tail. Once initial trapping of the transient density of carriers has occurred we can write by consideration of the transient occupation function;

$$\delta N_t \approx \delta f_d \left\{ \int_{E_c-E_{th}}^{E_c} g(E)\exp\left[-(E_c-E)/kT\right]dE + \int_{E_v}^{E_c-E_{th}} g(E)dE \right\} \qquad (2.2)$$

where δN_t is the total transient trapped carrier density, δf_d is the transient occupation of the deep states, and g(E) is given by equation (1.20). δN_t is approximately equal to the initial pulse generated free charge density. The transient occupancy of free states is related to that at E_c-E_{th} by

$$\delta n/N_c = \delta f_d \exp(-E_{th}/kT) \qquad (2.3)$$

Combining equations 2.2 and 2.3 to eliminate δf_d and substituting for g(E) and E_{th} gives

$$\delta n = \delta N_t \alpha (1-\alpha)(\upsilon t)^{-(1-\alpha)} \qquad (2.4)$$

where α=T/Tc. Thus the model predicts a power law decay of index -(1-α). Power law decays are indeed frequently observed in amorphous materials. Note that the analysis only applies to the case $T<T_c$. If $T>T_c$ the product of the shallow trap Boltzmann distribution and the DOS implies that the density of trapped charge *decreases* in going from the mobility edge to E_c-E_{th}.

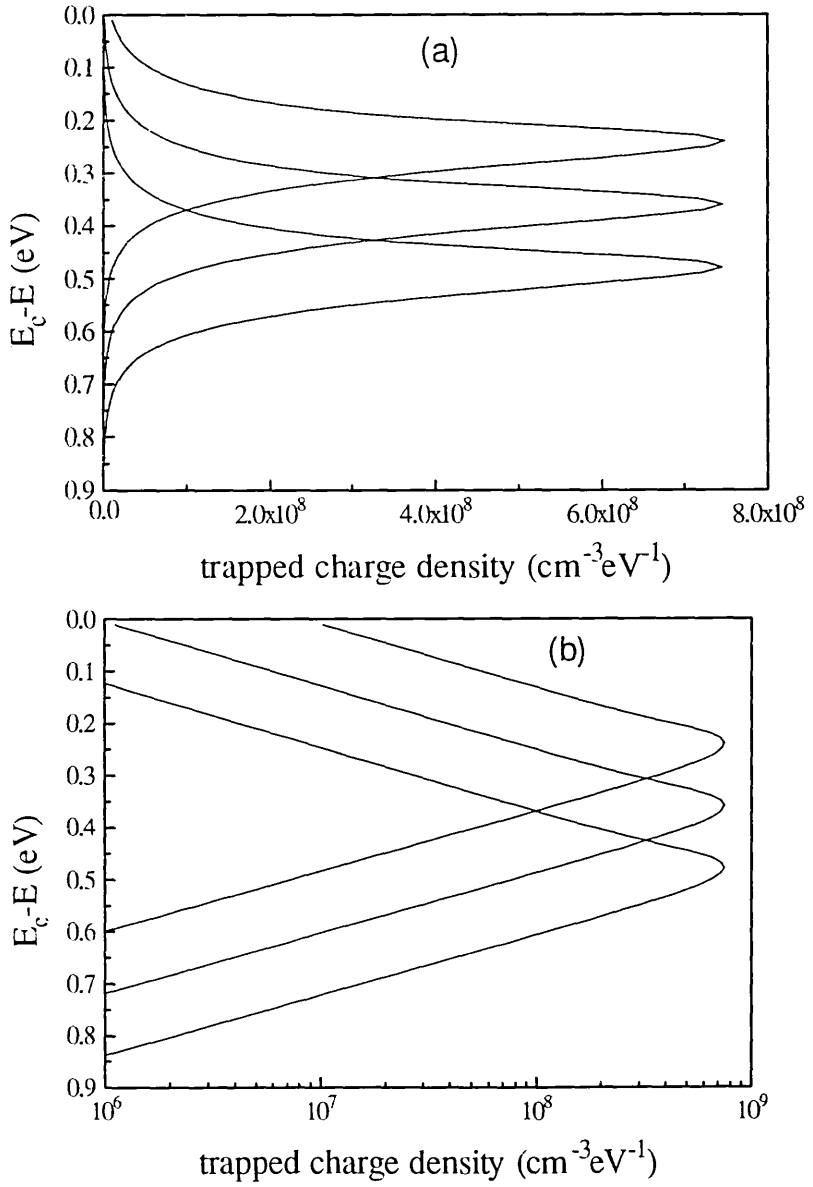

Figure 2.5 Linear (a) and log (b) axis plots of the distribution of trapped charge at successive equally spaced time intervals during a computer simulated TPC decay in a 0.05eV exponential tail. The majority of charge is located in a kT strip at the thermalisation energy E_c-E_{th} which moves deeper into the gap with time.

2.3.2 TROK procedure for obtaining the DOS from measured TPC

If it is desired not to postulate a g(E) equation 2.2 can be recast in an approximate form as

$$\delta N_t \approx kT\delta f_d g(E_c - E_{th}) \qquad (2.5)$$

if it is assumed that the majority of charge is close to E_c-E_{th} . Again eliminating δf_d with equation 2.3 and substituting for E_{th} we obtain

$$g(E_c - E_{th}) = \frac{\delta N_t N_c}{\upsilon kTt\delta n} \qquad (2.6)$$

Thus from a TPC data point ($\delta I(t)$,t), a DOS point {$g(E) \propto (\delta I(t)t)^{-1}$, E_c-$E=kT\ln(\nu t)$} can be obtained.

2.3.3 Limitations of TROK

It is obvious that equation 2.6 gives an incorrect g(E) if the assumption that the charge packet is located at E_c-E_{th} fails. Using the TROK occupation function of figure 2.4 it is easy to conceive of a DOS for which this would be true, for example if there were a bump in the distribution of deep states, which is precisely what is expected for good quality a-Si:H. More subtly such significant structure in the DOS causes the TROK occupation function to be *invalidated.* Marshall and Main (1983) applied equation 2.6 to a computer simulated decay for a DOS consisting of three discrete levels, figure 2.6. The reconstructed DOS shows smearing of the structure over kT, which is to be expected because of the approximation of the shape of the charge packet as a kT wide constant occupation strip. However the energy location and density of the reconstructed levels are wrong, a direct consequence of the assumption that all charge is at E_c-E_{th}.

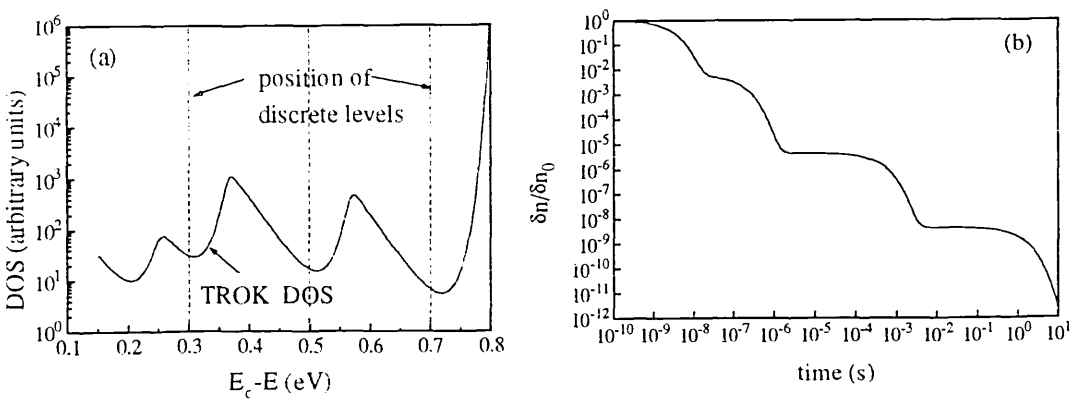

Figure 2.6 (a) DOS recalculated using equation 2.6 from a TPC decay (b) simulated for a DOS consisting of three discrete levels of equal density ($10^{17}cm^{-3}$).

Figure 2.7 illustrates the above argument with a plot of the transient occupation generated by a computer simulation using a DOS with a deep bump at an instant when the majority of charge is located in the bump. The shallow traps are still in quasi-thermal equilibrium with the free states but the occupation at the tail of the Boltzmann distribution is no longer the same as that of the deep states, although E_c-E_{th} still marks the transition from one region to the other. The evolution of the trapped charge distribution in this form of DOS is further examined in §6.2.

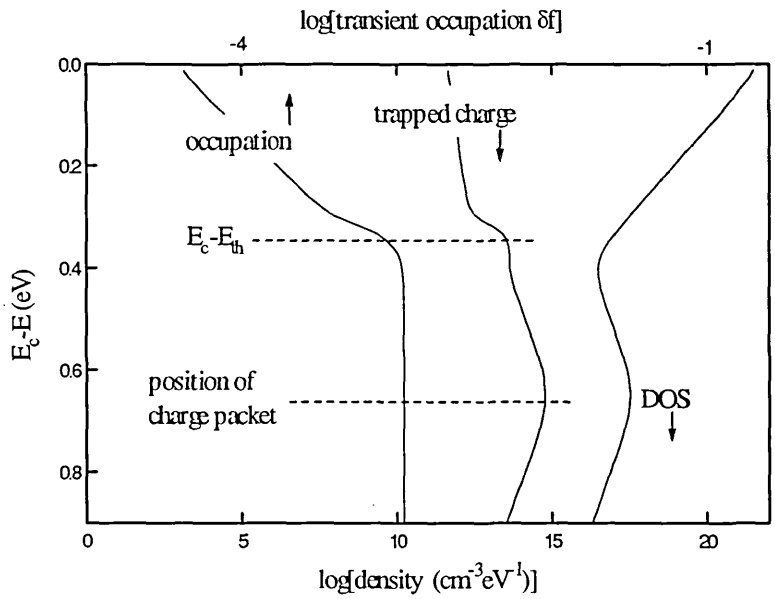

Figure 2.7 Computer simulated transient trapped charge distribution for the DOS shown at an instant when the majority of charge is trapped in the deep bump and not at the thermalisation energy. Note that the occupation function no longer has the TROK form - the occupation in the region just above E_c-E_{th} falls off with an exponential slope much smaller than kT.

2.3.4 Saturation and recombination

The TROK model as presented above is for the case of small occupation of deep traps. When the occupation approaches unity, for example when E_c-E_{th} reaches the Fermi level, thermalisation ceases because the saturated deep states cannot recapture thermally emitted charge. The charge packet is then in quasi-equilibrium with the trap distribution and the observed photocurrent is non-dispersive until recombination begins.

Recombination and deep trapping are competing processes. Deep trapping is dominant at the beginning of a decay, but recombination takes over once the total capture rate into states below E_c-E_{th} has fallen below the recombination rate. The experimentally observed recombination time is thus the release time from traps at a

depth E_R defined by

$$\tau_R^{-1} = C_n \int_{E_v}^{E_R} g(E)dE \qquad (2.7)$$

Equation 2.7 is equivalent to saying recombination occurs when the mean time spent free by carriers equals the recombination time.

The effect of recombination on the charge packet is shown in figure 2.8. The charge packet ceases to thermalise because thermally released carriers recombine rather than become deeply trapped. The current simply reflects the emptying out and removal of deeply trapped charge. Note that as charge is released the shallow energy side of the distribution sharpens in a similar manner to figure 2.7. In fact the effect of a deep bump in the DOS is very similar to that of recombination. Equation 2.7 can be adapted to find the time at which a bump affects the decay by substituting the free trapping time into the bump for τ_R.

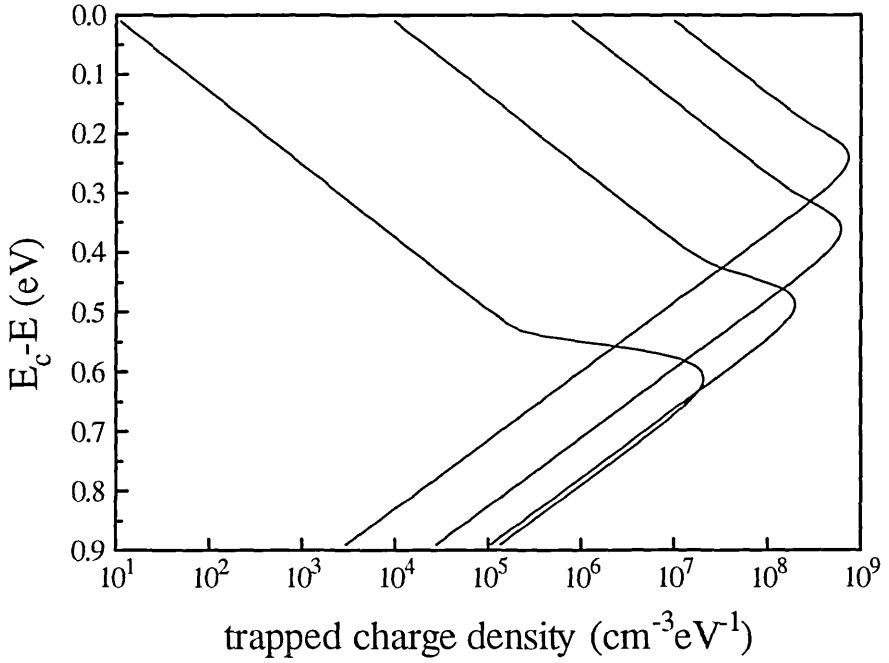

Figure 2.8 The distribution of trapped charge at successive equally spaced time intervals during a computer simulated TPC decay in a 0.05eV exponential tail whilst recombination is occurring. Charge released from traps at the thermalisation energy preferentially recombines so that the occupation of deep traps ceases to increase.

2.3.5 Emission rate treatment of recombination controlled TPC

Orenstein et al (1982) obtained functional forms for recombination in exponential tails, distinguishing between monomolecular, where the excess free carriers have a fixed recombination time, and bimolecular, where the recombination time varies with the excess carrier density, cases. The present author obtains the same time

dependencies with similar magnitude by considering the emission rate of deeply trapped charge.

Since the trapping and release rates for shallow traps are approximately equal we have

$$\frac{d\delta n}{dt} \approx \delta f_d kTg(E_c - E_{th})\nu \exp(-E_{th}/kT) - \frac{\delta n}{\tau_R} \qquad (2.8)$$

the first term on the RHS being the release rate from traps at E_c-E_{th}. We can make the further approximation that $d\delta n/dt$ is much smaller than either of the terms on the RHS and so

$$\delta n \approx \delta f_d kTg(E_c - E_{th})\tau_R / t \qquad (2.9)$$

This expression is analogous to a generation rate multiplied by a recombination time, c.f. equation 1.10. Note that δf_d remains constant during recombination at the value it had when recombination began, c.f. figure 2.8.

For an exponential DOS and monomolecular recombination we obtain

$$\delta n = \delta f_d N_c \nu^{-\alpha} t^{-(1+\alpha)} \tau_R \qquad (2.10)$$

in contrast to the $t^{-(1-\alpha)}$ behaviour prior to recombination. To treat bimolecular recombination we assume the recombination rate to be proportional to the remaining density of transient excess trapped charge

$$\tau_R^{-1} = \delta f_d C_R \int_{E_f}^{E_c - E_{th}} g(E)dE \qquad (2.11)$$

Substituting 2.11 into 2.9 we obtain

$$\delta n = \alpha / C_R t \qquad (2.12)$$

the time dependence of which is independent of T_c. The transition from the pre- to post-recombination régimes is expected to be faster for the monomolecular than the bimolecular process for which τ_R is changing.

Equation 2.9 can also be used for the pre-recombination regime by substituting the trapping time into the distribution below E_c-E_{th}. Again the same time dependence and a similar magnitude are obtained. This approach of relating δn to the emission rate makes clear that the occupation of the tail of the shallow trap Boltzmann distribution and the deep trap occupation are not necessarily the same.

2.4 Volterra equation method

This approach to obtaining g(E) from $\delta I(t)$ was developed by Michiel et al (1983), and has two parts. The first part relates g(E) to the waiting time distribution function $\varphi(t)$, defined such that the probability of release of a trapped carrier from the *whole* trap distribution in the time interval t to t+dt is $\varphi(t)dt$. $\varphi(t)$ is just the average over the distribution of the probability of release in time t to t+dt from traps at depth E to E+dE, p(t,E)dt, weighted by the relative probability of those traps capturing the charge. Thus

$$\varphi(t) = \int g(E)p(t,E)dE \Big/ \int g(E)dE \qquad (2.13)$$

p(t,E) can be obtained from equation 1.14. Solving 2.13 for g(E) is difficult. Matters are much simplified by making the approximation that all charge at a depth E is released at the same time $t(E)^{-1}=\nu\exp[-(E_c-E)/kT)]$. As with TROK this approximation results in the kT blurring of features in the DOS but unlike TROK no "thermalisation energy" significance is attached to E.

The second part of the approach relates $\delta n(t)$ to $\varphi(t)$. Prior to recombination the rate equation for the evolution of the transient free carrier density is

$$d\delta n/dt = (\delta n_0 - \delta n)y(t) - \delta n/\tau_t \qquad (2.14)$$

where δn_0 is the initial transient free carrier density and τ_t the trapping time into the whole DOS. y(t) is the effective release probability function for trapped carriers for the whole trap distribution, given by

$$y(t) = \int_0^t \varphi(t')u(t-t')dt' \qquad (2.15)$$

u(t-t') is the probability that a given carrier was free and became trapped in the time interval (t-t') to (t-t')+dt, i.e.;

$$u(t-t')dt' = \delta n(t-t')dt' \Big/ \delta n_0 \tau_t \qquad (2.16)$$

Combining 2.14-2.16 produces a Volterra integral equation using which $\varphi(t)$, and hence g(E), can be computed numerically from $\delta n(t)$ and $d\delta n(t)/dt$. $\delta n_0$and τ_t must be estimated.

The evaluation of $\varphi(t)$ is computationally intensive, involving a convolution which necessitates constant time steps in the numerical summation. There is

consequentially a practical limitation on the length of decay for which the method can be used. Another limitation is the requirement to estimate values for δn_0 and τ_t.

2.5 The time of flight (TOF) experiment

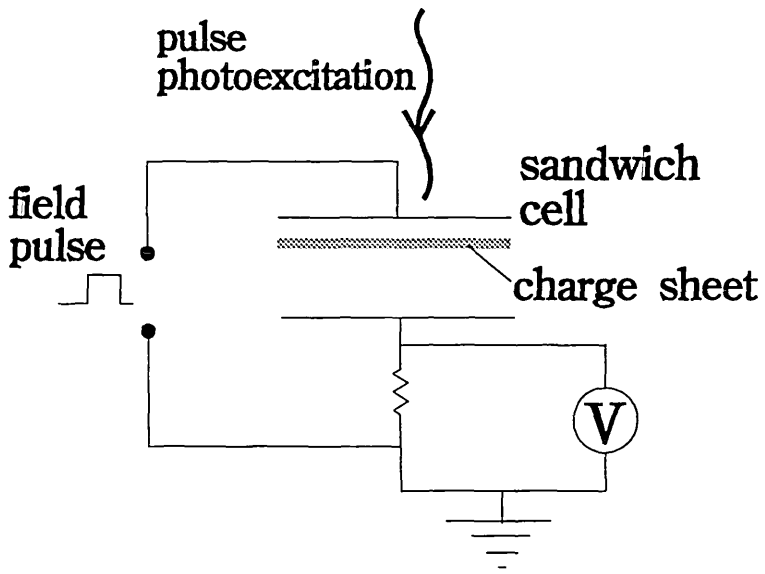

Figure 2.9 The time of flight (TOF) experiment.

Time of flight (TOF) is an experiment closely related to TPC. Figure 2.9 represents the experimental arrangement. The sample is deposited in a sandwich structure consisting of a bottom electrode, a thin film of the material under study and a semitransparent top electrode. A sheet of excess electrons and holes is created close to the top contact by a short pulse of light of a strongly absorbed wavelength. The desired carrier, electrons or holes, can then be caused to drift across the sample by application of a field of the appropriate polarity, the opposite charge of carrier being extracted at the top electrode. To avoid re-injection of charge and space charge effects blocking contacts and a pulsed field are used. The drifting carriers induce a current through the resistor, which ceases when all the excess carriers have been extracted at the bottom electrode. This technique is suitable for use with materials such that the transit time t_t across the specimen is smaller than the recombination time and much smaller than the dielectric relaxation time.

TOF has the advantage that the carrier species can be isolated, whilst TPC conduction is by both electrons and holes, although it is usually assumed that one species dominates. TOF is also less likely to be affected by surface imperfections than TPC. On the other hand the time scale of a TPC experiment is not limited by the dielectric relaxation time because charge neutrality is maintained.

2.5.1 Dispersion

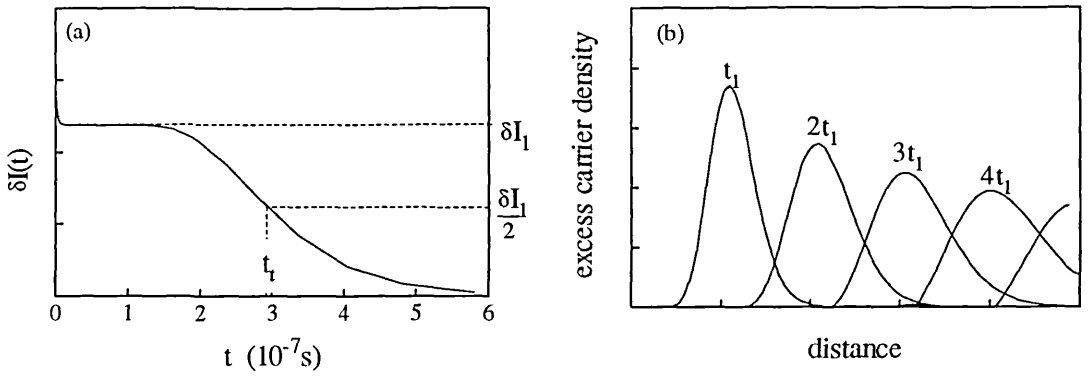

Figure 2.10 (a) Computer simulated conventionally dispersive current decay as would be observed in a TOF experiment with a crystalline sample, (b) spatial excess charge distribution in the sample at successive equally spaced intervals during the decay.

Figure 2.10(a) illustrates the *conventionally dispersive* current observed in TOF with a crystalline sample. The current is constant until the carriers begin to arrive at the bottom electrode. The carriers have a distribution of arrival times because scattering creates a statistical spread in the carrier velocities, so that the current does not cease abruptly. The average transit time t_t is that at which 50% of the carriers have been collected, from which the average drift mobility μ_d can be calculated:

$$\mu_d = \frac{l}{t_t \varepsilon} \qquad (2.17)$$

l being the drift distance and ε the field. The drifting charge spatial distribution is illustrated in figure 2.10(b). The r.m.s. width of the distribution increases with time but the peak of the distribution, which coincides with the average carrier displacement, moves at a constant velocity, i.e.; μ_d is *constant* so t_t is proportional to ε and l.

A typical TOF signal observed in an amorphous material exhibits *anomalous* dispersion, figure 2.11(a). The short time signal is the same as would be observed in TPC. The long time signal is similar to TPC when monomolecular recombination is occurring. The transit time t_t, taken from when the behaviour of the decay changes, is not linearly proportional to l or E. Figure 2.11(b) shows the spatial distribution of charge for a multiple trapping model, the peak in the carrier density remains close to the top electrode, does not progress linearly with time and does not coincide with the average carrier displacement. In the multiple trapping model this behaviour is a consequence of the process of equilibration of the transient charge with the trap distribution The signature is that the drift mobility *varies* with ε and l.

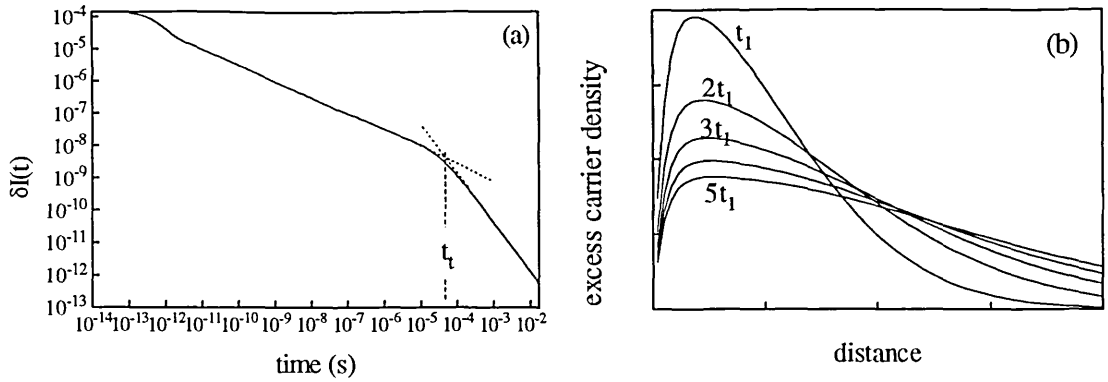

Figure 2.11 (a) Computer simulated anomalously dispersive current decay for a TOF experiment, (b) spatial excess charge distribution in the sample at successive equally spaced intervals during the decay. Note that the peak in the distribution is stationary.

The extraction of charge at the bottom electrode plays the same rôle as monomolecular recombination, so t_t can be related to the DOS by a similar equation to 2.7, replacing the recombination time with the free transit time t_f, the length of time a carrier must spend in free states to traverse the sample. Marshall et al (1987) use this relation for t_f as the basis for a method of determining the DOS. For a particular specimen t_f can be controlled by varying the field, and the thermalisation energy, defined in a different way to TROK, determined for a particular field from the activation energy of μ_d. The technique is labour intensive, requiring many TOF experiments at different temperatures to probe a single energy. Additionally the time scale of the experiment and hence the energy depth which can be probed is limited by the dielectric relaxation time.

The method of *post-transit spectroscopy* (Seynhaeve et al, 1989) uses the TOF post transit current to calculate g(E). The post transit current reflects the emptying out of deeply trapped charge, i.e.; $\varphi(t) \propto \delta n_t$, and is insensitive to the collapse of the internal field so that δn can be measured to long times. The DOS can be thus be calculated using equation 2.13.

2.6 Numerical computer simulation

The rate equations for transport in the multiple trapping model can be solved numerically for $\delta n(t)$, $\delta p(t)$ and the trapped charge densities (Main et al, 1991). The solution may be found for arbitrary distributions of tail states, correlated states and energy dependent capture coefficient profile, and for transient, modulated (see chapter 3) steady state and transient with optical bias photoconductivity. Numerical modelling is used extensively in this work mainly as a tool to provide insight into physical processes through qualitative rather than quantitative matching with experiment. Further details of the modelling procedure and of the model parameters used in this work are contained in appendix A.

The attempts described in chapter 2 to formulate a method of calculating the DOS from TPC measurements have had to cope with the dependence of the occupation of deep states on the *whole* history of the decay. Thus any such method which attempts to make a one to one mapping between a single (δI,t) data point and a (g(E),E) point in the DOS distribution must fail in the general case. However an analogous mapping *is* possible for data points (I_ω,θ,ω) from the modulated photocurrent experiment.

3.1 Description of the experiment

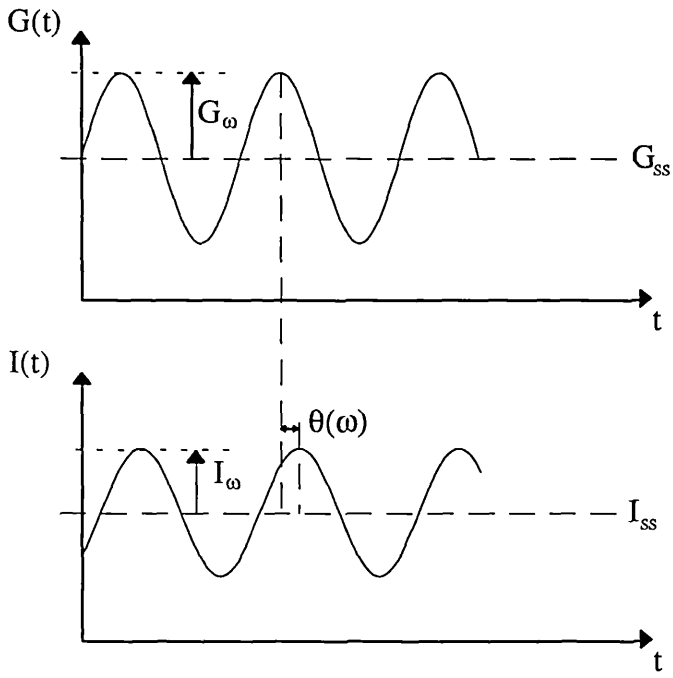

Figure 3.1 The MPC experiment. The generation rate G in the sample is sinusoidally modulated by modulating the intensity of the excitation light, and a sinusoidally modulated photocurrent $I_{ss}+I_\omega \sin[\omega t+\theta_\omega]$ is observed.

MPC can be performed with a coplanar or sandwich sample, in the following the coplanar configuration is assumed. The specimen is illuminated with super band gap energy light the intensity of which is modulated with a sine wave, figure 3.1. The generation rate G(t) may be represented as the sum of a steady state term G_{ss} and the real part of an alternating component of angular frequency ω and amplitude G_ω, $\Re[G_\omega \exp(i\omega t)]$. The ratio of the complex magnitude to the steady state magnitude G_ω/G_{ss} is referred to as the modulation index and is expressed as a percentage.

Amorphous materials are observed to respond sine wave modulated illumination with a sine wave modulated photocurrent which is phase shifted by a frequency dependent angle $\theta(\omega)$ with respect to the excitation and which has a frequency

dependent complex amplitude $I_\omega(\omega)$. The MPC experiment consists of sampling the complex photocurrent spectrum (I_ω,θ,ω) by means of a phase sensitive detector for a range in frequency typically 1-10^5 Hz. The mean value of the photocurrent I_{ss} is independent of the modulation frequency if the modulation index is made small enough, ideally having the same magnitude as the steady state photocurrent measured at generation rate G_{ss}.

3.2 Multiple trapping analysis

The analysis presented here is a résumé of that given by Oheda (1981). As in the treatments for TPC in chapter 2 it is assumed that transport is a multiple trapping process, i.e.; current is carried solely by carriers in free states which interact through trapping and release with the trap distribution. It is further assumed that the influence of the states below the quasi-Fermi level may be represented as a monomolecular recombination time τ_n for high enough frequency. This will be true even for a material exhibiting bimolecular behaviour if the modulation index is sufficiently small, the recombination time being determined by the mean excitation. A fuller treatment valid for low frequency/deep states is discussed in §3.4.

The rate equations are

$$\frac{dn}{dt} = G_{ss} + G_\omega e^{i\omega t} - \int_{E_{tn}}^{E_c} \frac{dn_t}{dt} dE - \frac{n - n_d}{\tau_n} \qquad (3.1)$$

for free electrons and

$$\frac{dn_t(E)}{dt} = nC_n\left(g(E) - n_t(E)\right) - \bar{n}(E)C_n n_t(E) \qquad (3.2)$$

for trapped electrons. The solutions are expected to be of the form

$$n(\omega) = n_{ss} + n_\omega(\omega)e^{i\omega t} \qquad (3.3)$$

$$n_t(E,\omega) = n_{tss}(E) + n_{t\omega}(E,\omega)e^{i\omega t} \qquad (3.4)$$

n_ω and $n_{t\omega}$ being complex functions. Substituting into the rate equations and making the linearisation approximation that terms in $e^{2i\omega t}$ can be ignored yields

$$n_\omega = \frac{G_\omega}{\left(A^2 + B^2\right)^{\frac{1}{2}} e^{i\phi}}$$

$$\tan(\phi) = B/A \qquad (3.5)$$

where A and B are real and are given by

$$A(\omega) = \frac{1}{\tau_n} + c_n \int_{E_{tn}}^{E_c} (1-f)g(E)\left\{\frac{\omega^2}{(\omega_e+\omega_n)^2+\omega^2}\right\}dE \qquad (3.6)$$

$$B(\omega) = \omega + c_n \int_{E_{tn}}^{E_c} (1-f)g(E)\left\{\frac{\omega(\omega_e+\omega_n)}{(\omega_e+\omega_n)^2+\omega^2}\right\}dE \qquad (3.7)$$

where $\omega_e=e_n$ and $\omega_n=nC_n$. It may save confusion later to point out that A and B are not themselves the real and imaginary parts of n_ω, although their ratio *is* the tangent of *minus* the phase shift; so $\phi=-\theta$. Equations 3.5-3.7 are easily generalised to a DOS with more than one species of states, i.e.; with several distributions of states having different trapping coefficients, by integrating separately over each distribution and summing in equations 3.6 and 3.7 (see appendix B).

A very clear relationship between ϕ and g(E) can be discerned by investigating the energy dependence of the weighting functions in the curly brackets operating on the effective DOS (1-f)g(E) in the integrals in equations 3.6 and 3.7. We define

$$W_A(\omega,E) = \frac{\omega^2}{(\omega_e+\omega_n)^2+\omega^2} \qquad (3.8)$$

$$W_B(\omega,E) = \frac{\omega(\omega_e+\omega_n)}{(\omega_e+\omega_n)^2+\omega^2} \qquad (3.9)$$

W_A and W_B are illustrated graphically in figure 3.2 for an angular frequency $\omega>>\omega_n$. W_B is sharply peaked at an energy E_c-E_ω such that

$$E_\omega = kT\ln(\upsilon/\omega) \qquad (3.10)$$

and has kT skirts. Thus the weighting function W_B emphasises states at E_c-E_ω. Note that the mean release time from states at E_c-E_ω is $1/\omega$, which is reminiscent of the definition for E_{th}, equation 2.1. However the definition of E_ω has been arrived at *without making any assumptions about the shape of the DOS.* W_A is flat below E_c-E_ω and has a kT/2 skirt above. When the integral terms in equations 3.8 and 3.9 dominate the tangent of the phase shift is approximately the ratio of the density of states at the thermal emission related energy E_c-E_ω to the integrated density of states below E_c-E_ω. If we approximate W_B by a delta function, W_A by a step function rising at E_c-E_ω, and normalise

to the integrals of W_B and W_A, we can write

$$\tan(\phi) \approx \frac{\omega + \frac{\pi}{2} kTC_n g(E_c - E_\omega)}{1/\tau_n + C_n \int_{E_{tn}}^{E_c - E_\omega} g(E)dE} \tag{3.11}$$

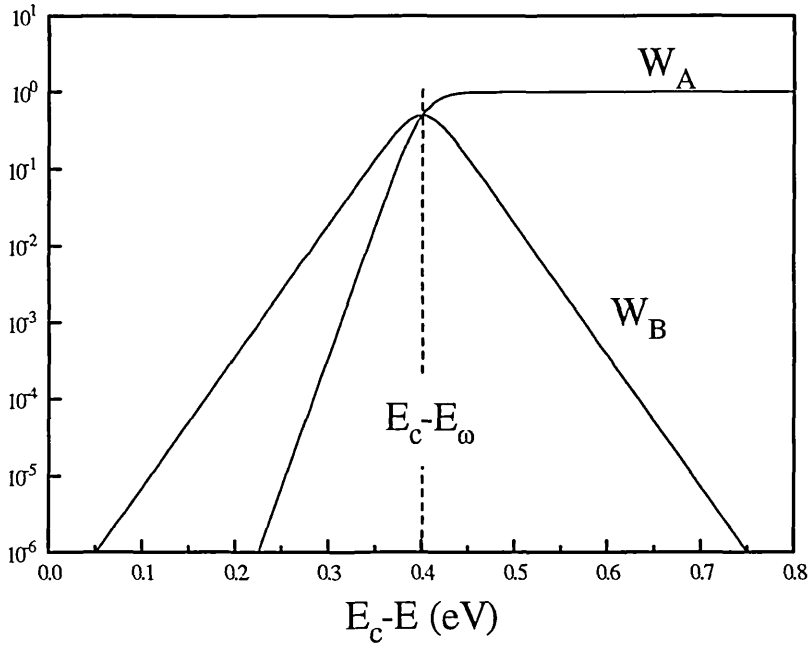

Figure 3.2 The weighting functions W_A and W_B calculated for E_w=0.4eV, T=300K and $\omega_n << \omega$.

3.3 Calculation of the DOS from MPC spectra

In his 1981 paper Oheda went on to derive a recursive procedure to calculate the DOS from phase spectra only. Brüggemann et al (1990) demonstrated that the recursion tends to amplify even a small amount of noise in the experimentally measured spectra to produce a substantially incorrect DOS. They proposed an alternative method of calculation using *both* the MPC complex magnitude and phase spectra to determine the value of B and hence g(E). Making the delta function approximation for W_B we can write:

$$g(E) \approx \frac{B - \omega}{\frac{\pi}{2} kTC_n} = \frac{2}{\pi kTC_n} \left\{ \frac{G_\omega \sin(\phi)}{|n_\omega|} - \omega \right\} \tag{3.12}$$

In general the explicit ω can be ignored for experimentally accessible frequencies. It is emphasised that equation 3.12 has been derived without making any assumptions about the form of g(E). The delta function at E_c-E_ω approximation for W_B and hence equation 3.12 is valid for angular frequencies such that $(1\text{-}f(E_c\text{-}E_\omega)) \approx 1$, i.e.; $\omega >> \omega_n$. The MPC spectrum at low frequencies is independent of $g(E_c\text{-}E_\omega)$, see §3.4 below.

Equations 3.6 and 3.7 can be used in their exact form to calculate the MPC spectrum for the 3 discrete levels DOS of figure 2.6 used to test the TROK interpretative scheme in chapter 2. The DOS recomputed from the spectrum using equation 3.12, figure 3.3, places the levels at the correct energies and with the correct integrated densities. The kT skirts of the recomputed levels are a result of the delta function approximation for W_B.

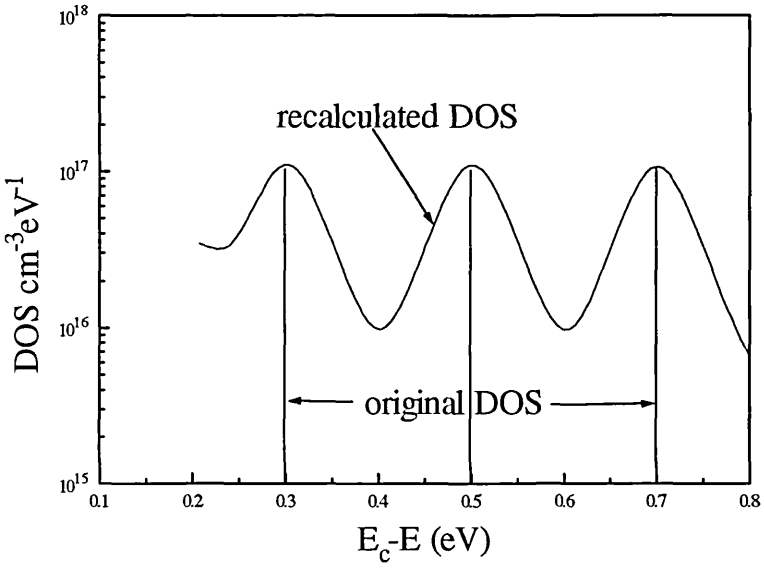

Figure 3.3 DOS recalculated from MPC spectrum calculated using equation 3.12 for an original DOS consisting of three discrete levels of density $10^{17}cm^{-3}$. The calculated phase spectrum is presented in figure 4.10.

The broadening effect is reduced in another calculation method devised by Hattori et al (1991) who use W_A rather than W_B. W_A has the advantage that it has a sharper fall off, kT/2, on the shallow energy side. However W_A does not fall off on the deep energy side so the differential dA/dlnω must be used to regain the energy selectivity.

$$g(E) \approx \frac{dA/d(\ln\omega)}{C_n kT} = \frac{1}{C_n kT}\frac{d}{d(\ln\omega)}\left[\frac{\cos(\phi)}{|n_\omega|}\right] \qquad (3.13)$$

Using a differential has the disadvantage of making the computed DOS more sensitive to noise in the measured spectrum.

3.4 Low frequency analysis

3.4.1 Extension of Oheda analysis

Oheda's original analysis represents the effects of hole transitions between gap states and the valence band by a recombination time. This approximation might be

expected to be valid for angular frequencies $\omega >> \omega_n$ where the weighting functions emphasise states at energies more than kT above E_{tn} for which the electron transition rates are much larger than the hole rates. Nevertheless the behaviour of equations 3.6-3.9 for low frequencies are investigated here because comparison (see §8.2) with the behaviour of the fuller analysis of §3.4.2 below suggests that the differences introduced by including hole transitions may not be great.

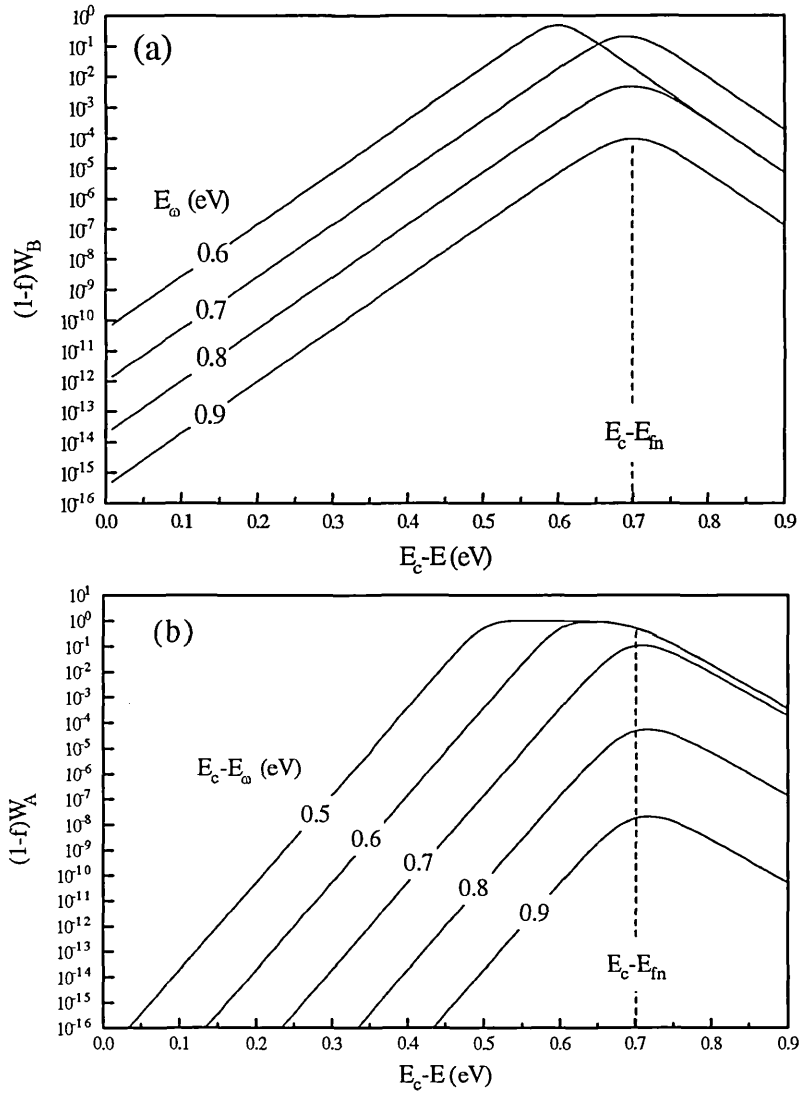

Figure 3.4 (a) $(1\text{-f})W_B$ and (b) $(1\text{-f})W_A$ calculated for the indicated values of E_ω and E_{fn}, demonstrating the loss of energy selectivity for $E_\omega > E_c - E_{fn}$.

Inspection of equations 3.8 and 3.9 for the weighting functions, reveals that for $\omega << \omega_n$ the denominator is independent of ω. The energy dependences of W_B and W_A are therefore independent of ω, as is illustrated by figures 3.4(a) and (b). The break point of $(1\text{-f})W_A$ and the peak of $(1\text{-f})W_B$ "stick" at $E_c - E_{tn}$ and ω serves only to scale the magnitude of the weighting functions. Consequently MPC measurements cannot be used to map the DOS below the trap quasi-Fermi level. As ω decreases the contributions of

the integral terms in equations 3.6 and 3.7 for A and B decrease. At low enough frequency A takes a frequency independent value of $1/\tau_n$, but B continues to decrease. When B<<A, $n_\omega \approx G_\omega/A = G_\omega \tau_n$, as expected for a slow variation in photogeneration magnitude.

An analytic form for B for $\omega << \omega_n$ can be obtained by integrating the $(1-f)W_B$ product over energy and again approximating with a scaled delta function. Using the thermal equilibrium form for f (and hence $E_{tn}=E_{fn}$) we can write $(1-f)=\omega_e/(\omega_e+\omega_n)$ and so

$$B(\omega << \omega_n) \approx C_n g(E_{fn}) \int_{E_v}^{E_c} \left(\frac{\omega_e}{\omega_e + \omega_n} \right) \left\{ \frac{\omega}{\omega_e + \omega_n} \right\} dE \approx \frac{\omega kTg(E_{fn})}{n_{ss}} \qquad (3.14)$$

i.e.; $B \propto \omega$.

3.4.2 Other MPC analyses

A full treatment of MPC including both electron and hole transitions for single valence states has been given by Hattori et al (1994). Proceeding from their result for n_ω and making suitable approximations, see appendix B, we may derive for $\omega << \omega_n$

$$B \approx \omega C_n \frac{kT}{2} \frac{(\omega_n + 2\omega_p)}{(\omega_n + \omega_p)^2} \qquad (3.15)$$

where B is as defined in equation 3.5 and $\omega_p = p_{ss} C_p$. Note that although Hattori et al are able to derive an analytic expression for n_ω, values for n_{ss} and p_{ss} must be found numerically for a particular g(E) and G_{ss}.

In the paper of Hattori et al and in this work it is assumed that for small G_ω each charge state of dangling bonds can be regarded as a separate set of single valence states, the relative abundances of each charge state being determined by the steady state generation. Longeaud and Kleider (1993) by contrast have properly treated MPC for double valence states. Their work is not further considered here.

Chapter 4 Fourier transform method

A simple procedure to obtain accurately the density of states from the modulated photocurrent spectrum has been demonstrated in chapter three. Unfortunately MPC has the experimental drawback that electromagnetic coupling effects limit measurements to a range in frequency of about $1\text{-}10^5$ Hz , see §5.3.3, thus the DOS may only be probed over a limited range of energy at any one temperature. By contrast TPC may be measured over 10 or more orders of magnitude of time and current. The possibility suggests itself of obtaining an accurate, wide energy range probe for the DOS by combining the MPC analysis with the TPC experiment by the use of a *Fourier transform.*

4.1 Mathematical basis

To achieve this the MPC interpretative scheme must be recast in terms of the TPC Fourier transform spectrum, see Main et al (1992) and Pandya and Schiff (1985). The semiconductor may be regarded as a system where the generation rate is the input and the photocurrent the output. Fourier transform theory can be applied in the regime where the system response is linear. The complex transfer function $H(\omega)$ of the semiconductor can be defined as the spectral response to sinusoidal input generation rate of unit amplitude, thus the MPC spectrum for sinusoidal magnitude G_ω is $n_\omega(\omega) = G_\omega H(\omega)$. Substituting for n_ω in equation 3.12 gives

$$g(E) = \frac{2}{C_n \pi k T}\left\{\frac{\sin\phi(\omega)}{|H(\omega)|} - \omega\right\} \qquad (4.1)$$

where $H(\omega) = |H|e^{-i\phi}$

At times much longer than the duration of the photogeneration pulse the TPC decay n(t) can be regarded as the response of the semiconductor to an impulse generation $G(t)=\delta G\delta(t)$. If the pulse magnitude δG is small enough that the current magnitude varies linearly with δG we can define a unit impulse response function $h(t) = n(t)/\delta G$. Fourier transform theory states that

$$H(\omega) = \mathcal{F}[h(t)] = \delta G^{-1}\mathcal{F}[n(t)] \qquad (4.2)$$

Thus if the Fourier transform of a TPC decay can be calculated the DOS can be obtained from equation 4.1. Note that the steady state component of the MPC generation rate does not appear explicitly above. In fact the steady state generation rate alters the form of the response functions h(t) and $H(\omega)$. This leads to the intriguing notion that the Fourier transform of a TPC decay without optical bias is equivalent to an MPC spectrum for zero mean generation rate.

4.2 Calculation of the Fourier transform

The methods described here have been duplicated independently by Melcher and Schiff (unpublished). The numerical calculation of the Fourier transform is not trivial. Standard digital FFT methods rely on a constant sampling interval, whereas a set of TPC $\{i(t_k),t_k\}$ data covers typically ten orders of magnitude in time with non uniform intervals.

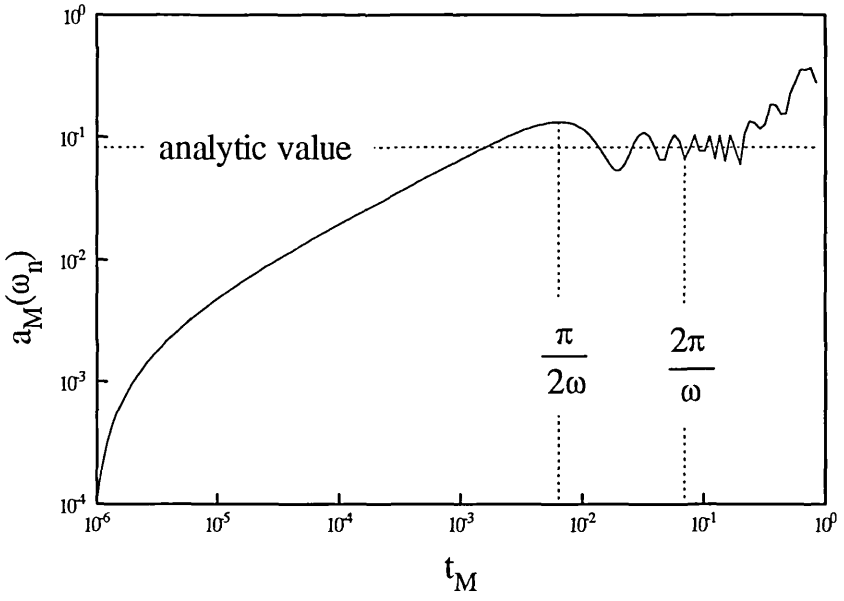

Figure 4.1 The variation with t_M of the first order approximation to the real part of the Fourier transform (equation 4.3) of $t^{-1/2}$, summation performed between 10^{-6} and t_M for ω=231radians.

The simplest approach is to evaluate the first order approximation to the integrals for the real and imaginary parts of the Fourier transform for selected frequencies ω_n If there are M data points then

$$\Re e\{H(\omega_n)\} \approx a_n(\omega_n) = \delta G^{-1} \sum_{k=2}^{M-1} n(t_k)\cos(\omega_n t_k)\Delta t_k \qquad (4.3)$$

$$\Im m\{H(\omega_n)\} \approx b(\omega_n) = \delta G^{-1} \sum_{k=2}^{M-1} n(t_k)\sin(\omega_n t_k)\Delta t_k \qquad (4.4)$$

where $\Delta t_k=0.5(t_{k-1}-t_k)$. Figure 4.1 shows the variation of the sum $a(\omega_n)$ with increasing t_M for sets of numbers generated by a power decay function, $(t_k^{-1/2},t_k)$, $t_{k+1}/t_k=1.1$, evaluated for $\omega_n = (t_1 t_M)^{-\frac{1}{2}}$. A power law is chosen as a test function because TPC decays observed in amorphous materials are generally of this form. An analytic expression for the Fourier integral of a power law $t^{-\rho}$ for $0<\rho<1$ over the range t=0 to ∞ can be found in reference books (Spiegel, 1974), the phase is frequency invariant and is just $(1-\rho)\pi/2$. The integral reaches the correct order of magnitude within one quarter

oscillation of $\cos(\omega_n t)$. The sum then oscillates about and converges on the analytic value. At long times however the value of the sum wanders because of aliasing, i.e.; because the sample interval is comparable to or longer than the period of $\cos(\omega_n t)$.

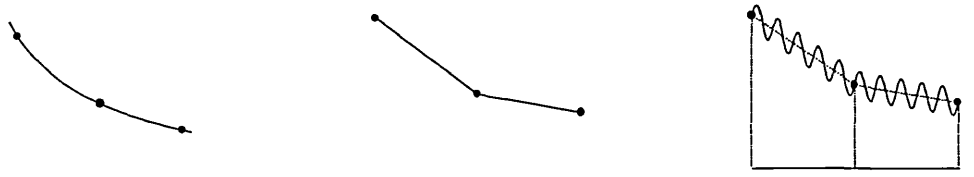

Original function | Linear spline interpolated *approximate* function | Contribution to Fourier transform summation

Figure 4.2 The principle of the improved method of calculating the Fourier transform using linear spline interpolation, equations 4.5 and 4.6.

The aliasing problem can be eliminated by changing the summation to find the *exact* transform of a linear spline interpolated *approximation* to the TPC decay. This is to say the approximations to the Fourier integrals consist of the sum of exact Fourier integrals of straight line segments joining the data points, figure 4.2. The summations can be written as

$$\Re_e\{H(\omega_n)\} \approx a(\omega_n) = (\delta G \omega_n)^{-1} \sum_{k=2}^{M} \left\{ \begin{array}{l} \frac{s_k}{\omega_n}\left[\cos(\omega_n t_k) - \cos(\omega_n t_{k-1})\right] \\ +\left[n_k \sin(\omega_n t_k) - n_{k-1}\sin(\omega_n t_{k-1})\right] \end{array} \right\} \qquad (4.5)$$

$$\Im_m\{H(\omega_n)\} \approx b(\omega_n) = (\delta G \omega_n)^{-1} \sum_{k=2}^{M} \left\{ \begin{array}{l} \frac{s_k}{\omega_n}\left[\sin(\omega_n t_k) - \sin(\omega_n t_{k-1})\right] \\ -\left[n_k \cos(\omega_n t_k) - n_{k-1}\cos(\omega_n t_{k-1})\right] \end{array} \right\} \qquad (4.6)$$

where $s_k=(n_k-n_{k-1})/(t_k-t_{k-1})$. Figure 4.3 shows the improvement in the approach of the approximation to a final value. It might be thought that using a power law interpolation would be more appropriate for the generally encountered forms of TPC decays, however an analytic form for the Fourier integral of a power law between arbitrary limits appears not to exist.

4.3 Evaluation of the numerical Fourier transform

Even if the Fourier transform could be computed to perfect accuracy it is necessarily only an approximation to the complex transfer function unless the TPC

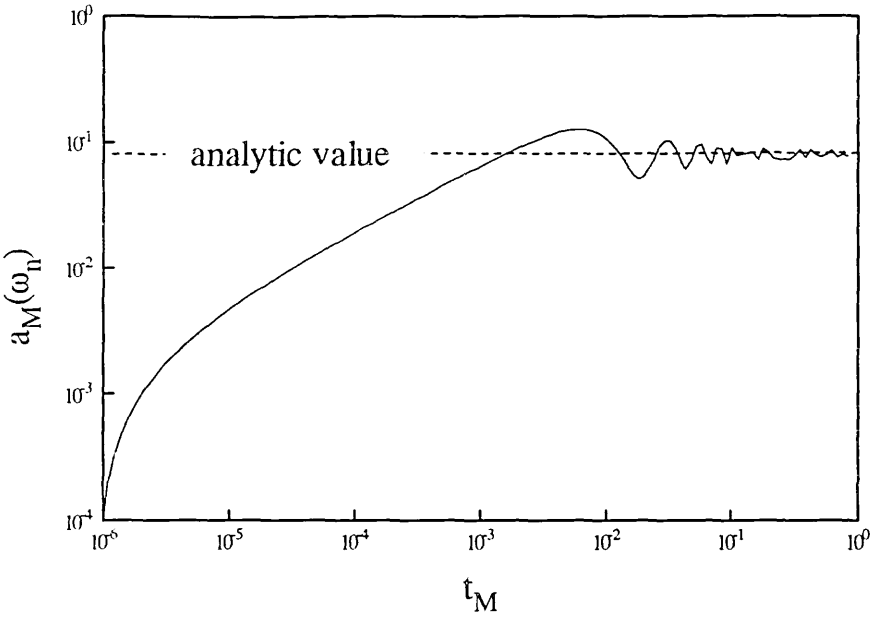

Figure 4.3 The variation with t_M of the linear spline interpolation approximation to the real part of the Fourier transform (equation 4.5) of $t^{-1/2}$, summation performed between 10^{-6}s and t_M for ω=231rads

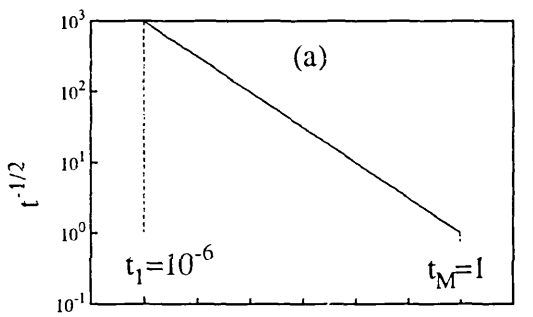

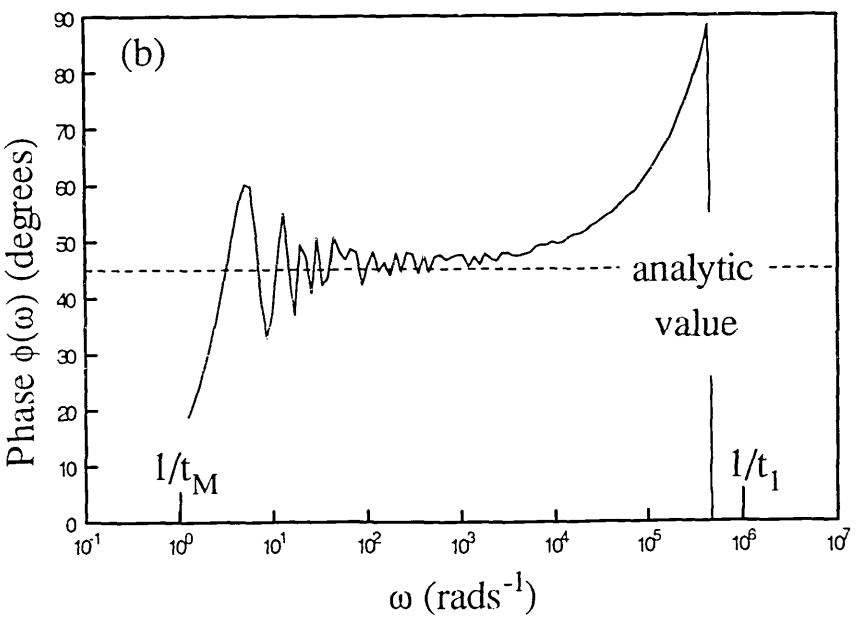

Figure 4.4 (b) Fourier transform phase spectrum calculated for the $t^{-1/2}$ power law decay data set of (a) using equations 4.5 and 4.6.

signal is captured in its entirety, which is experimentally not possible. However it might be expected that the transform would be a good approximation for a "reasonable" range of frequency $1/t_M<\omega<1/t_1$. Figure 4.4(b) shows the Fourier transform phase calculated from the $(t_k^{-1/2},t_k)$ number set of figure 4.4(a) using equations 4.5 and 4.6. From this point on it may be assumed numeric Fourier transforms referred to in this work have been calculated using equations 4.5 and 4.6. The transform phase takes the analytic value of $\pi/2\equiv45°$ in the middle of the "reasonable" range but departs at the limits. At the $1/t_M$ end the oscillation is caused by the abrupt truncation of the number set, as figure 4.5 illustrates. The period of the sin and cos functions in the summations is commensurate with the truncation time t_M, but the peaks and troughs of the functions coincide with t_M for different values of the angular frequency, so causing the phase to shift above and below the analytic value. The oscillation can be removed by artificially causing the photocurrent to tend smoothly to zero at the long time end by multiplying by an apodisation function. The function used in this work is the Gaussian

$$Q(t_k) = e^{-c(t_k/t_M)^2} \qquad (4.7)$$

where typically c is chosen to be 5. Figure 4.6 shows the improvement in the calculated phase spectrum using $(Q(t_k)t^{-1/2},t_k)$. The use of Q with experimental data should only be necessary if capture has not occurred to long enough times to observe final recombination.

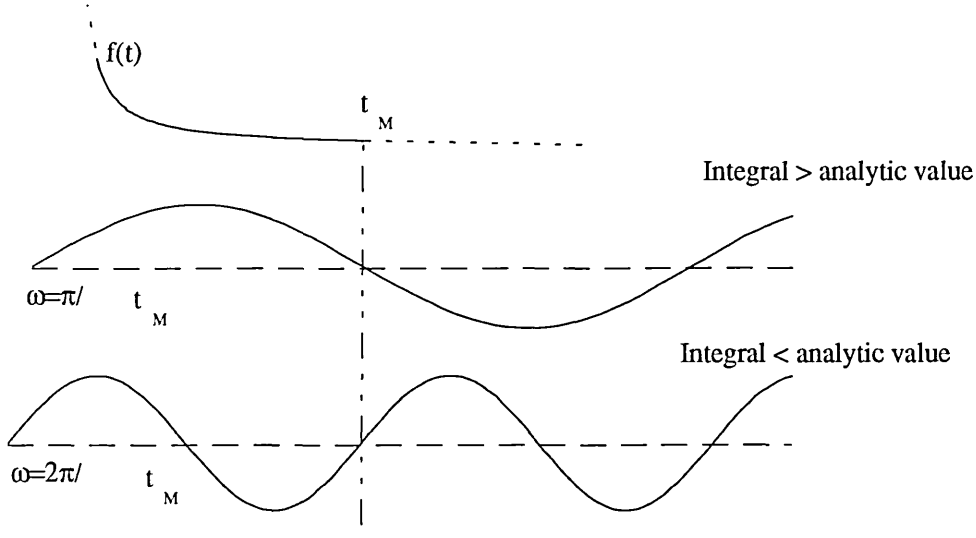

Figure 4.5 The origin of low frequency oscillation in phase in the abrupt long time termination of f(t) at t_M. The missing contribution to the sine function-f(t) product integral from the truncated portion of f(t) can be positive or negative depending on the relation between t_M and ω.

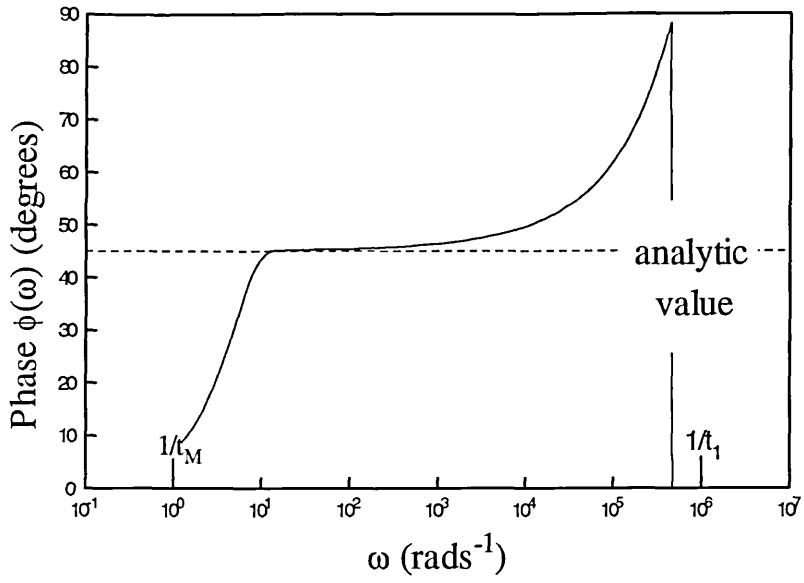

Figure 4.6 The improvement to the calculated phase spectrum of figure 4.4 obtained by first applying an apodisation function to the number set. The low frequency oscillations have disappeared.

The rise of the computed phase above 45° at the $1/t_1$ end is not so easy to deal with. It is a consequence of the missing contributions to the summation from the portions of the $t^{-1/2}$ decay not sampled by the data set. Figure 4.7 attempts to illustrate why the phase rises; the product $t^{-1/2}\cos(\omega_n)$ is much larger than $t^{-1/2}\sin(\omega_n)$ at small t and large ω_n, so that, compared to $b(\omega_n)$, $a(\omega_n)$ is relatively much smaller than its analytic value, making the computed phase $\tan^{-1}(b/a)$ larger than the analytic value. The error is worse for a larger power, see figure 4.8, for $\rho=0.9$ the computed phase is affected at a frequency 5 orders smaller than $1/t_1$. This property, of a feature at time t affecting the transform at a frequency many orders smaller than 1/t, is *fundamentally necessary* to the task of physical interpretation for which we are employing Fourier analysis. The occupation of deep states is dependent on the whole history of the TPC decay, so information on states at an energy depth with release time t is contained in the decay at times $<<t$. The distortion of the computed transform is greater the larger is the size of the contribution to the exact Fourier integral associated with the missing short time data. This is why the distortion in figure 4.8 gets worse as ρ gets larger, because the relative contribution to the integrals from data at $t<t_1$ gets larger.

The task of calculating the transform of real experimental data is actually easier than dealing with a power law because the TPC signal has a maximum theoretical value - the pre-trapping current, i.e.; the current when virtually all the pulse generated charge is still in free states. The ideal would be to capture data at short enough times to see the pre-trapping photocurrent. This is not possible with the equipment (and time duration of laser pulse) used, but it is possible to estimate the magnitude of the pre-trapping current without making any more assumptions than those necessary to scale the computed DOS, and hence estimate the maximum size of the missing contribution to the Fourier

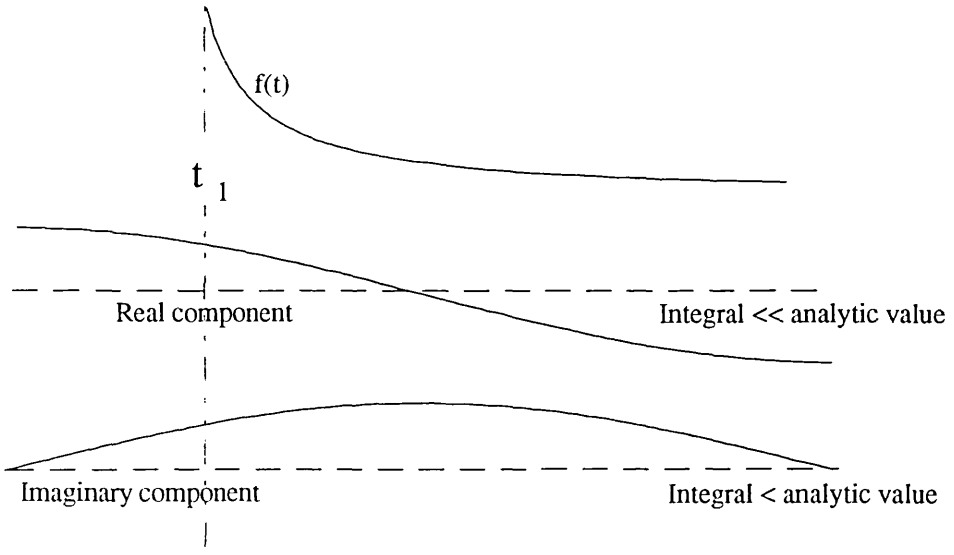

Figure 4.7 The origin of the high frequency phase error in the calculated spectrum. The missing contribution to the real component of the Fourier transform sum from f(t) at $t<t_1$ for ω commensurate with $1/t_1$ is much larger for the real component than the imaginary component because the cosine function takes its largest values at small ωt, but the sine function its smallest values.

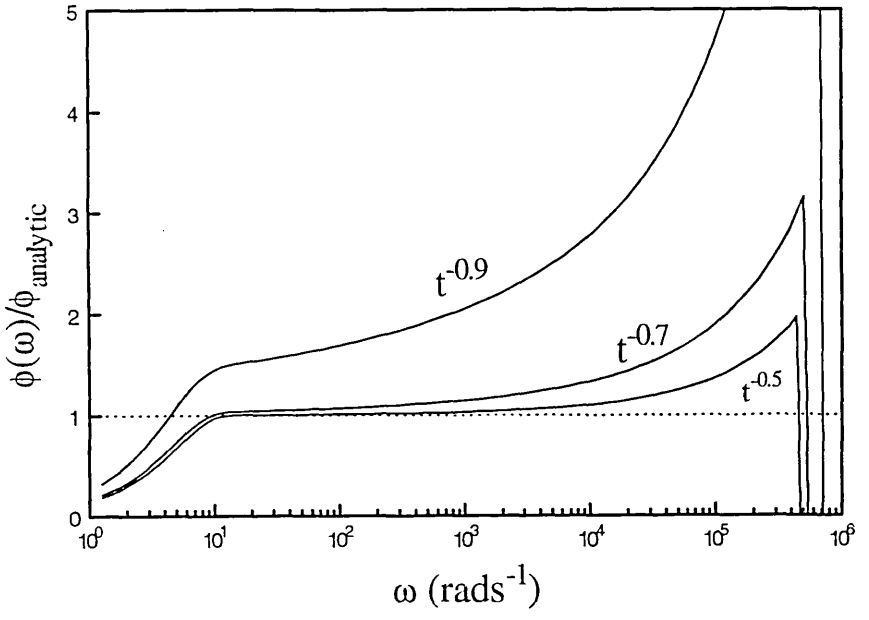

Figure 4.8 The calculated Fourier transform phase spectra normalised to the analytic values for three different power law decays.

summations. This point is further covered in the discussion of the application of the Fourier transform method to TPC data measured in undoped a-Si:H in chapter 6.

A final check on the robustness of the summation is to look at effect of varying the data sampling interval t_{k+1}/t_k. Figure 4.9(a) and (b) compare the transform of the $t^{-0.9}$ decay using t_{k+1}/t_k=1.1 and 10. Despite the severity of using a very steep decay with such a large interval the summation still reproduces the general shape of the smaller interval curves. The real and imaginary parts of the large interval spectrum are about a factor of five too large because the integral under a straight line joining two points is greater than that under a power law, but the error cancels in calculating the phase. Reducing the interval to smaller than 1.1 does not affect the summation. Experimentally an interval of 1.1 is aimed for but the summation is insensitive to an irregular interval so no great care has to be taken.

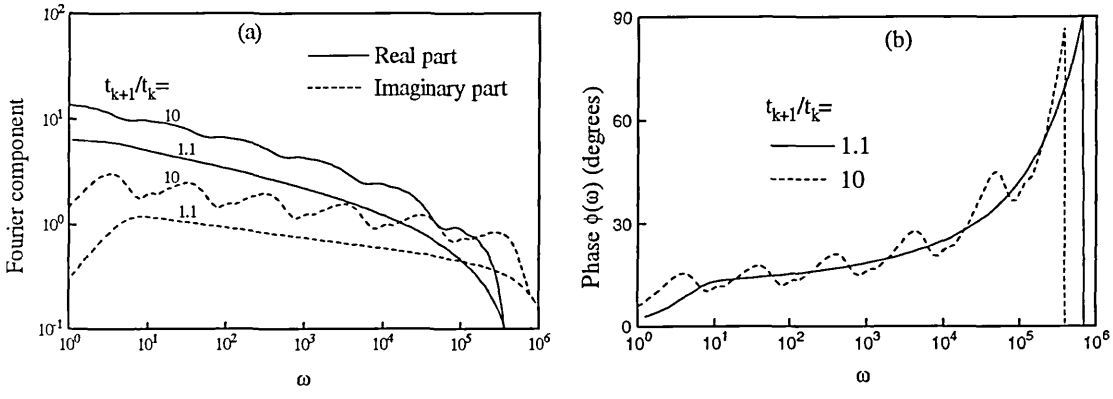

Figure 4.9 Effect of using a sampling interval of t_{k+1}/t_k=10 on (a) the real and imaginary part and (b) the phase spectra of the calculated Fourier transform for a $t^{-0.9}$ power law decay.

4.4 Use of the Fourier transform method with simulation data

The exact complex photocurrent spectrum for a given DOS can easily be calculated using the Oheda analysis of §(3.2). Figure 4.10(a) shows a comparison between the Fourier transform phase spectrum computed from the *simulated* TPC decay of figure 2.6 using a three level DOS and the *exact* phase spectrum for the same DOS and recombination time. It can be seen there is no discernible difference between the spectra. Unsurprisingly the DOS recalculated using equation 4.1 from the Fourier transform spectrum, Figure 4.10(b), is also the same as that calculated from the exact spectrum. The levels are blurred by kT tails, caused by the delta function approximation for the function W_B, but the integrated densities and the centre positions are correct.

It is not expected to be able to recalculate using the method a tail of slope sharper than kT because of the delta function approximation. However the approximation has a

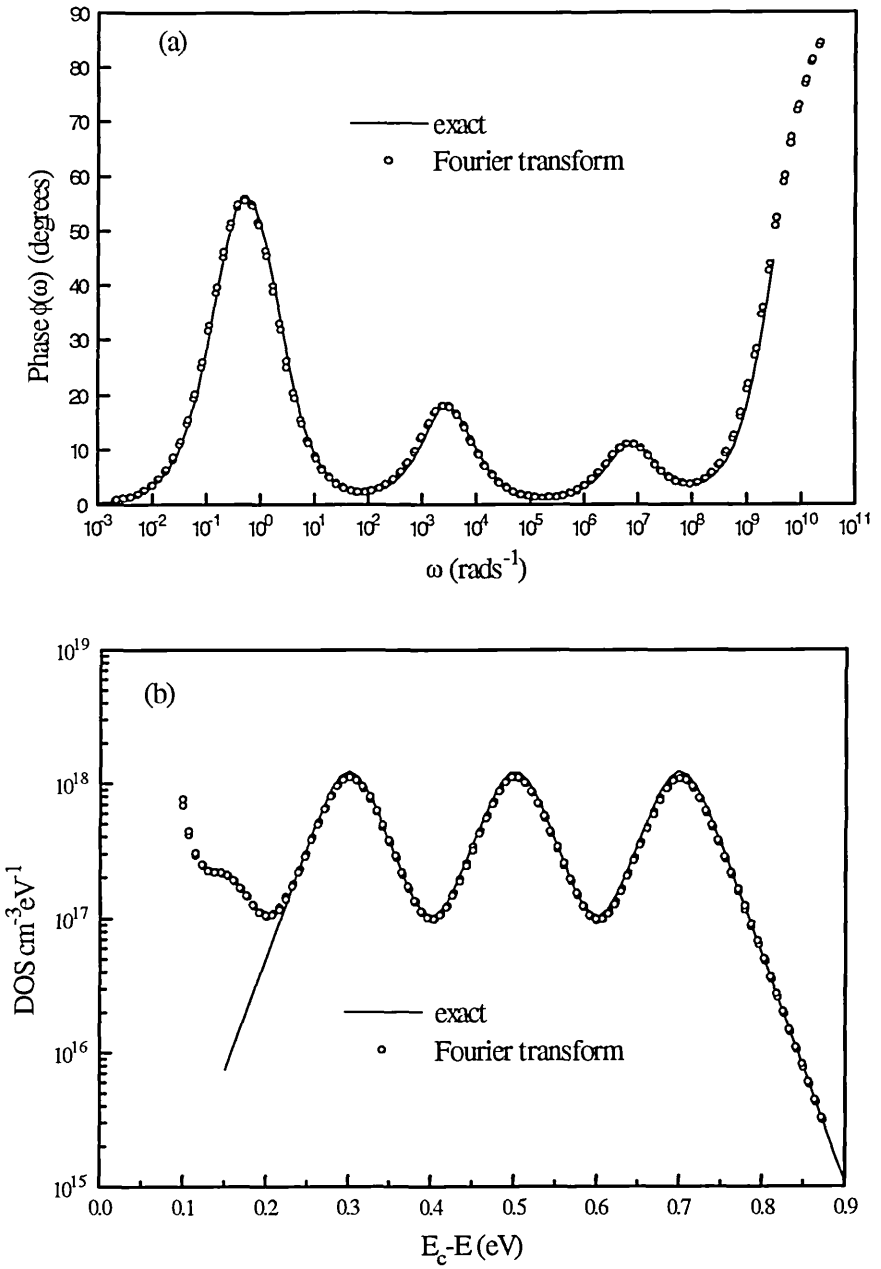

Figure 4.10 Comparison of the (a) phase spectra and (b) recomputed DOS calculated from the MPC rate equations (exact) and from the calculated Fourier transform of the simulated TPC decay (figure 2.6(b)) for a model DOS consisting of three discrete levels at 0.3, 0.5 and 0.7 eV below E_c.

further effect when dealing with tails of steeper slope than kT; the recalculated DOS is too high, figure 4.11. This is a result of the convolution of W_B with g(E), which is dominated by the large DOS on the shallow energy side of E_c-$E_{\omega,}$, but the value of which thanks to the approximation is placed at E_c-E_ω. Figure 4.12 demonstrates that for a sufficiently sharply falling exponential tail the shift to the product gW_B is at a shallower energy than E_c-E_ω.

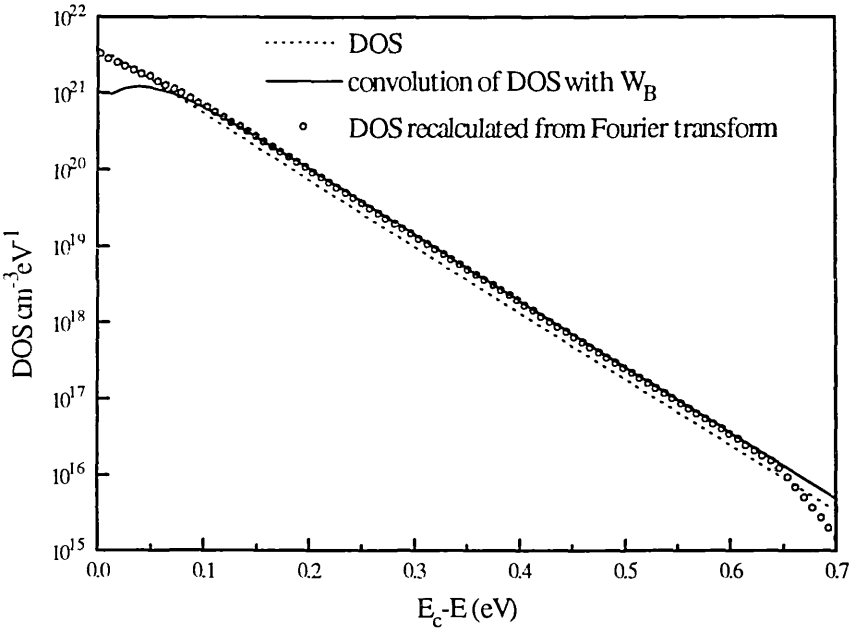

Figure 4.11 Comparison of the DOS recalculated using the Fourier transform technique from a simulated TPC decay in an exponential tail with the convolution of the model DOS with the W_B function.

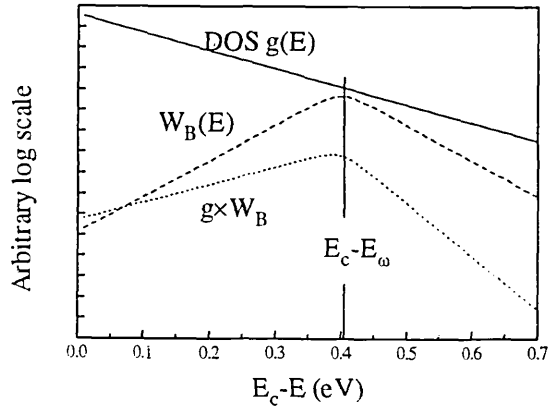

Figure 4.12 Shift to shallower energy of the peak of gW_B for a sufficiently sharply declining DOS (≤kT).

4.5 Conclusions concerning the use of the Fourier transform method

In this chapter a Fourier transform method for calculating the DOS from TPC data has been presented. It has been demonstrated that an accurate numerical calculation of the Fourier transform can be made despite the difficult nature of a typical TPC data

set, i.e.; a decay covering many orders of time and magnitude. However it is clear that the method must be used intelligently with an awareness of the circumstances that can distort the computation of the transform, in particular the possibility that significant contributions to the summation are missing because of experimental bandwidth limitations. Finally it must be borne in mind that the Fourier analysis is only valid in the régime of linear response of the material.

5.1 Sample details and characterisation

5.1.1 Coplanar gap cells

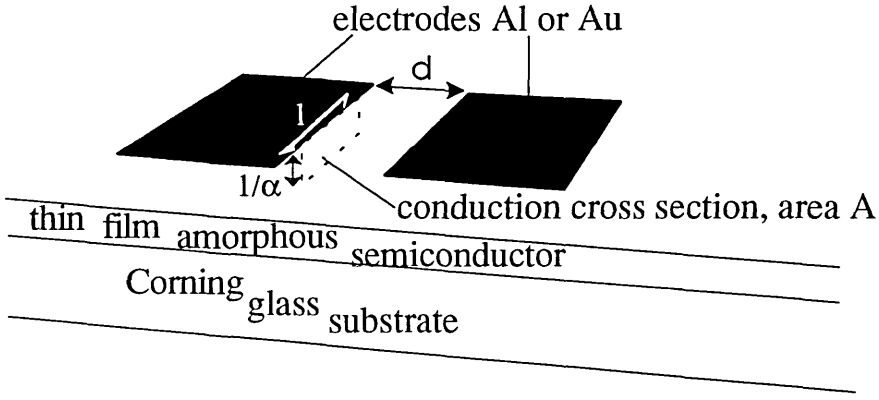

Figure 5.1 Coplanar gap cell

All the experimental investigations described in this work were performed using a coplanar gap cell as illustrated in figure 5.1. The current through the cell is approximately related to the carrier densities by

$$I = (\mu_n n + \mu_p p) e \varepsilon A \qquad (5.1)$$

where ε is the applied field and A the conduction cross sectional area. In this work it has been assumed that electrons dominate conduction in the a-Si:H and holes in the a-As_2Se_3, samples, so that in each case the minority carrier term in the brackets above may be ignored. The contacts are fabricated to be Ohmic, i.e.; their effect in the circuit can be represented by a negligibly small series resistance. The Ohmic nature of the contacts to the samples studied in this work was checked by making I-V measurements.

The approximation implicit in 5.1 is that conduction can be represented as occurring through a volume of constant carrier density with cross-section A. The depth of the cross-section is taken to be the inverse of α, the material absorption constant for the radiation, i.e.; the depth over which the intensity of radiation in the material drops to 1/e of its incident (non-reflected) value. The illumination wavelength (§5.2.4) used in this work was chosen so that the value of $1/\alpha$ of 1 μm, the same for both amorphous silicon and amorphous arsenic selenide, is commensurate with the thicknesses of the thin films. The density of excess carriers is thereby made approximately uniform throughout the depth of the sample so that the current is controlled by bulk rather than surface states. If it is desired to emphasise the effect of surface states a more strongly absorbed wavelength is chosen. The width of the cross-section is the width of the electrodes for measurement of dark currents or of photocurrents for illuminations covering the whole

Table 5.1 Sample details

Material	a-Si:H (undoped)	a-Si:H (undoped)	$a\text{-}As_2Se_3$
Fabricated at	IPE Stuttgart Germany	Dept Engineering, Univ. Cambridge	KU Leuven, Belgium
Method	PECVD	PECVD	thermal evaporation
Identification code	L011132	SCD138	—
[1] Film thickness	1.10μm	0.79μm	~1μm
Electrode gap d	0.05cm	0.044cm	0.04cm
Electrode length l	1.0cm	0.4cm	0.5cm
Electrode material	aluminium	aluminium	gold
σ_d(294k)	$4\times10^{-12}(\Omega cm)^{-1}$	$7\times10^{-12}(\Omega cm)^{-1}$	$2\times10^{-11}(\Omega cm)^{-1}$
[2] E_c-E_σ	0.80eV	0.71eV	0.83eV
[3] E_c-E_f	0.82eV	0.80eV	—
[4]Photoconductivity index γ	0.83	0.96	0.52
[1]Tauc gap	1.80eV	1.80eV	—
[5] Urbach energy	0.052eV	0.058eV	0.054eV
[6]Ambipolar diffusion length	165nm	92nm	<50nm
[7]Quantum efficiency η	1	1	0.3
$\therefore \delta G$ (laser max.)	$1\times10^{18}cm^{-3}$	$1\times10^{18}cm^{-3}$	$3\times10^{17}cm^{-3}$

Notes:

1. Transmission measurements made at IPE Universität Stuttgart
2. See figure 5.2(a) of σ_d vs. 1/T for all samples.
3. E_f calculated using a value of $\sigma_0=200(\Omega cm)^{-1}$ for a-Si:H (Stuke, 1987)
4. See figure 5.2(b) of photoconductivity vs. G for all samples.
5. Photothermal deflection spectroscopy (PDS) measurement made at IPE Universität Stuttgart
6. Grating method measurement (for a review see Weiser and Ritter, 1988)
7. Values from literature, a-Si:H (Carasco and Spear, 1983), $a\text{-}As_2Se_3$ (Mott and Davis, 1979).

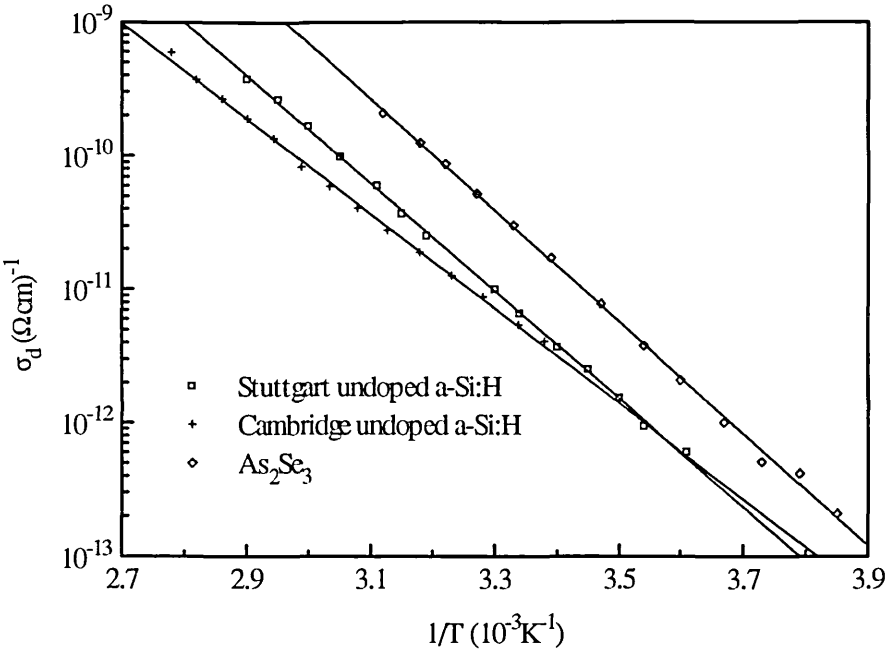

Figure 5.2(a) Dark conductivity measurements versus inverse temperature.

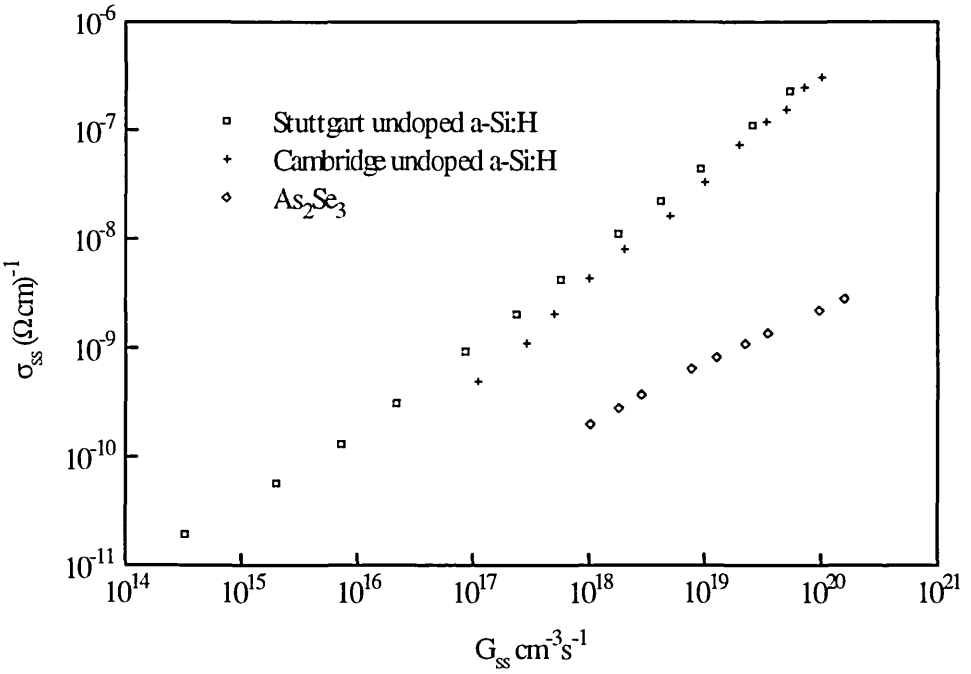

Figure 5.2(b) Photoconductivity versus generation rate measurements, T=294K.

of the cell. For illumination covering part of the cell the full width half maximum (FWHM) of the illumination intensity profile is used, see §5.2.4 below. Thus the conduction cross sections for dark current, steady state photocurrent and TPC may be different, which means that care must be taken when making calculations.

Using the approximations above and in §5.2.4 for the incident photon areal density $F\Delta t$ the density of electron hole pairs generated by an unattenuated laser pulse is

$$\delta G = (1 - R - T)\alpha\eta F\Delta t \qquad (5.2)$$

where $R \approx 0.25$, T are the reflection and transmission coefficients and η is the quantum efficiency. The thickness of all the films used in this work is approximately 1 μm, so $T \approx 1/e$.

5.1.2 Sample details

The details of the samples are presented in table 5.1, dark conductivity activation energy data in figure 5.2(a) and photoconductivity versus generation rate data in figure 5.2(b). All TPC and MPC measurements were made using a field voltage of 300V.

5.2 Transient photocurrent measurements

5.2.1 TPC system overview

Figure 5.3 is a diagram of the partially automated system used to measure TPC. A nitrogen pumped dye laser, powered by batteries and enclosed in a Faraday cage to minimise interference, is used to generate the pulse of photocarriers. The apparatus is controlled by a personal computer via an IEEE-488 connection to the digital storage oscilloscope (DSO) and an RS232 line to a pulse generator which fires the laser via a fibre optic link, again to minimise interference. The sample is sited in a liquid nitrogen coolable cryostat with windows allowing illumination by the laser from the front and a LED from the rear.

The sample signal is pre-amplified with a current to voltage amplifier. The DSO is triggered to capture the signal by means of a beam splitter which diverts part of the laser emission into another fibre optic cable. The data are passed to the computer for processing and storage. The transimpedance and bandwidth of the amplifier can be varied to allow the decay to be sampled over a range of signal magnitudes and times. For a particular bandwidth the appropriate voltage sensitivity and time base on the DSO must be set manually. The computer can then be instructed to fire the laser a selected number of times and average the measured photocurrents to reduce noise. The programme can overlap measurements at different bandwidths to build up a composite

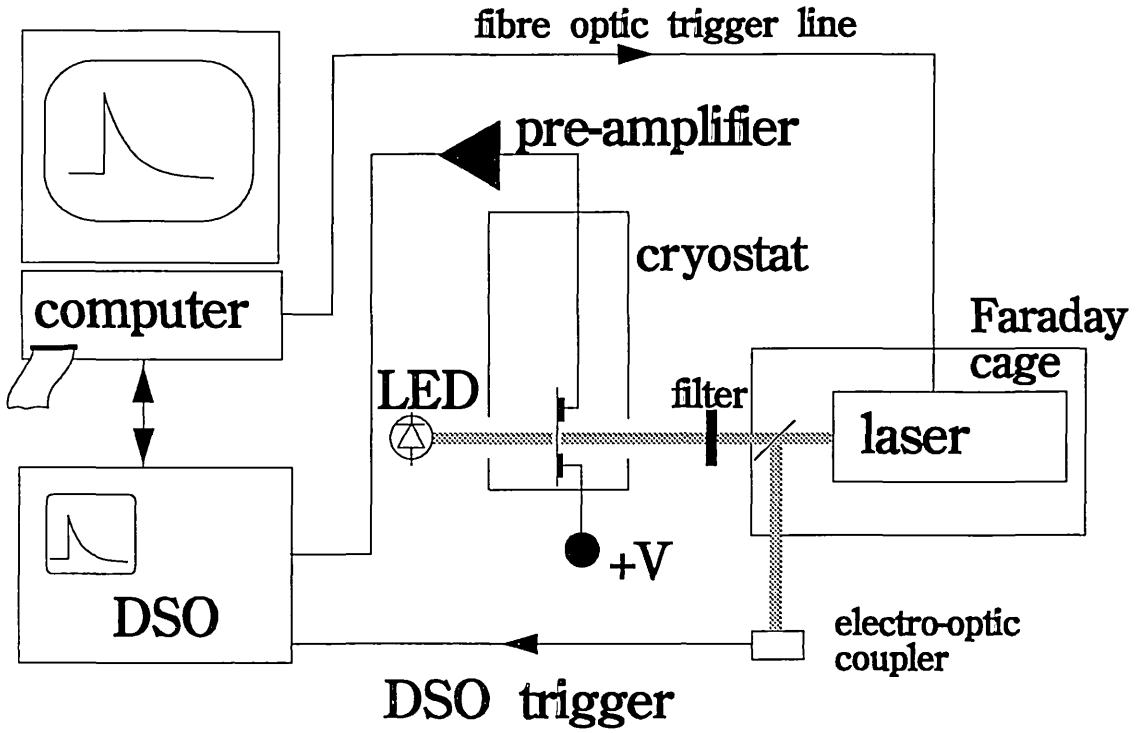

Figure 5.3 Schematic diagram of partially automated TPC measurement system.

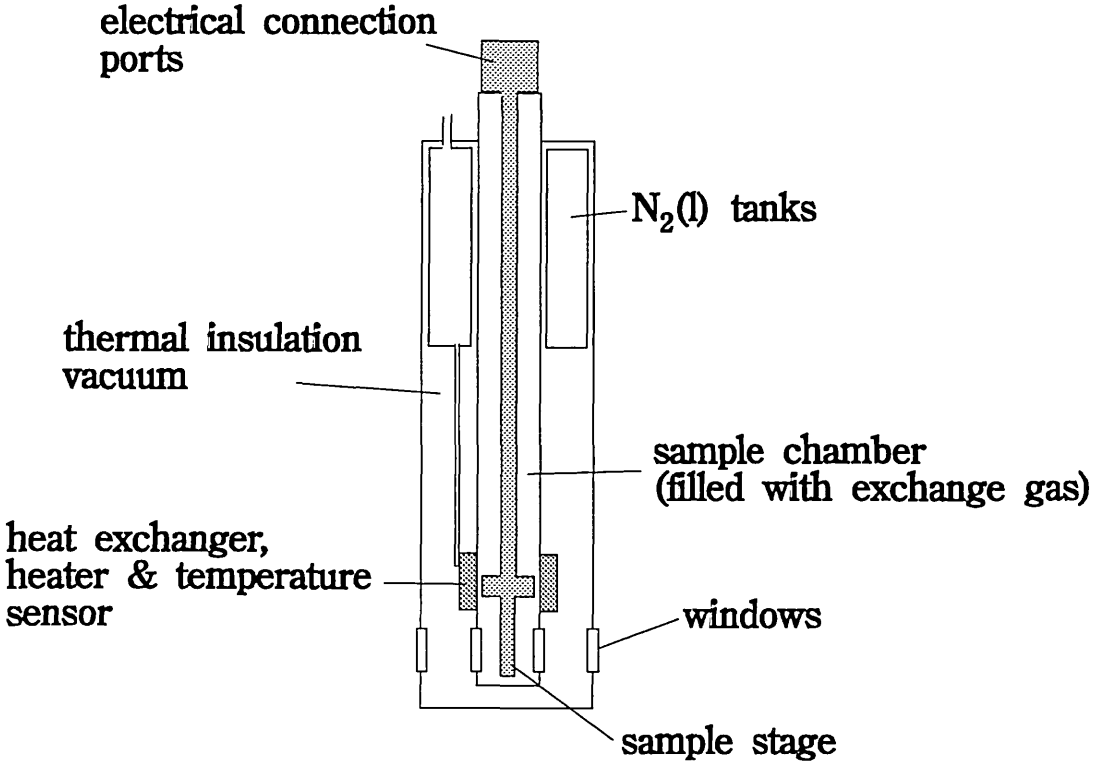

Figure 5.4 DN704 Oxford Instruments liquid nitrogen cooled cryostat.

picture of the decay. Further details of each component of the system are given and discussed below.

5.2.2 The sample chamber and cryostat

The cryostat, figure 5.4, is a model DN704 manufactured by Oxford Instruments. The sample sits on a grounded metal holder having a hole permitting illumination from the rear as well as the front, figure 5.5, in a central chamber at the bottom of the instrument. One electrode is connected to a field voltage line and the other to an earthed subminiature coaxial cable signal line. Ports for the lines are situated at the top of the cryostat. Liquid nitrogen circulated through a heat exchanger from a holding tank is used as the coolant, the rate of flow being balanced against a heater connected to a temperature controller to obtain a desired temperature. The range of temperature it has proved possible to achieve with the apparatus extends from just above the boiling point of nitrogen, 77.3K, to 360K. The sample chamber is insulated by a rotary pump vacuum but is itself at atmospheric pressure, the gas column in the chamber making the thermal contact between the heat exchanger and the specimen stage. In fact when making cold measurements the chamber was kept at a slight overpressure with a supply of dry nitrogen to avoid condensation.

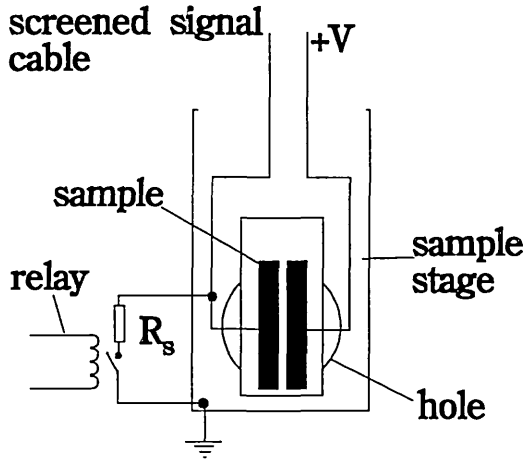

Figure 5.5 Sample stage

5.2.3 The Pre-amplifier

The photocurrent through the sample is detected by passing it through a sampling resistor R_s to earth and measuring the potential induced across the resistor with the DSO. The coaxial connectors in the circuit have an associated capacitance to earth C_c which if no other circuit elements are included restricts the bandwidth to $1/R_sC_c$. One way around the problem is to use a buffer voltage amplifier. Only the capacitance appearing at the input to the amplifier then affects the bandwidth. The buffer should therefore be situated close to the sample. However the lack of space in the sample chamber and the extremes of temperature to which the components would be subjected preclude this solution. The pre-amplifier is instead situated outside the cryostat close to the signal port. There is therefore a large input capacitance to the amplifier, the coaxial signal cable being about 35cm long having an overall capacitance to ground of about 30 pF. Since the input capacitance cannot be reduced the alternative is to reduce the input impedance by using a current-to-voltage amplifier configuration, figure 5.6. The circuit acts so that the output voltage V_{out} is given by $V_{out}=-I_{in}R_f$, where I_{in} is the current through the sample. Thus R_f is the effective sampling resistance. However R_f does *not* determine the bandwidth of the signal line - this is instead determined by the input impedance of the operational amplifier which is very small. The limiting bandwidth of the circuit is actually $1/R_fC_f$. Note that although C_f has been drawn in as a separate component it is an unavoidably present "stray" capacitance associated with the R_f and the circuit layout.

The current amplifier has the drawback that for smaller R_f it is unstable because the operational amplifier introduces phase shifts to the high frequency components of the signal, resulting in positive feedback and oscillation. Stabilisation can be effected by

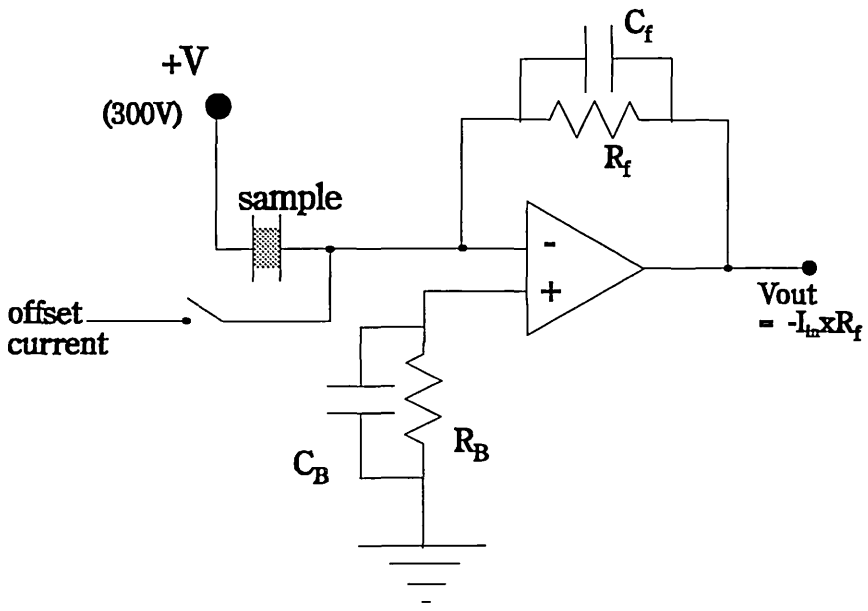

Figure 5.6 Current-to-voltage pre-amplifier. The output voltage $V_{out}=-I_{in}R_f$, where I_{in} is the current through the sample.

deliberately reducing the bandwidth to filter out the high frequencies by increasing C_f. Physically a feedback resistor is mounted on a holder which is plugged into a socket on the circuitboard. Resistors at decade intervals in the range 10kΩ-10^{11}Ω were used in the course of the investigation. The 10kΩ-10^6Ω resistors have in series a capacitor consisting of a length of miniature coaxial cable, trimmed so that the capacitance is just large enough to prevent oscillation. No series capacitor was found to be necessary for the higher resistances, and stabilisation was not found to be possible for a 1kΩ resistor. Note that the great current sensitivity afforded by the capability of using very large R_f is an advantage of the current amplifier configuration over a voltage buffer amplifier. The bandwidth for each R_f was determined by measuring the rise time, the time to rise to $(1-1/e)\times 100\%$ of the final output voltage for a small square pulse input current, 5.7(a). The results are presented in figure 5.7(b). The screened resistor network in figure 5.7(c) was used to generate the current pulse from a voltage pulse. The network avoids problems with capacitative coupling which would arise if a very large series resistor was used to create the same magnitude of current pulse.

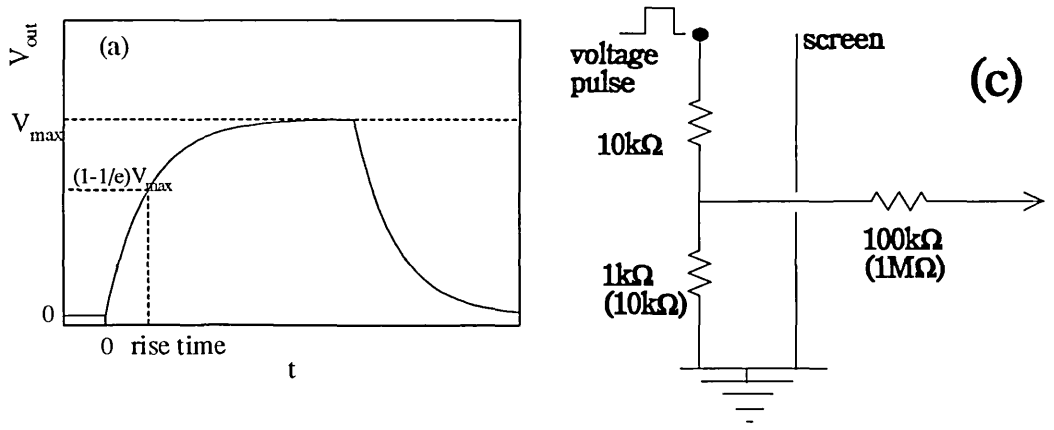

Figure 5.7 (a) Response of an RC network to a square voltage pulse illustrating the definition of the rise time, (c) screened resistor network used to create a *current* pulse to calibrate the rise times of the pre-amplifier.

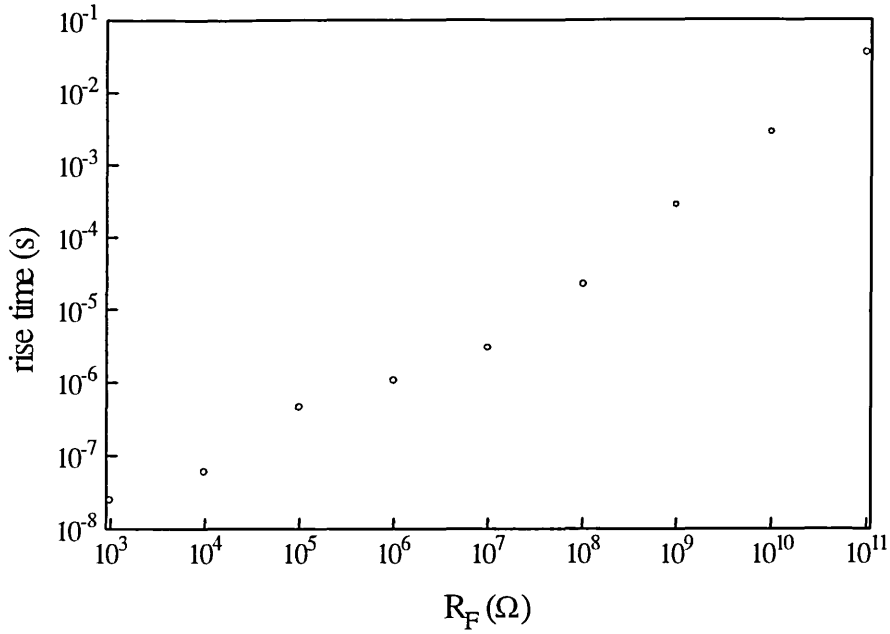

Figure 5.7(b) Measured rise times of the pre-amplifier for a small current pulse versus feedback resistance R_f (Dick, 1994).

An effect which limits the ability of the circuit to follow the signal is found to operate for steep power law decays. Figure 5.8 shows the numerically calculated response V_0 of an RC circuit to an input voltage signal V_I in the form of a t^{-1} power law decay. V_0 *overshoots* V_I and does not follow the input signal until t=10CR. Thus when dealing with steep power law decays the time after which the output of the pre-amplifier is following the input can be ten times longer than the rise times of figure 5.7(b). Care was taken during this work to identify such situations.

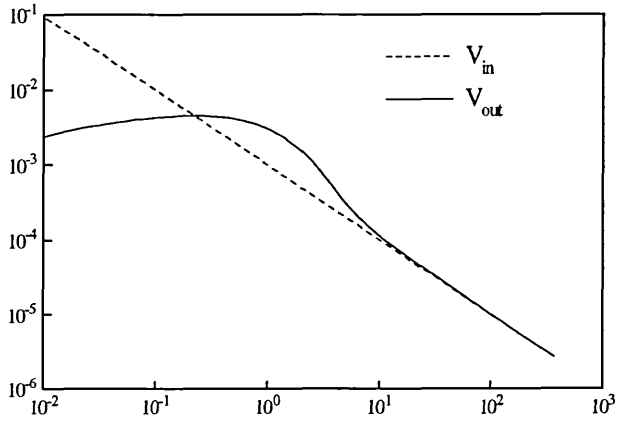

Figure 5.8 Response of a CR network to a t^{-1} power law decay. V_{out} does not follow V_{in} until ten times the rise time.

For sufficiently large magnitude very short time signals (≈ns) a 47Ω sampling resistor sited on and earthed to the sample holder may be used to detect the current instead of the current amplifier. On this time scale the RC model of the connector bandwidth does not apply. The value of 47Ω was chosen to match the characteristic impedance of the coaxial connector cables since impedance mismatches cause the signal to be reflected, distorting the data captured by the DSO. Similarly the coaxial cable leading to the DSO input must be terminated with 47Ω. The 47Ω sampling resistor is

switched in and out of circuit by means of a relay, figure 5.9, connected to earth. The relay has proved capable of withstanding liquid nitrogen temperatures.

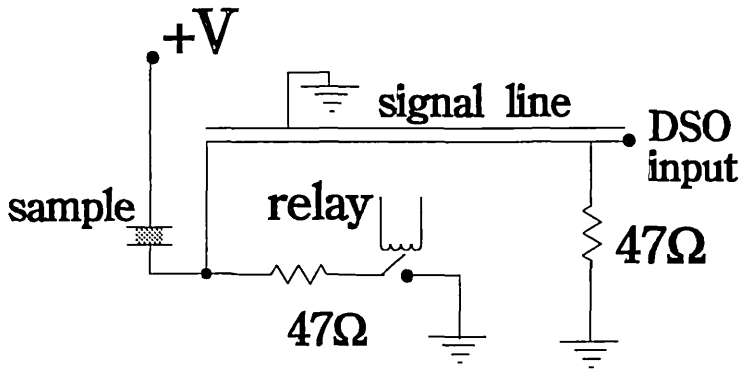

Figure 5.9 Detection of short time TPC by a 47Ω resistor sited on the sample stage and switched to earth by means of a relay.

An arrangement to supply a dc current to the input of the op-amp is included in figure 5.6. This is required to offset the steady state photocurrent through the sample when optical bias is applied which would otherwise cause the op-amp to saturate. However, if the offset is used the observation of TPC at long times is limited by 1/f noise and drift in the offset current. The op-amp chip is a Burr-Brown OPA637 using DIFETs, chosen for its wide bandwidth, low input current noise ($1.6fAHz^{-1/2}$ at 1kHz) and low input bias current. The low input current noise and bias current are especially necessary to allow the use of large R_f.

5.2.4 Light sources

The dye used with the laser was Rhodamin 101, which gives an emission peak at 655nm (1.90eV). This is in the red, but photons being neutral particles no charge is incurred. The intensity of the beam can be attenuated by the use of neutral density filters placed in the light path. A $0.8mm^2$ area fast pin photodiode (Hewlett-Packard 5082-4207), calibrated for current vs. incident photon flux per square centimetre against a thermopile (Merazga, 1990) was used in the circuit of figure 5.10 to characterise the laser pulse. An optical density 4 ($OD4=10^{-4}\times$) attenuator was used to reduce the current in the photodiode to its linear response region below about 100mA. The temporal intensity profile, observed with a Tektronix model 7623A analogue storage oscilloscope, is Gaussian in shape, with a FWHM of around 5ns. Figure 5.11 shows the spatial intensity distribution in the plane of the sample (i.e.; at the same distance from the laser), along axes parallel and transverse to the electrodes, also Gaussian in shape with FWHM 2.3 and 1.3 mm respectively. For this work the spatial distribution is approximated by a square profile of parallel axis width 2.3mm and magnitude $F=4.1\times10^{22}$ photons $cm^{-2}s^{-1}$, which has the same integrated intensity as the measured parallel distribution. The variation in the transverse direction was ignored because the FWHM is over twice the largest sample electrode spacing. A similar temporal approximation is made that the pulse is square and of duration $\Delta t=5ns$. The

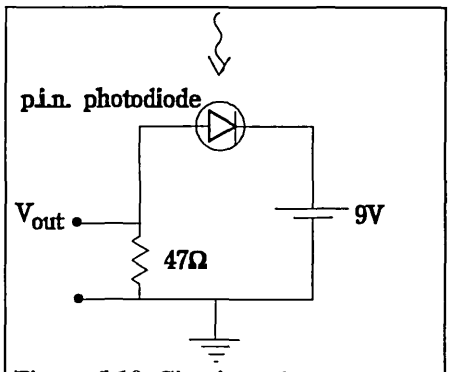

Figure 5.10 Circuit used to characterise the laser pulse.

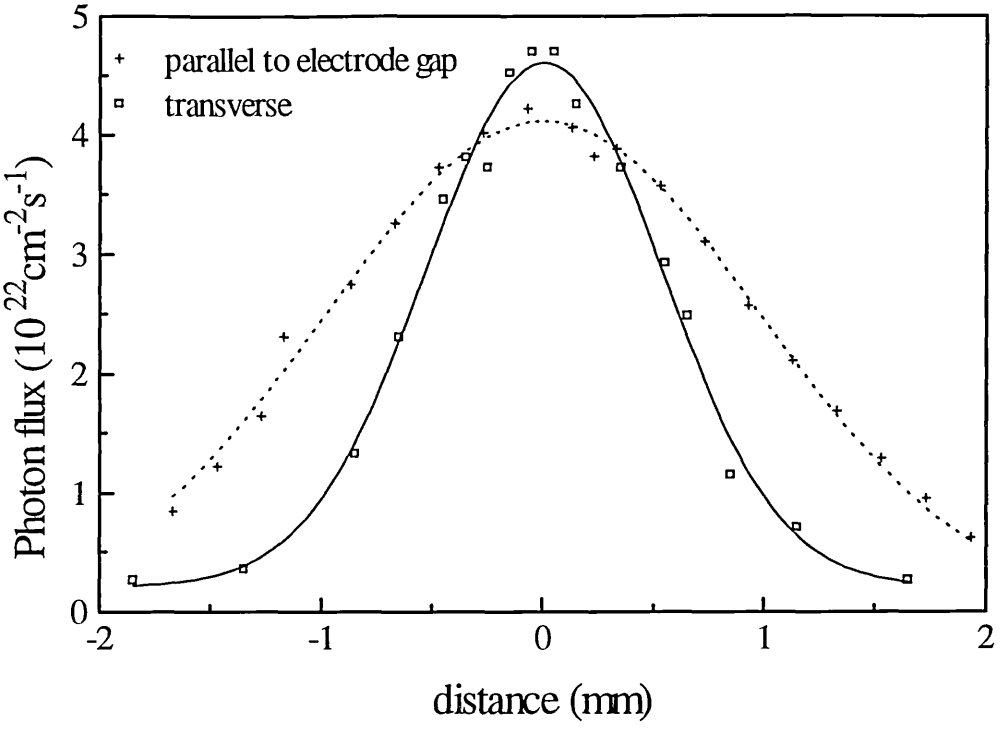

Figure 5.10 Spatial distribution of laser spot intensity at the position of the sample.

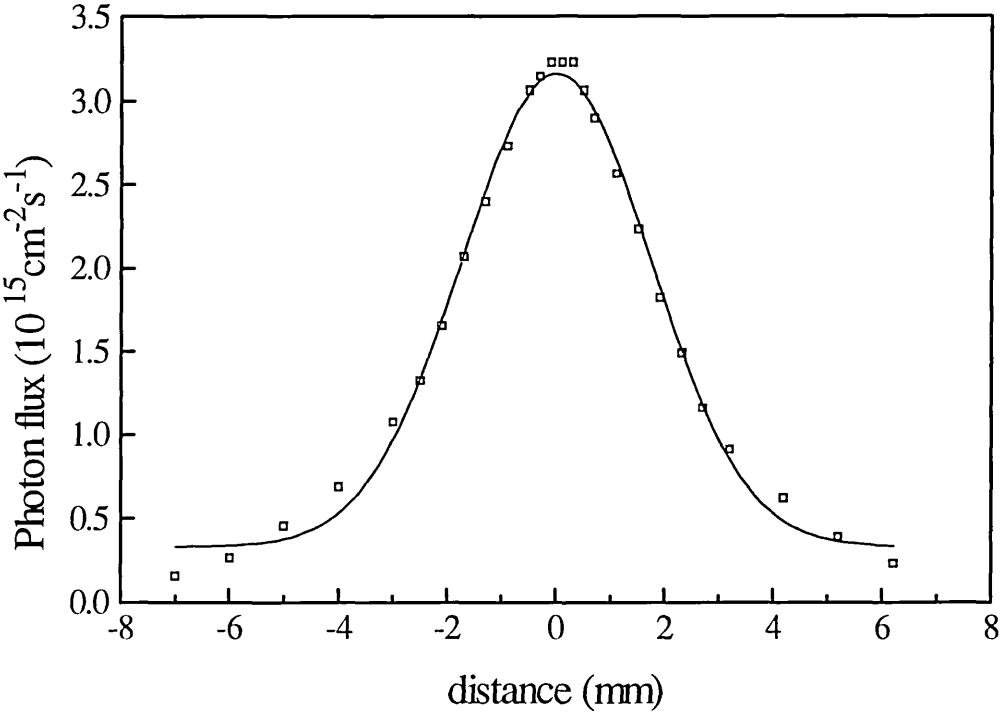

Figure 5.11 Spatial distribution of LED/light pipe spot intensity at the position of the sample. The distribution is circularly symmetric.

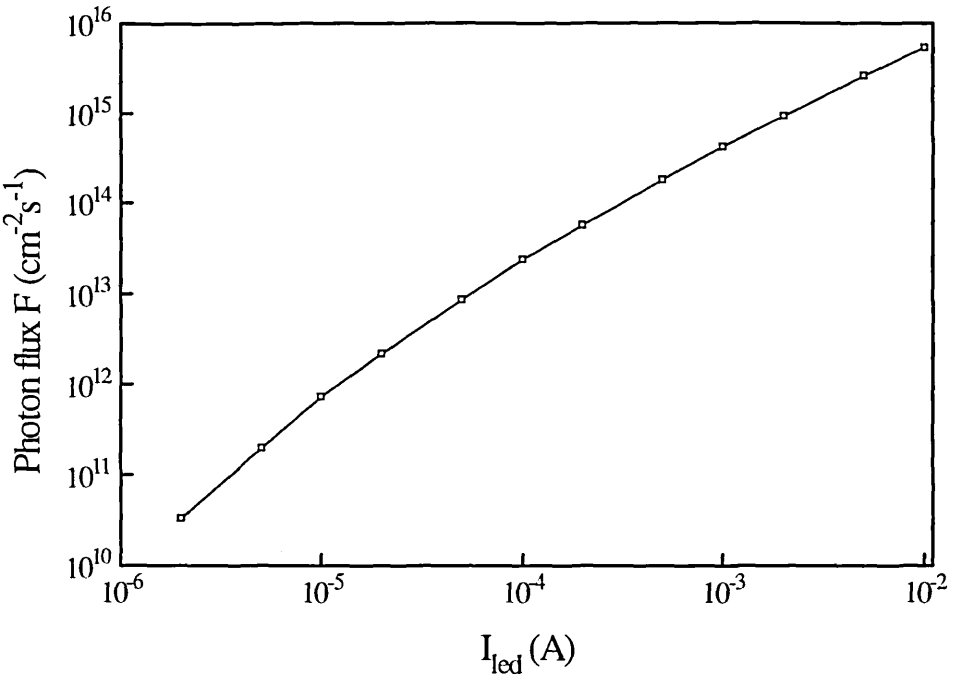

Figure 5.13 Peak photon flux emitted by LED/light pipe at the position of the sample versus LED driver current.

areal density of photons incident on the surface of the sample from a single unattenuated laser pulse is thus $F\Delta t=2.1\times10^{14}$ photons cm^{-2}.

The Stanley H3000 LED, emission peak 654nm, used for optical bias was characterised similarly. The LED output is directed onto the sample through a quartz light pipe so the measurements in figure 5.12 were made at the appropriate distance from the end of the pipe. The intensity distribution is circularly symmetric with a FWHM diameter of 4.3mm. Figure 5.13 plots the *peak* photon flux against the LED current. The peak values must be multiplied by a correction factor of 0.79, arrived at by a similar procedure to that for the laser, to give the mean flux across the FWHM diameter. The LED can also be used as a source of pulse excitation by passing currents of up to 10A for 200ns, delivering a maximum total density of 4×10^{11} photons cm^{-2}. The LED is not damaged because of the short duration of the high current.

5.2.5 Signal capture and processing

The digital storage oscilloscope is a Gould model 4072, which has two input channels, 100MHz bandwidth, is capable of 400 Mega-samples s^{-1} on each channel decreasing to 5 samples s^{-1} on the longest time range, analogue to digital conversion to 8 bit precision and storage of 1008 samples on each channel per scan. In use the DSO voltage sensitivity and timebase are set manually and the controller computer programme instructed to fire the laser a specified number of times. During this process the manual controls of the oscilloscope are disabled. Each time the laser is fired the DSO captures both the specimen signal and the signal from an electro-optic coupler connected to the fibre optic cable sampling the laser pulse directly, the coupler signal being used as the trigger. Both channels of captured data are then passed as a stream of 8 bit numbers, representing the fraction of full scale deflection measured at each capture event, to the computer which updates the average of the measurements in floating point arithmetic. Weighting is handled so that at the end of the process each measurement has been given the same relative weighting (multi-channel averaging).

When the user requires no more laser firings the programme is instructed to calculate the current and sample time represented by each point of the averaged signal, interrogating the DSO directly to obtain the voltage sensitivity and time base, and extracts the transient part of the recorded signal by subtracting the steady state part. Each data set passed by the DSO includes the 200 samples recorded just before the trigger was received. The first 150 of these points are used to calculate the steady state baseline. The peak in the recorded signal from the channel monitoring the laser directly and an offset are used to identify the position of the beginning of the photodecay so that data points corresponding to shorter times can be deleted. The programme interrogates the user once during a set of measurements to obtain the time offset between the peak in the direct laser signal and the start of the transient photodecay. The offset exists because of the different system time delays experienced by the sample and laser signals, and is of the order of 10ns. Finally further averaging of the data is carried out using the technique of variable bandwidth digital filtering, which consists of replacing the data points in a time window $t-\Delta t$ to $t+\Delta t$, $\Delta t \propto t$, by a single data point at t with a current which is the average of the replaced data. The smaller currents at longer times thus undergo more averaging, whilst a data point time interval ratio of approximately 1.1 (chosen to suit the Fourier transform procedure, see §4.3) is maintained. This reduces the 808 sampled points to 62 for plotting.

Typically the transient response of an amorphous silicon specimen can be temporally resolved from 5ns to 100s using four time range settings, averaging 100 pulses for each setting. The averaging procedures permit the signal to be recovered from noise 1-2 orders larger in magnitude, to an effective precision *better* than 1 bit. When using multiple pulses care must be taken that the specimen is allowed to relax sufficiently in between each measurement, so the programme is written to allow a pause of user specified length in between each laser firing. The programme execution time with the computer used results in a minimum pause of 0.2s. On the longer timebases a pause of at least 10× the longest sample time was used. Care has also to be taken that the pre-amplifier or DSO front end internal amplifier are not overloaded. The nature of the TPC signal presents some problems in this regard, the current being very high at short times but small at long times. If a large gain is used to observe the long time signal the risk is run of the short time signal overloading the electronics, to the extent that in some circumstances even if the overload time is shorter than the sampling interval the recovery time can be much longer. Confidence in the measurements is assured by overlapping different timebase data sets. Since the circuit parameters for each set are different it is unlikely that instrumental distortions will affect each set in the same way.

5.3 Modulated photocurrent measurements

5.3.1 MPC system overview

Figure 5.14 is a block diagram of the MPC measurement system, also partially computer controlled by IEEE-488 links. The excitation light is provided by a LED with a programmable signal generator (Thurlby-Thandar TG1304) acting as the current source. The sample photocurrent is detected with a current to voltage amplifier as before and the complex signal phase and magnitude are measured by a phase sensitive detector (PSD) The PSD is provided by the signal generator with a reference signal synchronised with (although not necessarily in phase with) the LED supply current.

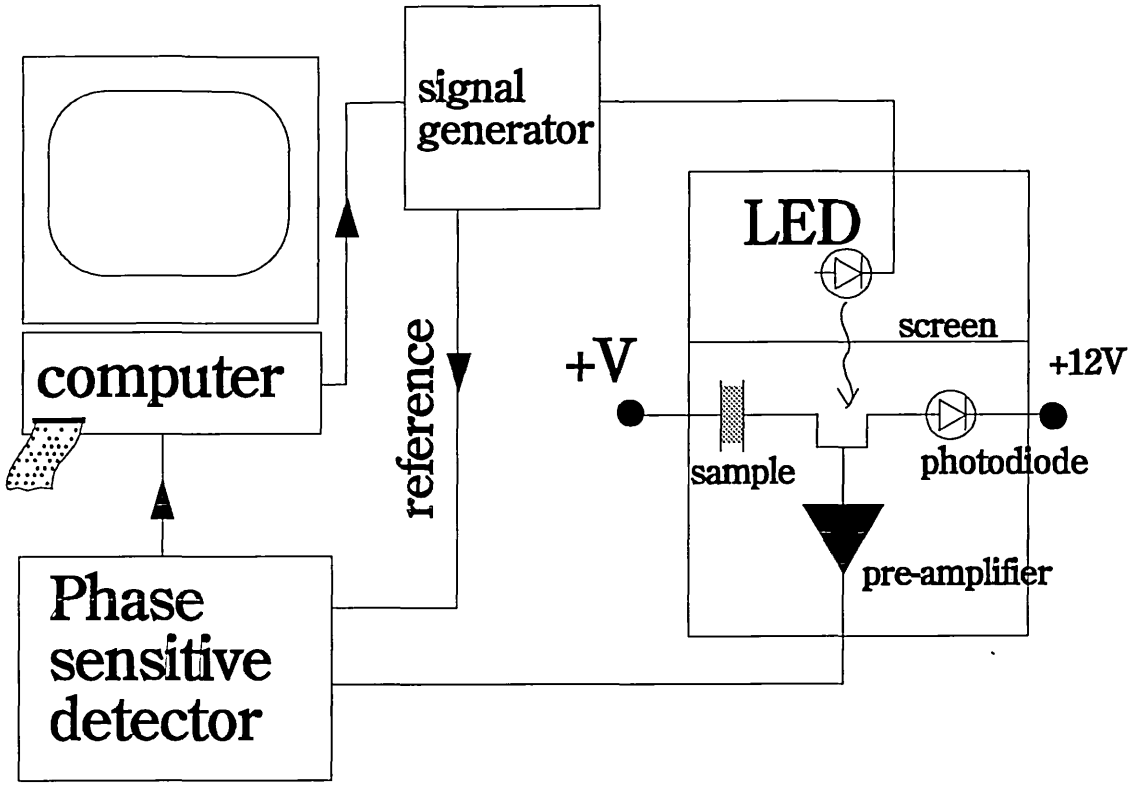

Figure 5.14 Experimental system for measuring MPC.

The experimental procedure is to set the mean flux and modulation index using the manual controls on the signal generator and an appropriate series resistance. A computer programme is run which sweeps the modulation frequency in logarithmic steps between 2 Hz and 10^5 Hz. At each frequency the user can adjust the PSD sensitivity and allow the reading to settle. The computer is then instructed to read the PSD measurement several times, usually five, and record the average. The final step in obtaining the MPC spectrum is to subtract from the recorded phase the phase shift due to the measurement system which has previously been measured with the aid of a fast photodiode using the same procedure, see §5.3.2 below.

5.3.2 Phase sensitive detection

The PSD is a Stanford Research Systems model SR530, capable of measurements in the range 2 Hz-10^5 Hz. The basic principle of the instrument is illustrated in figure 5.15(a). The demodulator multiplies the input signal V_{in} by an alternating polarity square wave of the same frequency as the reference signal. Thus if the input is a sine wave of the same frequency as and in phase with the reference signal it will be full wave rectified, figure 5.15(b). The demodulator signal is smoothed by a low pass filter to produce the final dc output V_{out} which is the in-phase part of the selected frequency component of V_{in}. The quadrature signal is obtained by shifting the square wave by $\pi/2$, which in the case of the sine wave would result in V_{out} zero. The bandwidth around the reference frequency which contributes to the output is inversely proportional to the time constant τ of the low pass filter, which can be adjusted. It follows that a PSD is capable of an arbitrarily high signal-to-noise ratio which in practice is set by the practicalities of the experimental time scale. In use a settling time of 3τ must be allowed to permit the output to reach its final value. A τ of 1-10s was generally used. The SR530 permits direct measurement of the signal magnitude and phase shift w.r.t. the reference signal.

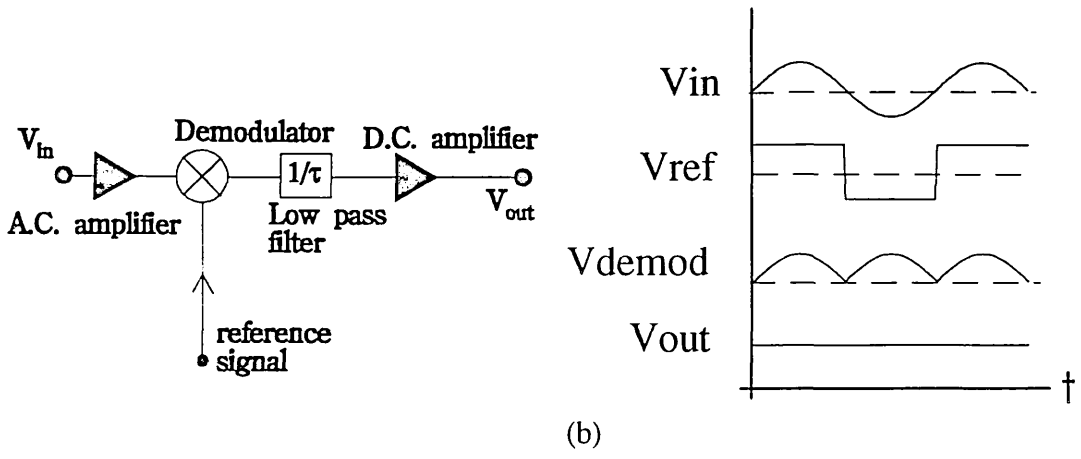

Figure 5.15 Illustration of principle of phase sensitive detection.

The relative contributions of the ac and dc amplification stages to the overall gain can be varied to suit the nature of the signal. The greatest stability in the output signal is achieved in the high stability/low dynamic reserve mode, in which the ac gain is largest, because dc amplifiers are subject to low frequency noise and drift. However if the signal is buried in a high noise background ac amplifier may be overloaded, and in such cases ac gain may be traded for dc by using the high dynamic reserve mode, at the cost of reducing the stability of the output signal.

5.3.3 Sample circuit

Using the same simple RC model as for TPC (§5.2.3) the frequency domain response of the sample-amplifier circuit begins to introduce significant extra phase shift to the signal at a frequency one order smaller than the bandwidth, figure 5.16. If the value of the extra phase shift can be determined then by phasor analysis the signal phase can be recovered by simple subtraction for frequencies low enough that the signal magnitude is not affected, i.e.; within the bandwidth.

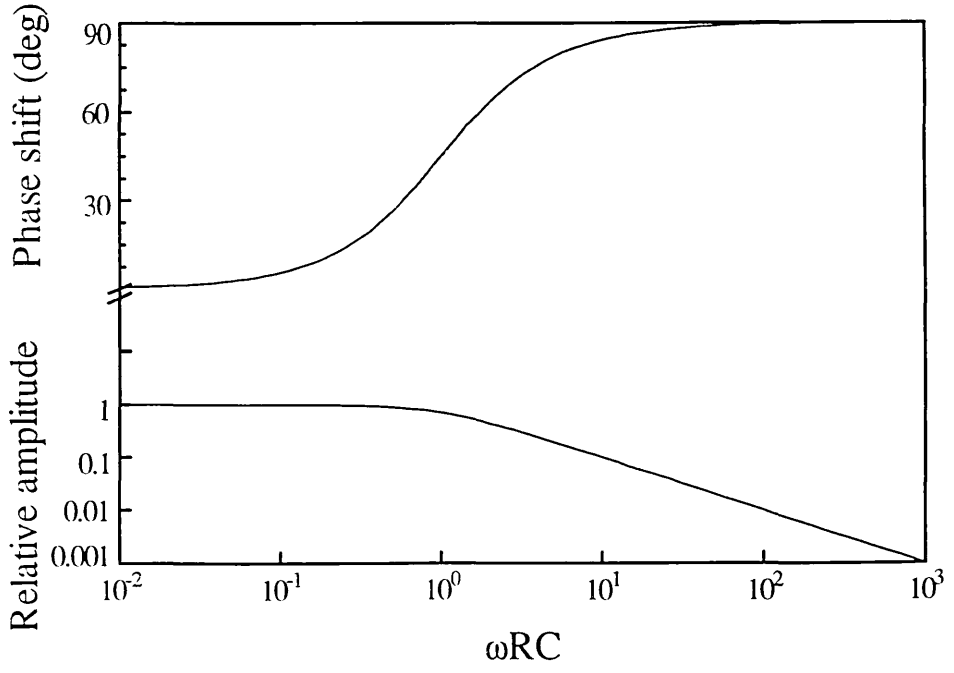

Figure 5.16 Frequency domain response of an RC network. The phase shift begins to rise at a tenth of the frequency at which the amplitude begins to fall.

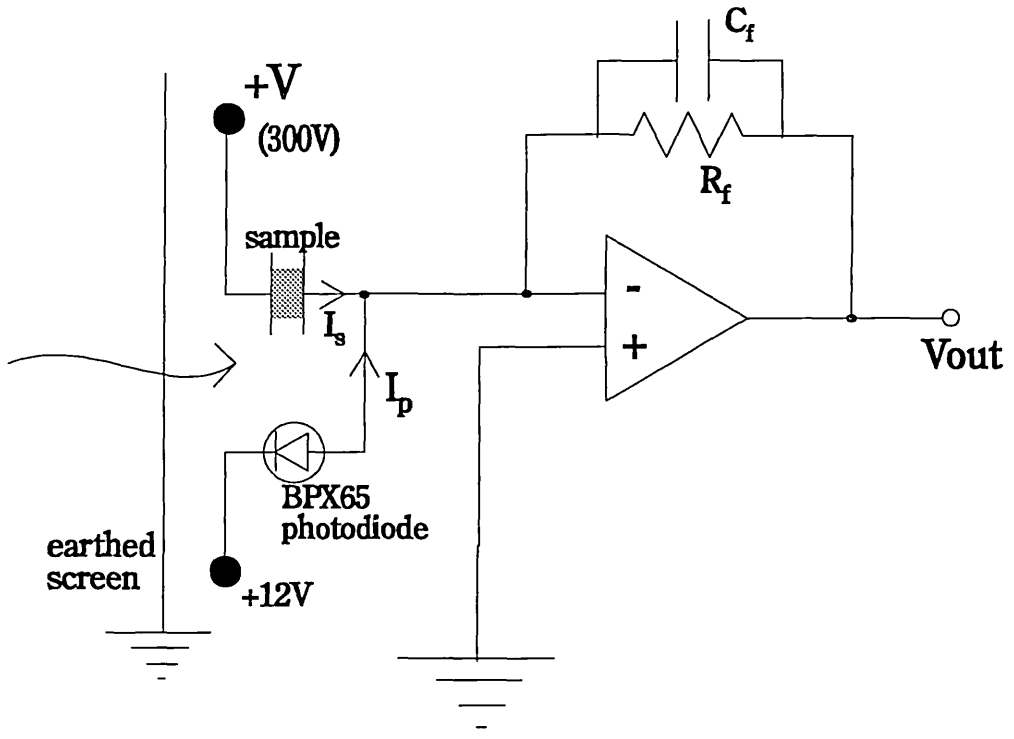

Figure 5.17 MPC sample and pre-amplifier circuit, showing the arrangement to enable the measurement system introduced phase shift to be determined.

The circuit is depicted in figure 5.17. The op-amp (Burr Brown OPA627) is used in a summing amplifier configuration for the currents through the sample and the photodiode, $V_o=-R_f(I_s+I_p)$. In use either the sample or the photodiode is blocked off with a non-metallic shutter. The central point of the design is that the input capacitance is the same when the photodiode is uncovered as when the sample response is being measured, so that the effect of the circuit on the photodiode signal should be identical to its effect on the sample signal. The photodiode signal should be in phase with the light intensity because of its fast response (§5.2.4), and so can be used to determine the instrumental phase shift. Note that this design also removes potential problems with phase shift between the reference signal sent to the PSD and the actual phase of the light intensity modulation. This phase shift can show a frequency dependence associated with the series resistor used to set the LED current and the LED plus stray capacitances. Figure 5.18 shows the photodiode calibrations for the two R_f, C_f configurations used in this work.

In previous work with a different model of PSD (Webb, 1990) it was noted that changing the PSD sensitivity setting introduced a phase shift. In that work therefore the photodiode and sample signals were analysed on the same setting by attenuating the larger photodiode signal. In the present work the same problem has not been observed so no such precaution has been taken. The most accurate method of doing so would entail attenuating the LED output falling on the photodiode.

The LED is situated about 1cm from the sample/photodiode arrangement and is rigorously electrically screened to minimise capacitative coupling. The magnitude of the coupling was checked by blocking off the sample and the photodiode simultaneously, and was found to be negligible over the whole frequency range. The sample and photodiode are arranged approximately symmetrically with respect to the LED beam so that both are equally illuminated, enabling the photodiode signal to be used to determine the incident photon flux.

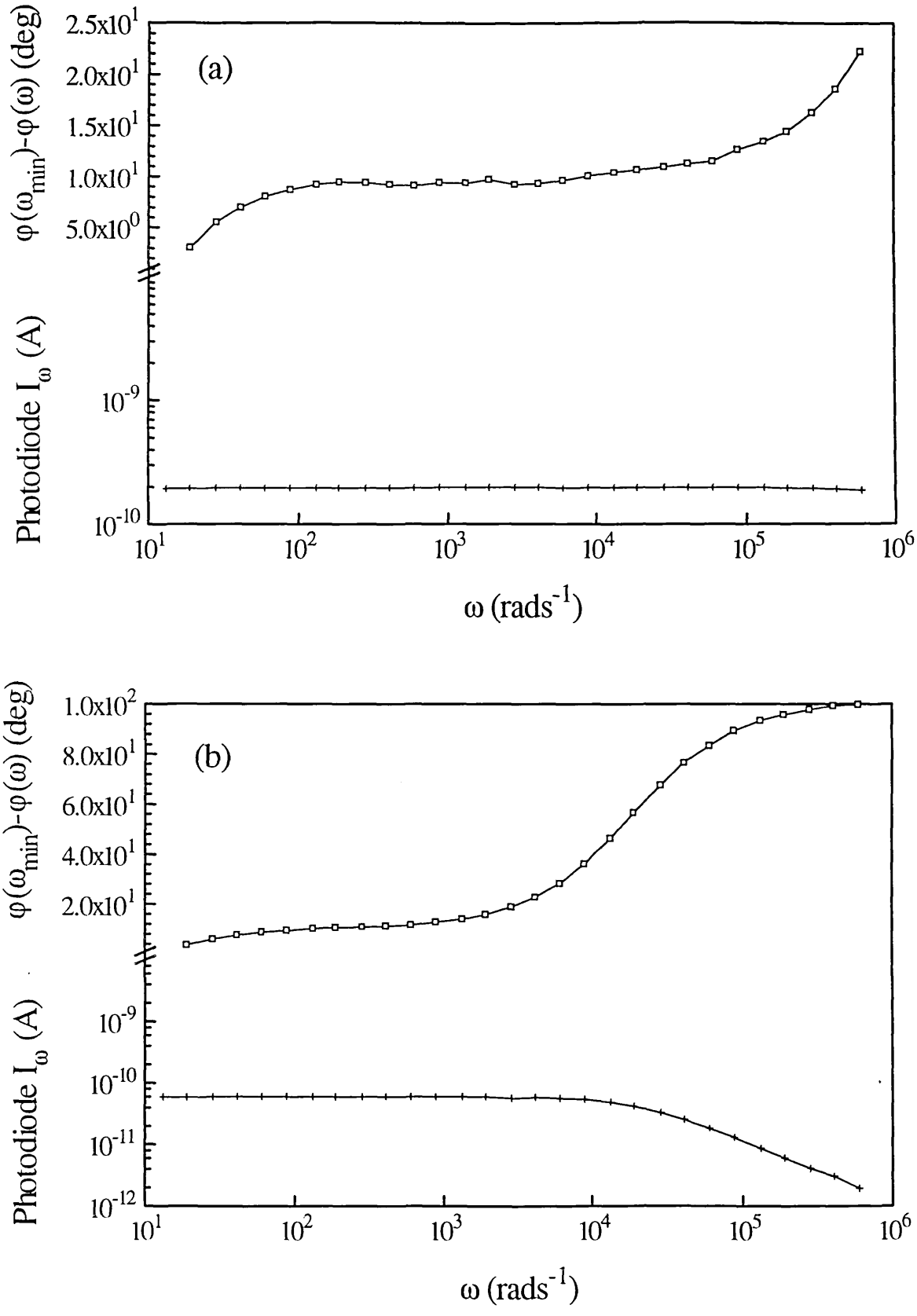

Figure 5.18 Calibration curves for the two R_fC_f configurations used in this work, (a); $R_f=10^5\Omega$, $C_f=0$, (b); $R_f=10^7\Omega$, $C_f=5pF$. The bandwidth of the (a) configuration is large enough to permit measurements at the PSD maximum input frequency of 10^5Hz to be made, the (b) configuration bandwidth limits measurements to less than 10^4 Hz.

5.3.4 Other sources of error

There are other sources of error which contribute to the signal when both sample and photodiode are blocked and which should be minimised. In addition to capacitative there is also electromagnetic coupling between the LED drive and sample circuits. The effect is expected to be small in the frequency range used, but it is such coupling which ultimately places an upper limit on the frequency at which MPC measurements may be made using the equipment described here. There is also ground loop emf, viz. small voltage differences due to Ohmic volt-drops between the instrument grounds which can appear when the experimental system is grounded at more than one point, for example via mains power leads (Keithley Instruments, 1992).

A non-instrumental potential source of error is the detection of harmonics of lower frequency processes in the sample signal. This can occur because PSD's will respond to odd harmonics of the reference signal which appear at the input. The theoretical model for MPC is a linear one and harmonics would be the result of non-linear behaviour by the sample. Experimentally the linearity of response is checked by maintaining the mean photon flux but varying the modulation index. If the response is linear the complex signal amplitude should scale with the complex flux amplitude but the phase should be invariant. This was observed to be the case with the a-Si:H spectra, see §8.1.

6.1 Linear régime

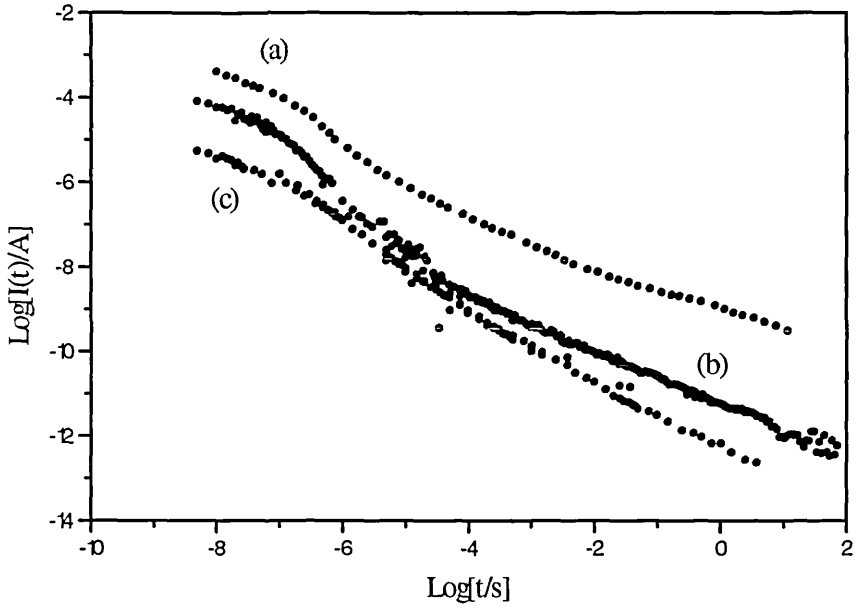

Figure 6.1: TPC decays in samples of undoped a-Si:H, (a) from literature (Antoniadis and Schiff, 1992), (b) deposited at I.P.E. Universität Stuttgart and (c) deposited at Cambridge University Engineering dept. (a) and (c) are shifted by a decade upward and downward for clarity.

Figure 6.1 shows TPC decays measured in both the Cambridge and Stuttgart a-Si:H materials at room temperature and with a laser pulse intensity cut by two orders of magnitude to give a calculated initial photocarrier density of 10^{16} cm^{-3}. A decay from the literature obtained with the same order of magnitude of excitation is included for comparison. In order to be able to use the Fourier transform technique with TPC data the material response must be sampled in the régime of linear variation of TPC with pulse intensity. The response for both a-Si:H materials at 10^{16} cm^{-3} is linear, at least up to 1ms, see figure 6.2. At longer times there is some deviation from linearity but the effect on the calculated DOS of reducing the intensity further is small, whilst there is a substantial decrease in the quality of the data because the relative magnitude of the noise is larger. It is further argued below that the early part of the TPC decay has the largest effect on the calculated DOS. Measurements of the intensity dependence of the specimen response are presented and discussed in §6.5.

The decays of figure 6.1 show a three slope structure characteristic of good quality undoped a-Si:H. There is a short time, high current, relatively non-dispersive region, followed by a steep fall between 100ns and 10μs and finally a power law decay to

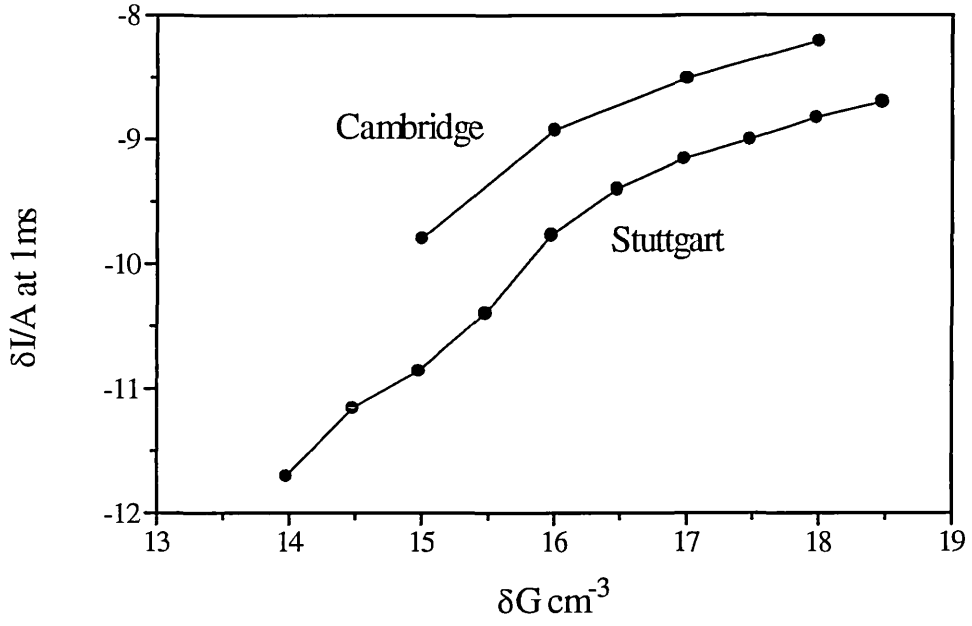

Figure 6.2 Transient photocurrent at 1ms after the photoexcitation pulse versus pulse photon density. The variation is sublinear above $\delta G=10^{16}cm^{-3}$ and linear below for both a-Si:H materials.

long times. Applying the intuitive thermalisation model this shape is suggestive of a DOS consisting of a sharp exponential at shallow energies and a broad exponential at deep energies. The short time region would correspond to conduction being controlled by multiple trapping in the shallow states, the long time power law decay to thermalisation in the broad exponential. The magnitude of the current falls when the charge transfers between the two parts of the DOS because the occupation of the broad tail is smaller than would be the occupation of a continuation of the sharp exponential. The expected magnitude of photocurrent for a broad tail is calculated in §6.4.

Application of the Fourier Transform technique produces a different picture. Figure 6.3 shows superimposed DOS profiles calculated from decays for the Stuttgart material at different temperatures, assuming $\nu=10^{12}$Hz. Differing temperatures allow access to differing ranges in energy, and overlapping the DOS profiles strengthens the case for the interpretation made by the method. There is a shallow energy steep tail, of characteristic energy 0.03 eV, but instead of the broad tail there is structure consisting of a deep bump with a peak at $E_c-E_b=0.65$ eV. Attributing this to D^0 defect states, the 'standard' defect model, would imply that although the profile is that of the D^0 states the bump centre energy is that for the D^- states from which electrons are released. The 'defect pool' model however permits the states to be D^+, in which case emission would be from D^0 states at the *same* energy, see §1.6. A difference in the trapping coefficients for

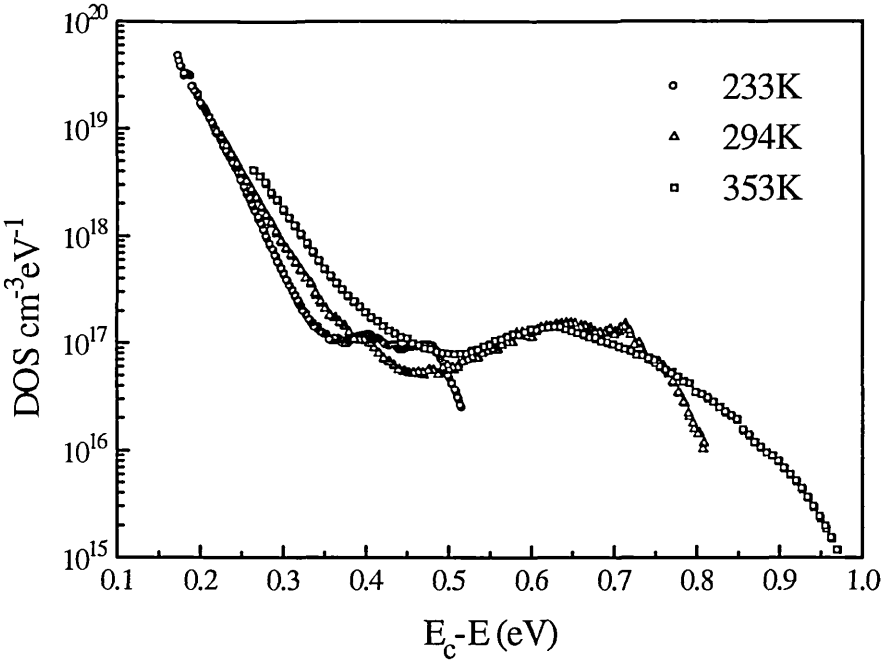

Figure 6.3 DOS distributions calculated from the TPC decays of figure 6.4 measured in the Stuttgart material at three different temperatures, assuming $\nu=10^{12}$Hz and $\mu=10\text{cm}^2(\text{Vs})^{-1}$

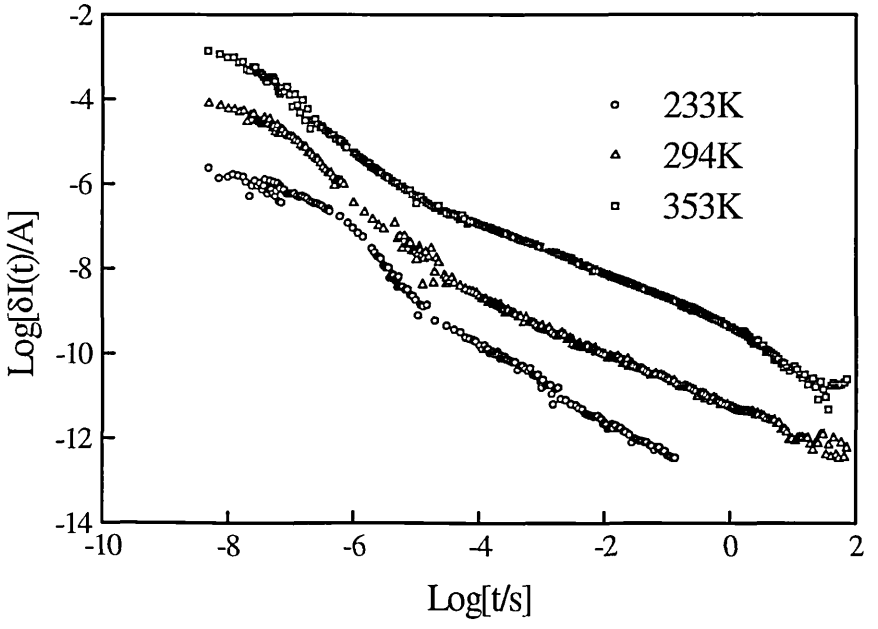

Figure 6.4 TPC decays measured at three different temperatures in the Stuttgart a-Si:H,δ $G=10^{16}\text{cm}^{-3}$.

the tail and defect states would also affect the energy position and magnitude of the density of the calculated defect state distribution. The inaccuracy in the slope of the shallow energy tail for temperatures such that $kT>kT_c$ occurs because of the broadening effect of the tails of the weighting functions in equations 3.6 and 3.7. The broadening also means that the precise shape of the defect distribution, Gaussian or otherwise, cannot be determined. The TPC decays are shown in figure 6.4. Note that a turn down in the decay signifying final recombination is only seen at the highest temperature, at 1 second. Using ν as above the Fermi level must therefore be at 0.85 eV below E_c or deeper which is larger than the value of 0.8eV obtained from the dark conductivity. An E_f of 0.8eV below E_c is consistent with not observing a recombination or saturation feature at lower temperature within the experimental time window.

A match to the experimentally observed TPC in the linear régime can be obtained by the finite difference simulation described in appendix A. Figure 6.5(a) shows the model DOS constructed to match the calculated DOS. The shallow energy states have an exponential distribution of energy 0.03ev extending to the band edge. The bump consists of a modified hyperbolic secant, i.e.: an increasing and then decreasing density of the same magnitude of exponential slope $|kT_b|$, in this case 0.07eV. The total bump density is $4.4\times10^{16}cm^{-3}$. Figure 6.5(b) compares the simulated and measured TPC; the very good fit over many orders of magnitude and time is achieved *without* any arbitrary scaling. The simulated decay is produced using the same υ, μ and conduction cross section parameters used to calculate the DOS from the experimental data.

6.2 Discussion of the deep bump interpretation

The steep decay can now be attributed to charge transfer between the tail and the bump. The fall begins when the total capture probability into tail states below $E_c - E_{th}$ is of the same order as the probability of capture by the defect bump, so that charge emitted from states at $E_c - E_{th}$ is recaptured into bump states rather than into the diminishing density of states just below $E_c - E_{th}$. The majority of trapped charge therefore shifts to the peak of the bump and TROK type thermalisation ceases until $E_c - E_{th}$ reaches the peak. TROK thermalisation then continues in the tail of the bump. The process is illustrated in figure 6.6 showing the charge distribution of the simulation of figure 6.5(b) at successive two decade intervals during the decay. Initially the charge can be seen thermalising as a packet in the shallow energy tail of the DOS. The packet then jumps to the peak of the deep energy bump. The charge trapped in states above $E_c - E_{th}$ can be seen to be released as $E_c - E_{th}$ moves to deeper energies. Finally when $E_c - E_{th}$ reaches E_b the charge packet starts to move again.

It is remarkable that there is no feature in the decays at the time, marked on figure 5.5(b), at which $E_c - E_{th}$ passes the bump peak energy. This possibility was pointed out by Schiff (1985) who considered the case of a bump distribution described

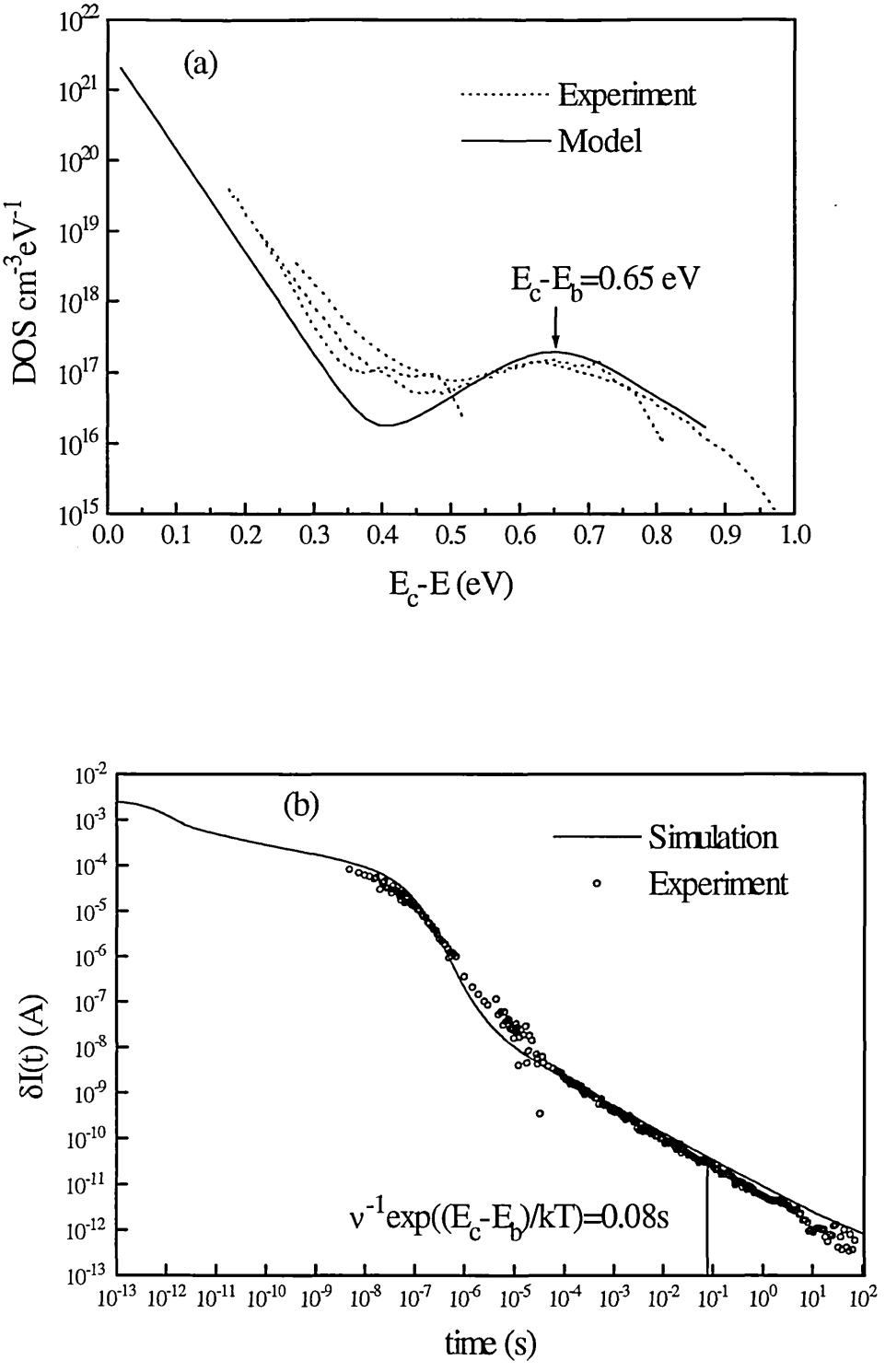

Figure 6.5 (a) Model DOS superimposed on calculated DOS for Stuttgart a-Si:H. (b) simulated TPC using the model DOS compared to experimental TPC ($\delta G=10^{16}cm^{-3}$). The same parameters as were used to calculate the DOS were used to scale the simulated TPC decay. The time marked is that at which the thermalisation energy passes E_b.

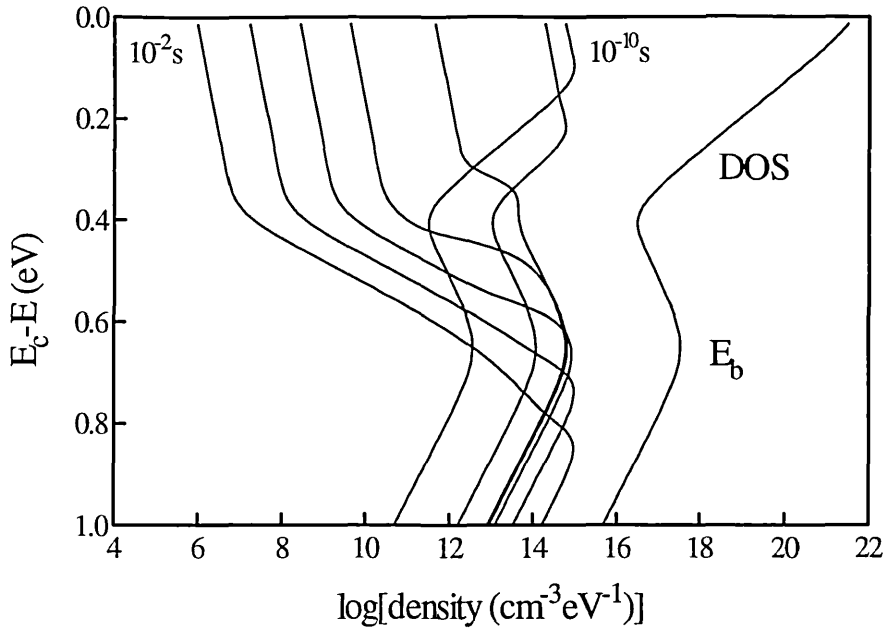

Figure 6.6 Density distribution of trapped charge at successive equally spaced instants during the simulated TPC decay of figure 6.5(b).

by a hyperbolic secant. When $E_c - E_{th}$ is deeper than E_b so that charge is thermalising in the deep side of the bump, as for an exponential tail, the current has a slope of $-(1-\alpha_b)$, $\alpha_b = T/T_b$. When $E_c - E_{th}$ is shallower than E_b charge is being emitted from states at $E_c - E_{th}$ and recaptured with a fixed trapping time into the peak of the bump. From equation 2.10 the expected power law index for this process in a falling exponential DOS is $-(1+\alpha)$. However, with the DOS *rising* at $E_c - E_{th}$ it appears that we can regard T_b and hence α to be negative so that we see the same index $-(1-\alpha_b)$ as for thermalisation.

The Fourier transform technique is able to detect the presence of the bump. The necessary information is contained in the ratio between the short and long time currents; therefore it is experimentally important that the high current region is sampled. This can be illustrated by applying the technique to the family of functions depicted in figure 6.7(a), consisting of a plateau region superimposed on a power law decay of slope 0.5. Figure 6.7(b) shows the ' DOS' which results for different values of the ratio between the plateau region magnitude P and the power law prefactor. With no plateau region the power law is interpreted as an exponential tail of characteristic energy 0.05 eV, as expected. Adding in the plateau causes the DOS to fall below the exponential at shallow energy (large ω) and return at deep energy (small ω), thereby forming a bump. The effect is more marked for a larger ratio. This happens because the DOS is inversely proportional to the magnitude of the Fourier integral (equation 4.1). At large ω the pulse dominates the Fourier integral. The relative contribution of the plateau region to the integral declines as ω decreases and the long time current contribution becomes more strongly weighted, until at small enough ω it is negligible. Note that the shallow energy 'tail' has a characteristic energy of 0.025eV, i.e.; kT. This is because the plateau region is

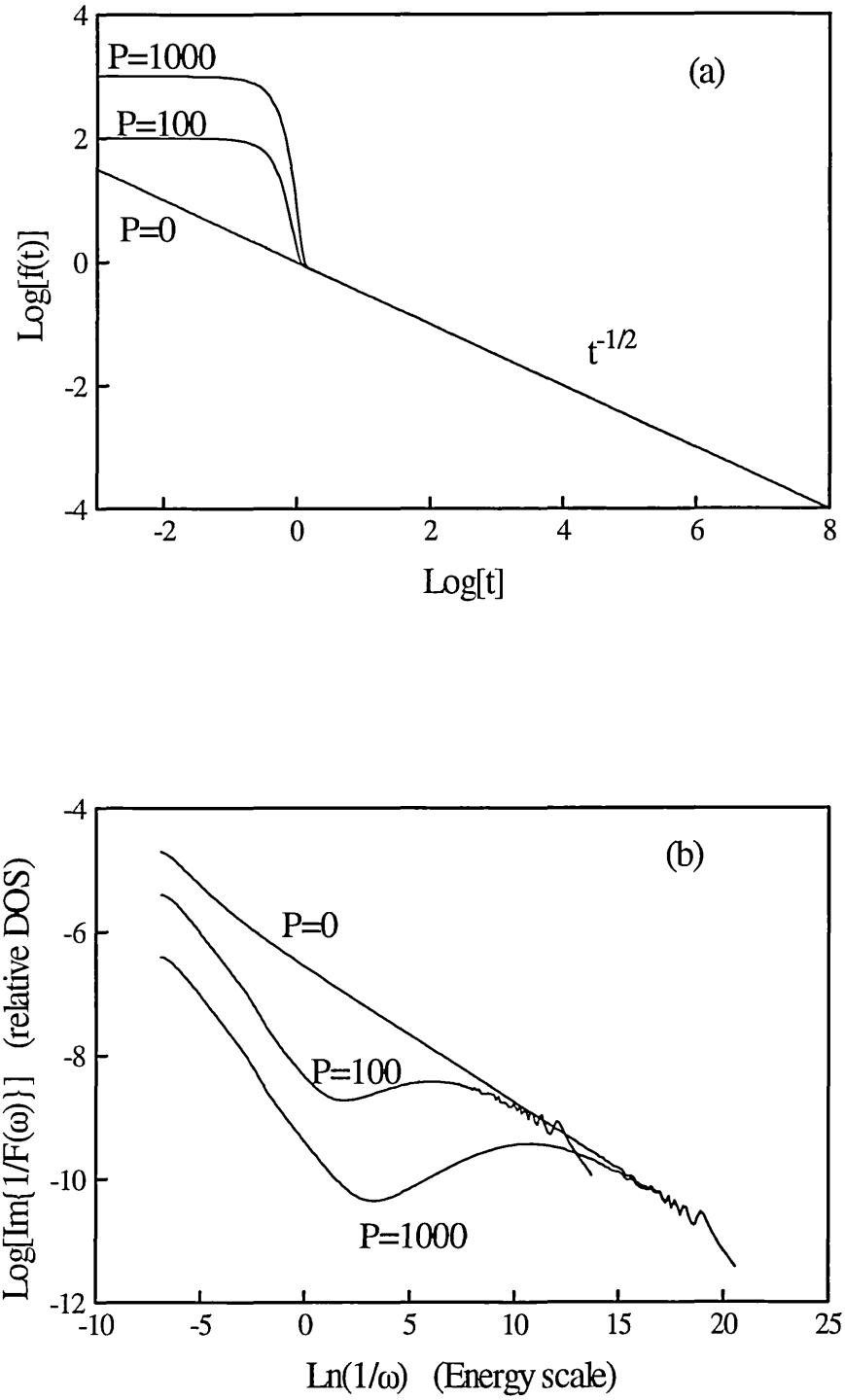

Figure 6.7 (a) Family of functions f(t) consisting of a power law $t^{-1/2}$ and a plateau region of magnitude P. (b) resulting of applying the Fourier transform DOS calculation procedure to f(t) for various values of P.

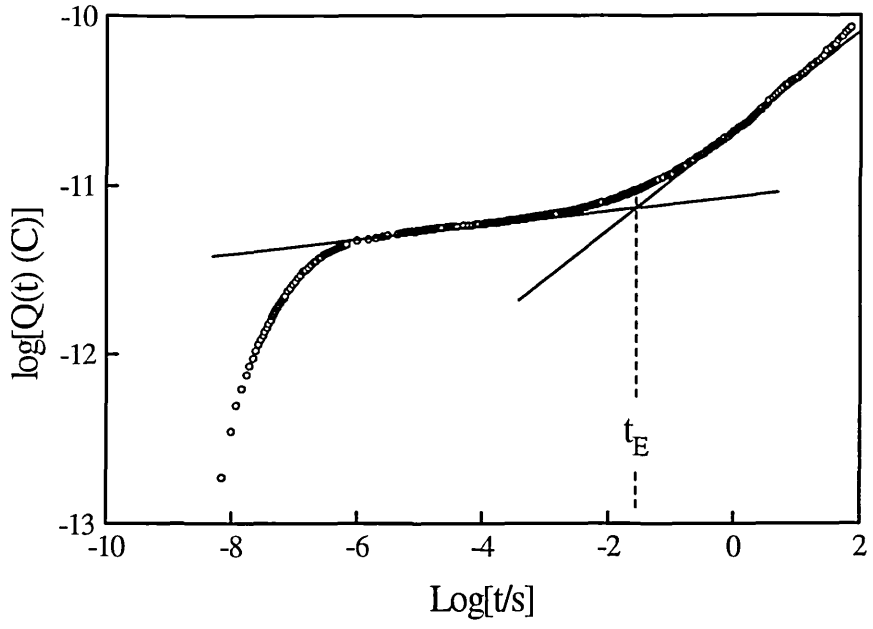

Figure 6.8 Time varying integral Q(t) of TPC in the Stuttgart a-Si:H ($\delta G=10^{16}cm^{-3}$). The time t_E is the emission time from deep states.

equivalent to a completely non dispersive transient current which would arise from a very sharp tail.

The ability of the Fourier transform technique to detect the deep traps is related to the emission time feature in transient photocharge experiments on a-Si:H described by Antoniadis and Schiff (1992). Transient photocharge Q(t) is measured with a coplanar or sandwich cell by using a detection circuit in charge collection configuration. If TPC has been measured to short enough time however Q(t) is just the time varying integral of $\delta I(t)$. Figure 6.8 shows the integral of the initial density $10^{16}cm^{-3}$ TPC decay in the Stuttgart material. Although the transient photodecay has no structure at the time t_E at which trapped charge in the bump is emitted a feature at this time *can* be seen in the plot of the transient photocharge because Q(t) is proportional to the average displacement of carriers. The rising short time integral corresponds to the relatively non-dispersive current region. The integral flattens off when the carriers start being deeply trapped, so that they can no longer contribute to the current, and the integral begins to rise again once this charge is released. In terms of the foregoing discussion concerning the Fourier integral of the analytic function we can look at the emission related rise as occurring when the integral of the power law is larger than the integral of the plateau region, illustrated in figure 6.9.

The emission time t_E obtained from the integrated TPC provides a feature the temperature dependence of which can be used to find υ and E_b from $1/t_E = \exp[(E_c - E_b)/kT]$. Unfortunately enough of the rise after emission to identify t_E is seen only for the three highest temperature transients of figure 6.4. Figure 6.10 shows the least squares fit to the data, giving $\upsilon=1.3\times10^{12}Hz$ and $E_c-E_b=0.63eV$.

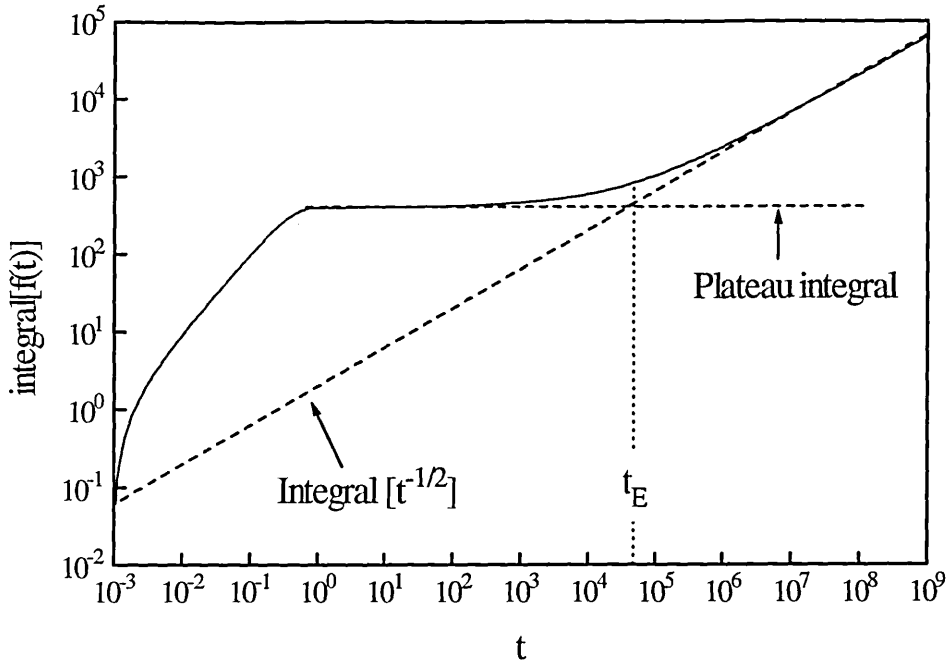

Figure 6.9 Integral of the function f(t) of figure 6.7(a) for $P=10^3$. The integral of $t^{-1/2}$ becomes larger than the integral of the plateau region at t_E.

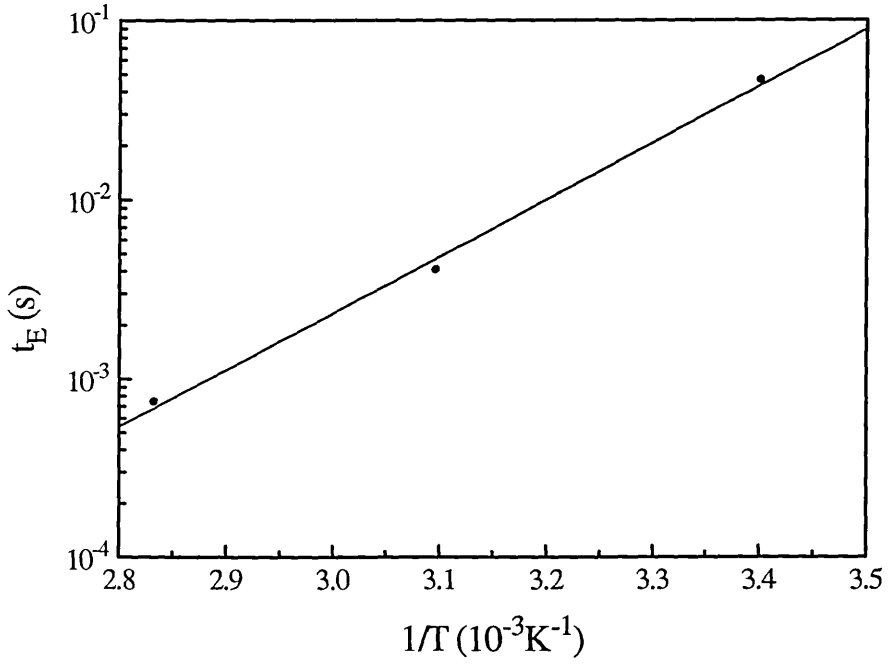

Figure 6.10 Activation energy of t_E in the Stuttgart a-Si:H. The plot gives $E_c - E_b = 0.63eV$ and $\nu=1.3\times10^{12}$Hz.

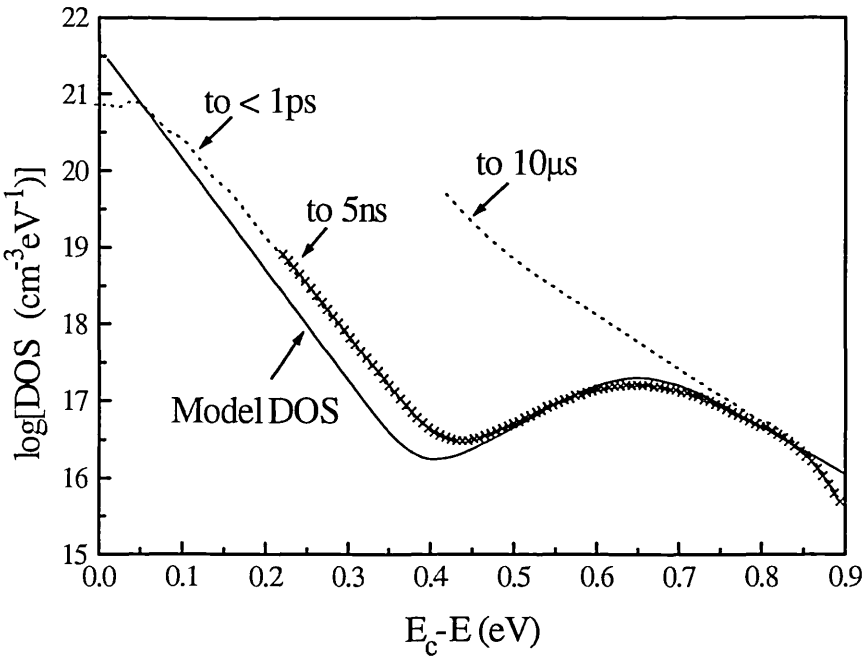

Figure 6.11 Effect on the recalculated DOS of truncating the simulated TPC decay of figure 6.5(b) at different times.

6.3 Validity of Fourier transform

The Fourier transform of the experimentally measured time response of a sample to impulse excitation is an approximation to the frequency response which is expected to be accurate within a reasonable range in frequency defined by the inverses of the minimum and maximum accessed times, see §4.3. The discussion in the previous section raises the possibility that even within the "reasonable range" the approximation may not be good. The question which must be asked is how large is the missing contribution to the Fourier integral from the portions of the decay outside the experimental time window? Figure 6.11 shows the effect on the calculated DOS of truncating the simulated transient of figure 6.5(b) at different times. It can be seen that an experimental time window that missed out the steep fall would lead to the calculation of an erroneous DOS distribution. This point is further pursued with respect to measurements on a-As_2Se_3 in chapter 9.

Is it possible to be sure that the Fourier transform of the a-Si:H data in figure 6.3 is a good approximation to the frequency response? There are several reasons to think so. First of all referring again to figure 6.11 the calculated deep DOS profile is not affected if the data is truncated at times before the deep trapping fall. This is an indication that the transform would only be seriously affected if there was unexpected structure in the decay at times shorter than the experimental minimum. However the size of the contribution of any such structure is limited because the drift mobility at 5ns is $0.36cm^2(Vs)^{-1}$, or to put it another way the photocurrent at 5ns is about 4% of the estimated current before any trapping has occurred. Although a two orders drop in the

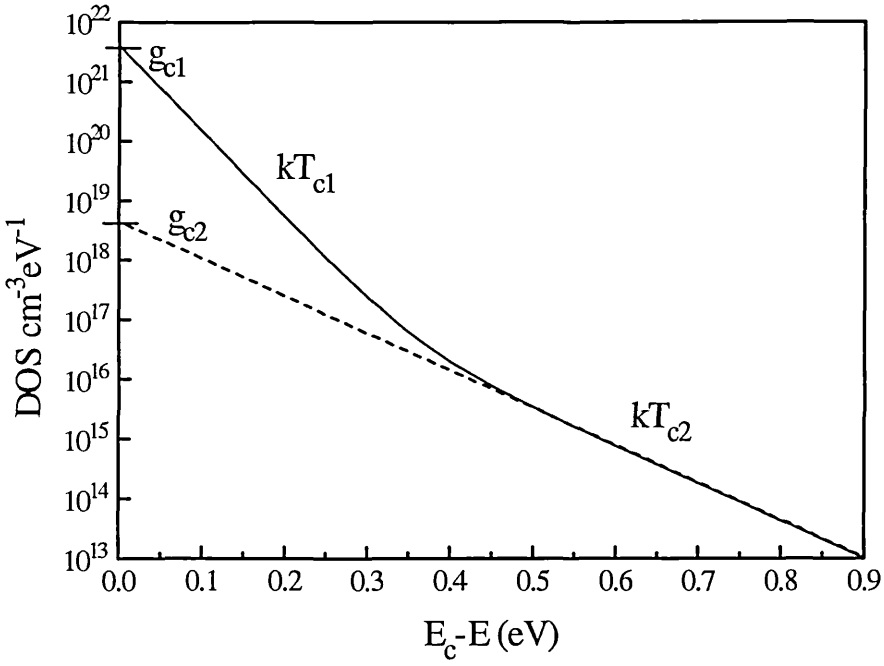

Figure 6.12 Two slope band-tail.

current just before 5ns would affect the calculated deep DOS, the trapping time into the shallow energy tail is around 1ps so it is unlikely that such structure exists. The drift mobility above compares with drift mobilities of around $1cm^2(Vs)^{-1}$ reported for undoped a-Si:H in time of flight experiments (Spear and Steemers 1983).

6.4 Thermalisation current magnitude

It is instructive to investigate what thermalisation in a two slope band tail such as in figure 6.12 would look like. The expression for the density of states is

$$g(E) = g_c \exp\left[-(E_c - E)/kT_{c1}\right] + g_{c2} \exp\left[-(E_c - E)/kT_{c2}\right] \qquad (6.1)$$

where g_c is the density of states at the mobility edge and g_{c2} is the extrapolated density of states at the mobility edge for the second tail. When charge is thermalising in the second tail we need to replace T_c and g_c in equation 2.2 for the trapped charge density with T_{c2} and g_{c2}. Then eliminating δf_d as before with equation 2.3 we obtain

$$\mu_d = \mu_0 \frac{g_c}{g_{c2}} \alpha_2 (1-\alpha_2)(\nu t)^{-(1-\alpha_2)} \qquad (6.2)$$

where $\alpha_2 = T/T_{c2}$.

For the long time power law decay ($t>1\mu s$) in Stuttgart a-Si:H of figure 6.1, assuming a value for μ_0 of $10cm^2(Vs)^{-1}$, the ratio g_c/g_{c2} is approximately 0.1, i.e.: $g_c<g_{c2}$!

In other words the DOS cannot be of the form in equation 6.2 because the magnitude of the long time current is too small.

6.5 Intensity dependence

Figures 6.13 (a) and (b) shows TPC decays measured in the Stuttgart and Cambridge samples over four orders of photogeneration pulse intensity. Both sets of data show the same features. At short times there is a marked sublinearity in the photocurrent magnitude with intensity and at long times and high intensity the photocurrent is virtually generation independent, the transients tending to coalesce into a common decay. The sublinearity suggests that at high laser intensity charge is being lost before 5ns by recombination. Such early recombination is observed in undoped a-Si:H in photoinduced absorption (PA) experiments which can detect the evolution of trapped as well as free carrier densities after a photoexcitation pulse with a time resolution of picoseconds. The recombination process is non-radiative (Mourchid et al 1990). A transition is seen between monomolecular behaviour below around $10^{18}cm^{-3}$ photocarriers and bimolecular above. Wake and Amer (1983) compared this transition density with the width of the Urbach edge to conclude that dangling bonds are not mediating the early recombination. Juska et al (1993) see the same transition using a photo-space charge limited current technique but the bimolecular recombination coefficient they deduce does not agree with that for the optical measurements. They agree that dangling bonds are not mediating the early recombination and suggest an Auger process. Referring again to figure 6.13 apparently bimolecular recombination begins *within* the experimental time window for both materials for the $10^{17}cm^{-3}$ initial density decay: the transient photocurrent is a factor of ten larger than the $10^{16}cm^{-3}$ current at 5ns but is only a factor of 3 larger at 1ms.

Figure 6.14 shows simulated TPC using the model DOS of figure 6.5(a) and the experimental initial photocarrier densities. The quantitative match above 10^{16} carriers cm^{-3} with figure 6.13(a) is not good. The numerical model includes only Shockley-Read transitions so a different mechanism, for example Auger recombination, coming into play at high intensity would not be reproduced by the simulation. However the same qualitative behaviour is apparent: sublinearity at short time and a 'common decay' at long time and high intensity. In the simulation bimolecular recombination is a consequence of the transient trapped carrier density exceeding the steady state density because the recombination rate is then controlled by the transient carrier density trapped in the band-tails. Figure 6.15 shows the effect of forcing recombination to be monomolecular even at high initial carrier densities. The capture coefficients of occupied band tail states in the model DOS have been set to zero and recombination is mediated by a single level of $4.4\times10^{16}cm^{-3}$ states at midgap. At high initial photocarrier density the tail states simply saturate, causing the short time TPC intensity dependence to be *superlinear*. At long

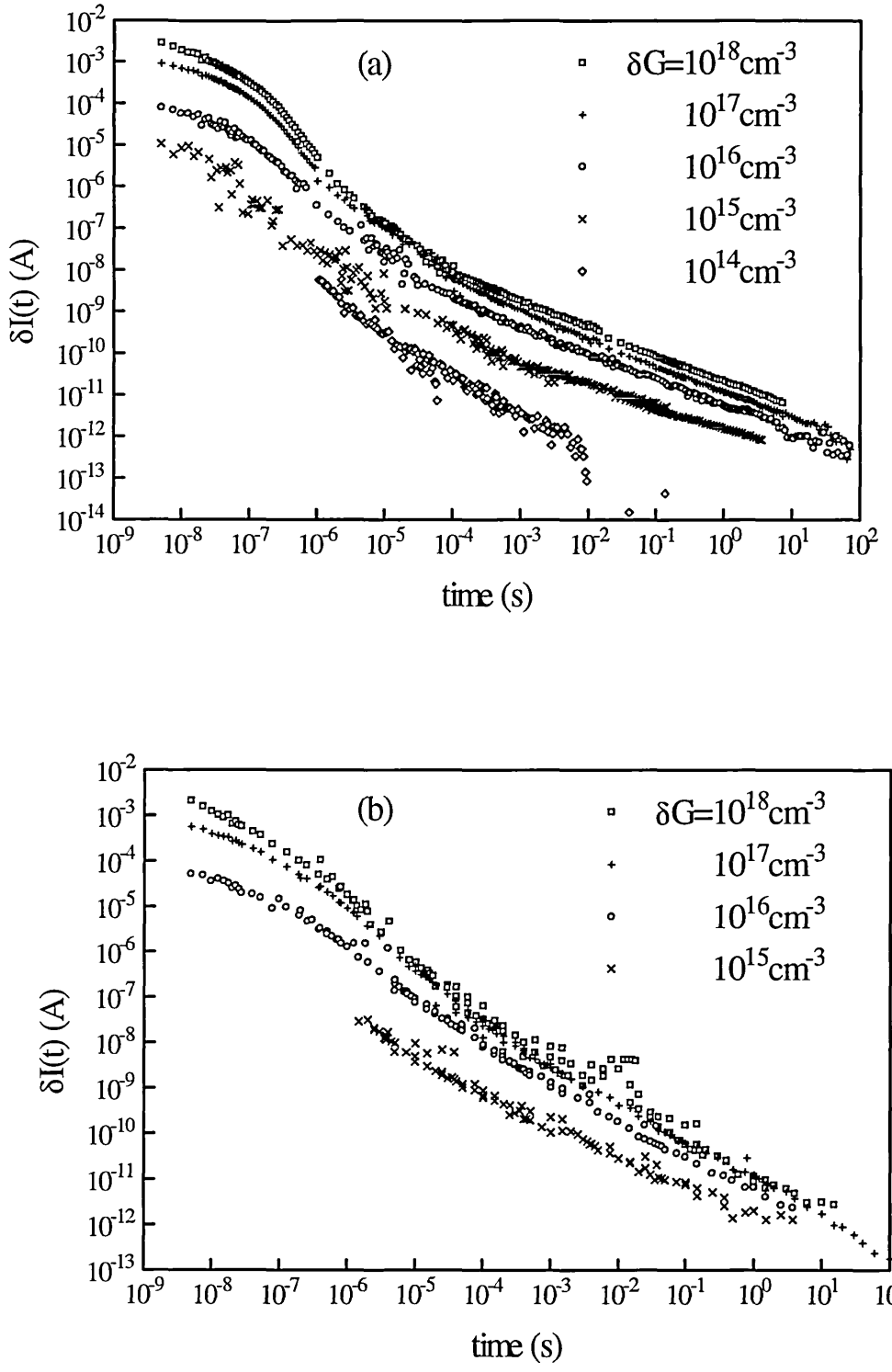

Figure 6.13 TPC at varying pulse intensity in (a) the Stuttgart and (b) the Cambridge undoped a-Si:H.

time the photocurrent is controlled by emptying and removal by recombination of the charge in the saturated states. The 'common decay' is seen because over a range of initial photocarrier density the states are identically occupied, i.e.; are full. In the bimolecular 'common decay' the states are not completely saturated but fill to a pulse intensity independent occupation determined by the trapping and recombination parameters, see §7.14.

Finally it is noted that the $\delta G=10^{14}cm^{-3}$ Stuttgart a-Si:H decay behaves anomalously, decaying with a power law slope of around t^{-1}. The author is not able to offer an explanation for this.

6.6 Summary

The Fourier transform technique for calculation of DOS distributions from transient photocurrent data described in chapter 4 is applied to experimental measurements on samples of undoped a-Si:H. The technique yields a DOS consisting of a sharp 0.03 eV exponential tail with a bump at 0.65 eV below E_c, in agreement with accepted models for undoped a-Si:H. The calculated DOS covers almost half the mobility gap. The Fourier transform technique is able to detect the bump despite there being no feature in the TPC decay at the time at which charge trapped in the bump states is released. A simulation using the calculated DOS and the same trapping parameters as were used to calculate the DOS reproduces the observed TPC decay. It is demonstrated that the shape of the deep energy calculated DOS is dependent on the relative magnitude of the pre- and post-deep-trapping decay currents, and that removing pre-deep-trapping data from the Fourier summation causes the calculated DOS to be distorted. It is argued from an estimate of the theoretical maximum value of the transient photocurrent (the pre-trapping current) that the effect of the missing contribution to the Fourier summation from TPC at times shorter than those experimentally observed is negligible. It is also demonstrated that the magnitude of the post-deep-trapping photocurrent is too small to be attributed to thermalisation in an exponential distribution of deep states with a prefactor smaller than the band edge DOS for a-Si:H.

At pulse photogeneration intensity greater than $10^{16}cm^{-3}$ it is observed that the short time TPC magnitude varies sublinearly with pulse intensity and that at long times the decay is almost completely insensitive to pulse intensity. These features are qualitatively reproduced by simulation. To account for the observations it is proposed that TPC in the high intensity régime is controlled by bimolecular recombination mediated by some other path than dangling bonds. The current at long times reflects the emission of deeply trapped charge from states left filled to an intensity independent occupation by the short time recombination process. It is demonstrated by simulation that recombination in the high intensity régime mediated solely by a fixed density of dangling bonds would result in a superlinear intensity dependence at short times.

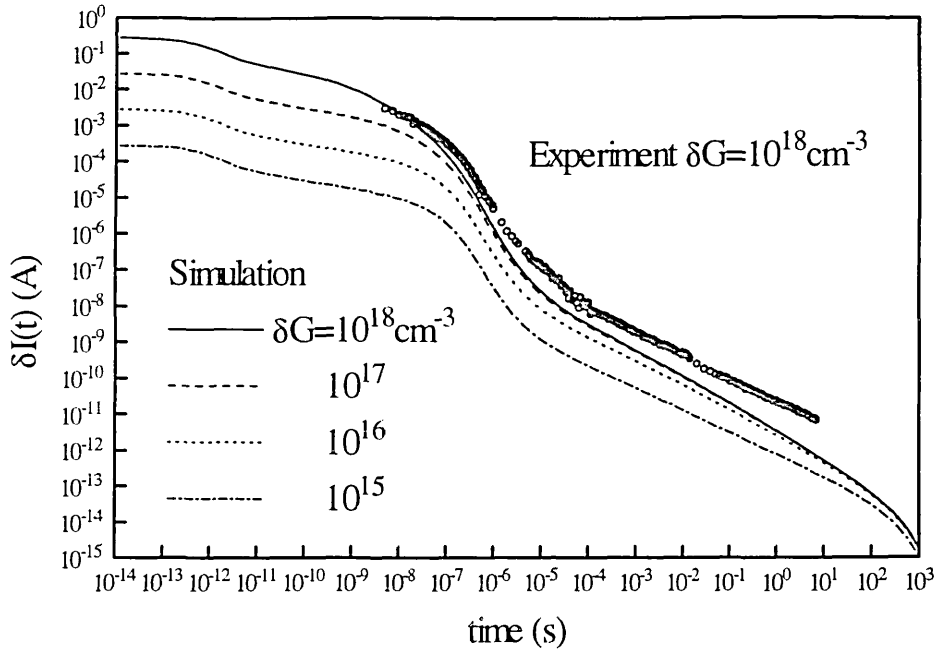

Figure 6.14 Simulated TPC decays at different pulse intensities using the model DOS of figure 6.5(a).

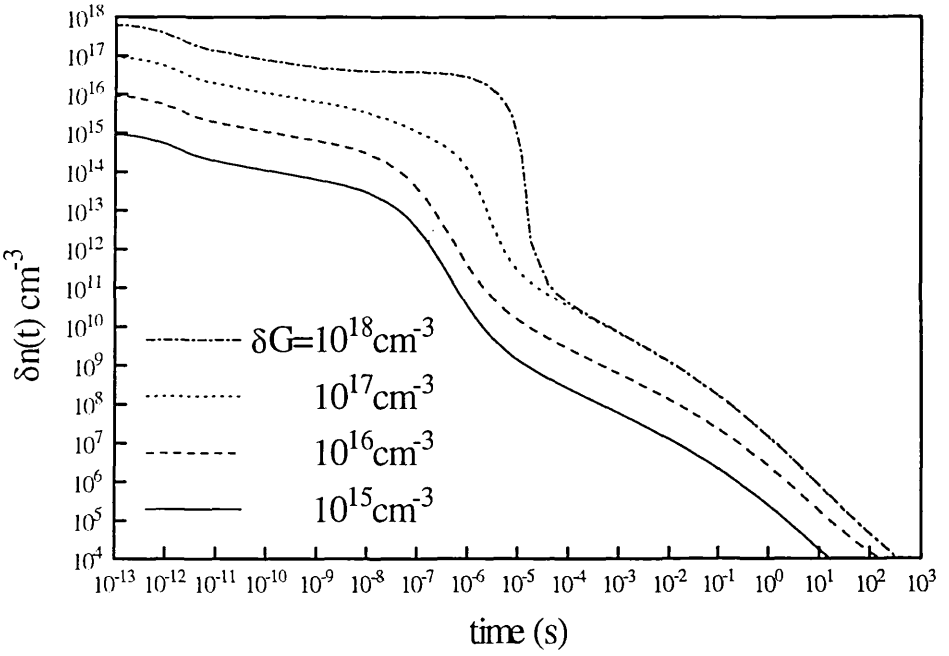

Figure 6.15 Simulated TPC decays with recombination constrained to occur through a single level of $4.4\times10^{16}cm^{-3}$ states and using the DOS of figure 6.5(a).

7.1 The undershoot

Measurements of TPC on both the Cambridge and Stuttgart material under appropriate conditions of optical bias exhibit an undershoot in the transient response δI(t). This is to say that δI(t) becomes negative because the *total* photocurrent drops below the bias illumination generated steady state photocurrent I_{ss}. A detailed investigation of how the time at which the undershoot occurs is influenced by optical bias intensity and temperature is described below.

7.2 Experimental characterisation of undershoot

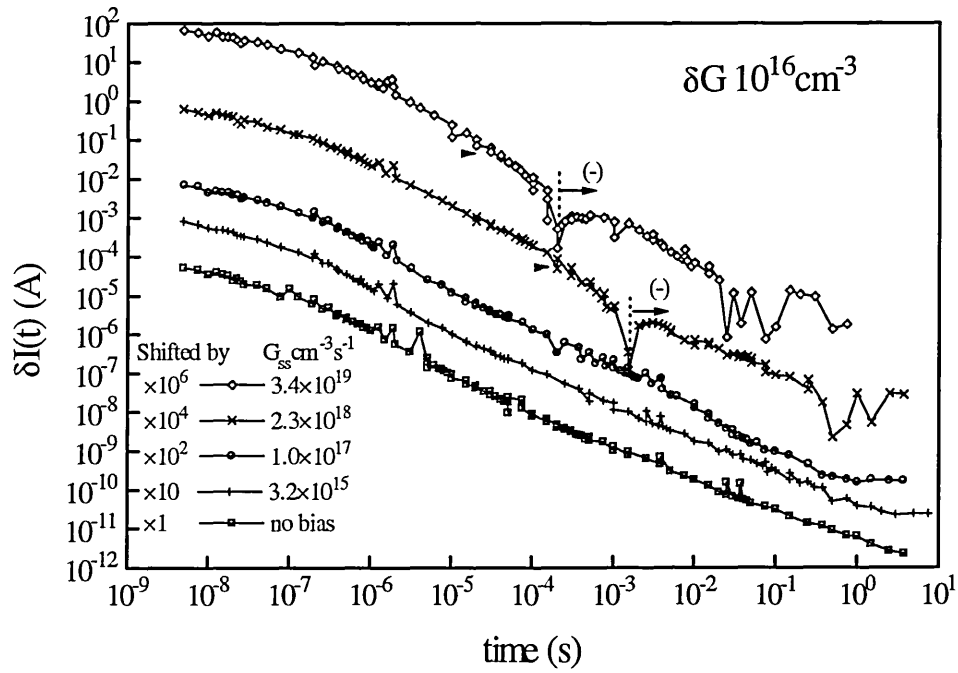

Figure 7.1 TPC with optical bias measured in the Cambridge a-Si:H. An arrow and a (-) indicate portions of the decays which are negative. The decays have been shifted by the indicated factors for clarity. The bare arrowhead indicates the value of δn^*, see §7.53.

Figure 7.1 shows decays measured in the Cambridge material with an initial laser generated electron-hole pair density of $10^{16}cm^{-3}$ and steady state generation varying between 3×10^{15} and 3×10^{19} electron-hole pairs $cm^{-3}s^{-1}$. Note that the y-axis represents the *absolute* value of the transient photocurrent. Thus the undershoot which is seen in the two decays

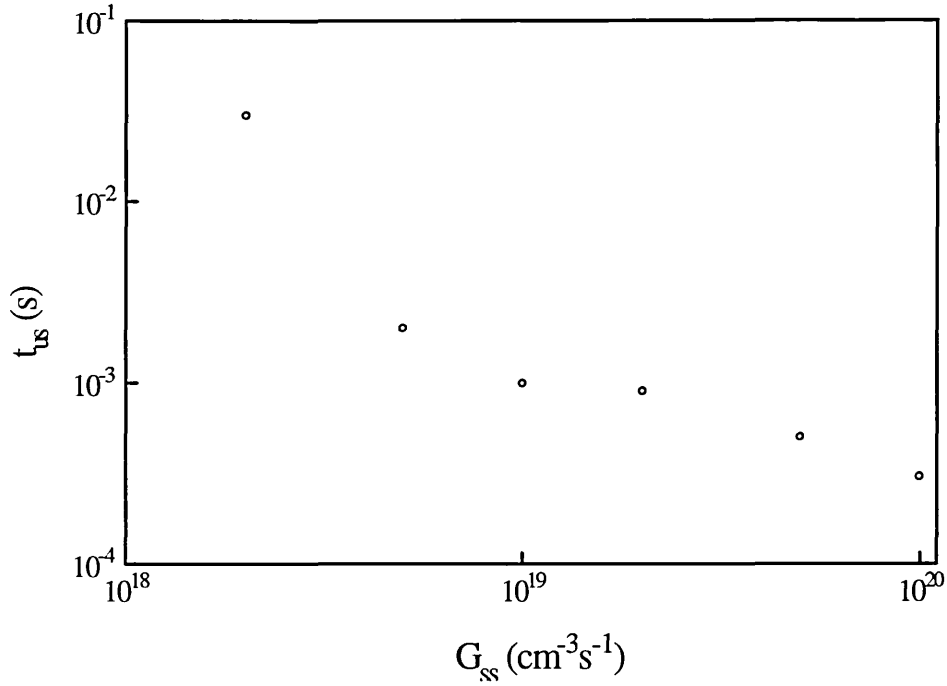

Figure 7.2 Undershoot time for the Cambridge a-Si:H plotted against steady state generation rate, $\delta G=10^{16}cm^{-3}$.

with the highest optical bias appears as a characteristic cusp, $\delta I(t)$ before the cusp being positive and that afterwards negative. It can be seen that the undershoot moves to longer times with decreasing optical bias. Below a bias of about $3\times10^{18}cm^{-3}s^{-1}$ it is not possible to observe an undershoot within the experimental time window. The undershoot time t_{us}, i.e.; the time at which the sign of δI reverses, shifts by about one order for a bias variation of one and a half orders, figure 7.2. Figure 7.3, using data from the same set of measurements shows the undershoot time plotted as an associated thermalisation energy using $E_{us} = kT\ln(\nu t_{us})$ against the estimated quasi-Fermi level shift E_{fn}-E_f calculated from the ratio of the dark current and steady state photocurrents There is some scatter in the points but the variation appears to be sublinear.

In a further experiment it was attempted to obtain an 'activation energy' for the undershoot. The trial assumption was made that there is a temperature independent offset ΔE_{us} between the thermalisation energy and the quasi-Fermi level. $\Delta E_{fn}=E_{fn}-E_f$ was kept constant at 0.24eV as the temperature was changed by varying the bias intensity to keep $kT\ln(I/I_d)$ a constant. The results are shown in figure 7.4, from which an activation energy E_{act} of 0.36 eV is obtained. The associated *thermalisation* energy E_{us} showed some temperature dependence however, changing from 0.54 eV at 305K to 0.57 eV at 355K. This places $E_c - E_{us}$ close to E_{fn} for E_f=0.8eV at room temperature. To reconcile the

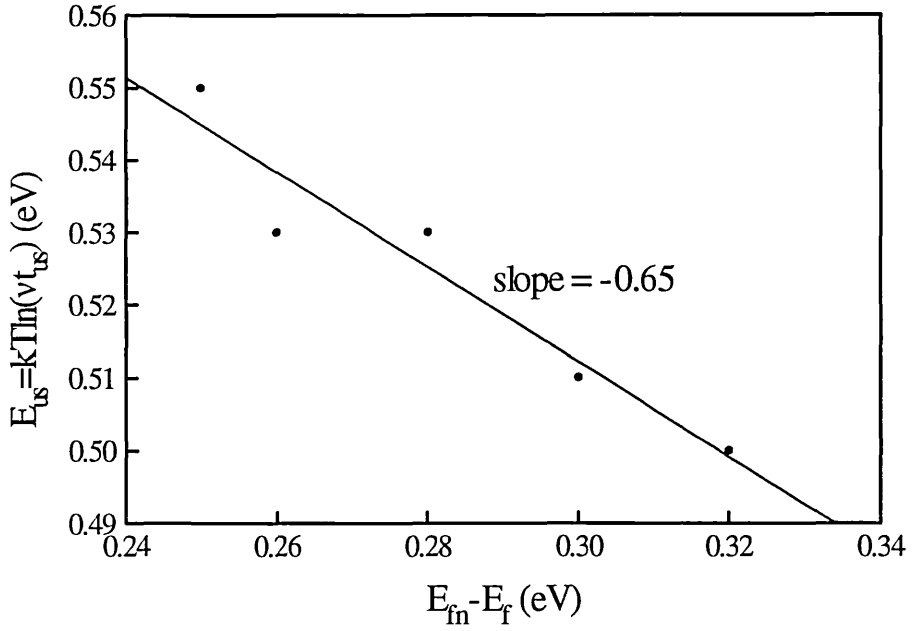

Figure 7.3 Data of figure 7.3 replotted as E_{us} versus $E_{fn}-E_f$, one data point ignored.

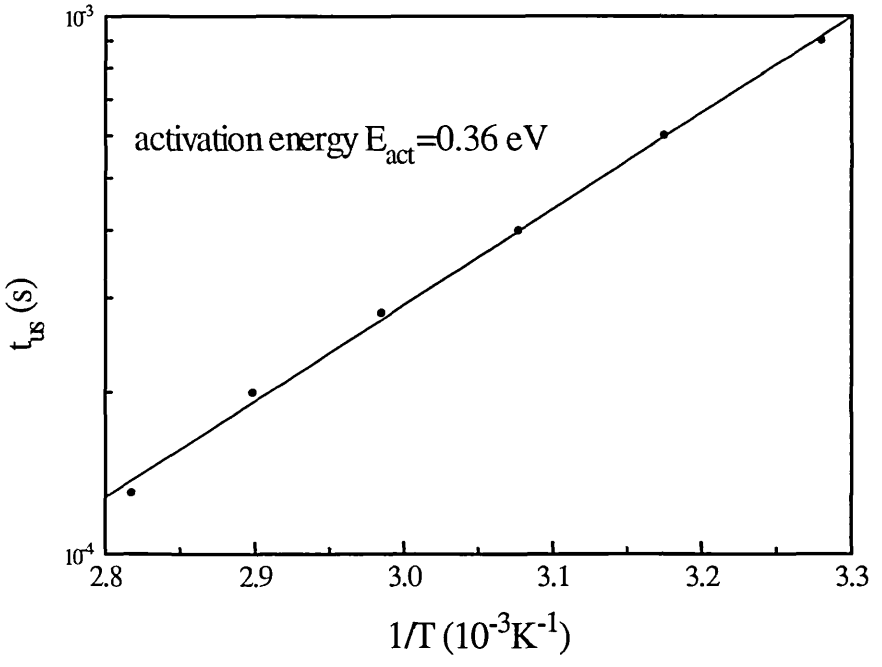

Figure 7.4 Activation energy of the undershoot time in the Cambridge a-Si:H with $E_{fn}-E_f$ maintained constant at 0.24 eV, $\delta G=10^{16}cm^{-3}$.

activation energy with the thermalisation energy appeal can be made to the temperature dependence in E_f, refer to §1.5. If we have

$$E_c - E_{us} = E_f + \Delta E_{fn} + \Delta E_{us} \qquad (7.1)$$

then analogously with equation 1.6 and the measurement of the conductivity activation energy we would expect

$$E_{act} = (E_c - E_f)_0 - \Delta E_{fn} - \Delta E_{us} \qquad (7.2)$$

For the Cambridge material $(E_c\text{-}E_f)_0$ is 0.71eV, so putting the experimental figure for E_{act}=0.36eV into equation 7.2 gives a value for ΔE_{us} of 0.11eV, in disagreement with the value of around 0.02eV from putting $E_c - E_{us}$=0.54eV into equation 7.1. It would therefore appear that the time at which undershoot occurs is not simply linked to the time at which charge release occurs from a particular energy depth above E_{fn}.

7.3 Theoretical treatment of Pandya and Schiff

An alternative approach to investigating the undershoot phenomenon arises from a theoretical treatment by Pandya and Schiff (1985) of multiple trapping TPC in the presence of optical bias in which they predict the observation of an undershoot for *bimolecular recombination* with a particular combination of model parameters. The rate equations are linearised and solved in the frequency domain. A sign reversal is also predicted in the quadrature spectrum of the Fourier transform of the TPC decay at a frequency ω which can be related simply to the model parameters. Note that literature searches for reports of the *experimental* observation of undershoot in a-Si:H, including a search on articles citing the Pandya and Schiff paper, have been unsuccessful. In the following the basis and results of the treatment will be presented. The physical meaning of the model parameters required to produce an undershoot will then be discussed and finally experimental and simulation results will be presented and analysed in terms of ω

The treatment uses a model of a material with a distribution of traps having an energy independent trapping coefficient. The carrier is chosen to be an electron and in addition to the multiple trapping assumption of conduction only by carriers in states above the mobility edge (§2.2) it is assumed that recombination occurs via trapped hole capture of free electrons, i.e.; filled electron traps do not capture holes. This assumption permits the steady state trap occupation function to be reduced to the ordinary Fermi function centred

on E_{fn} and recombination to be represented as an explicit function of the free and trapped electron densities. The rate equations representing the situation are as follows:

$$\frac{dn}{dt} = G - \int \frac{dn_t}{dt} dE - R \tag{7.3}$$

$$\frac{dn_t(E)}{dt} = nC_n(g(E) - n_t(E)) - n_t(E)C_n\bar{n} \tag{7.4}$$

where G is the generation rate, R the recombination rate and $n_t(E)$ the density distribution of occupied states. The variables in 7.3 and 7.4 can be expressed as the sum of a steady state part, subscripted 'ss' and a transient, time dependent part.

$$\begin{aligned} G(t) &= G_{ss} + \delta G(t) \\ n(t) &= n_{ss} + \delta n(t) \\ n_t(t) &= n_{tss} + \delta n_t(t) \\ R(t) &= R_{ss} + \delta R(t) \end{aligned} \tag{7.5}$$

The form of R(t) depends on the recombination mechanism. For monomolecular recombination the recombination rate is simply proportional to the free carrier density (see §1.7), so that $R=n/\tau$ with τ constant and therefore

$$\delta R = \delta n / \tau \tag{7.6}$$

For bimolecular recombination the recombination rate is proportional to the product of the free carrier density and the trapped hole density. The trapped hole density can be equated to the trapped electron density N_t, assuming the free electron and hole densities are much smaller than the trapped densities. Consequently $R=nC_RN_t$, where C_R is the capture coefficient of the trapped holes, and to first order

$$\delta R = \delta n C_R N_{tss} + n_{ss} C_R \delta n \tag{7.7}$$

where $N_t(t)=N_{tss}+\delta N_t(t)$. *The undershoot is a consequence of the second term in equation 7.7*, i.e.; of the effect of the transient density of trapped holes on the background *steady state* density of free electrons.

The system is linearised in δG by assuming that second order terms in δn and δn_t can be neglected. Pandya and Schiff are thus able to use Fourier transforms and solve for δn in the frequency domain. They obtain

$$\delta n = (\delta G - \delta R)\left[i\omega + \int dE g(E) C_n \{1-f\} \frac{i\omega}{i\omega + n_{ss} C_n + \bar{n} C_n} \right]^{-1} \qquad (7.8)$$

where $\delta n(\omega)$, $\Delta G(\omega)$, $\delta R(\omega)$ are the Fourier transforms of $\delta n(t)$, $\Delta G(t)$, $\delta R(t)$ respectively. Equation 7.8 is just the expression obtained by Oheda for the MPC analysis, equations 3.5-3.7, with the recombination term $\delta n(\omega)/\tau$ replaced by $\delta R(\omega)$. This is unsurprising in view of the argument in §4.1 relating the MPC spectrum to the complex transfer function of the semiconductor.

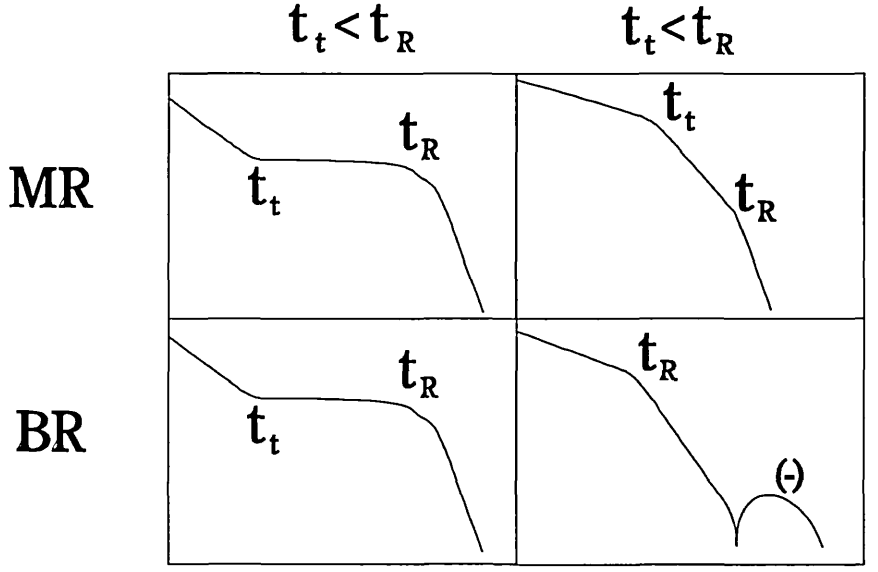

Figure 7.5 Diagram of behavioural régimes for TPC with optical bias identified by Pandya and Schiff (1985). A régime is characterised by the recombination mechanism, MR (monomolecular) or BR (bimolecular), and whether the charge packet thermalises (reaches the quasi-Fermi level) before ($t_t<t_R$) recombination begins or not ($t_t>t_R$). The undershoot (-) is predicted to occur for bimolecular recombination and ($t_t>t_R$).

Pandya and Schiff calculated $\delta n(\omega)$ and thus $\delta n(t)$ numerically for an exponential DOS and identified four distinct régimes of the solution, illustrated in figure 7.5. The régime of the solution is determined by two factors, the recombination mechanism (monomolecular or bimolecular) and the relationship between the observed recombination time t_R and the thermalisation time t_T at which $E_{th}(t)$ crosses E_{fn}. Undershoot occurs in the régime of bimolecular recombination when $t_R<t_t$. According to the analysis for bimolecular

recombination the relationship between t_R and t_t is independent of the steady state generation rate and is controlled instead by the ratio of the trapping and recombination coefficients: $t_R<t_t$ if $C_R>C_n$. Thus the observation of undershoot in the Cambridge and Stuttgart samples immediately indicates that recombination is bimolecular and that the recombination coefficient is larger than the capture coefficient, assuming that the analysis results are not crucially dependent on the shape of the DOS. A further caveat is that undershoot is not observed in the Stuttgart samples below $\delta G=10^{17}cm^{-3}$ electron-hole pairs, which is in the non-linear response régime, and not in the Cambridge samples below $\delta G=10^{16}cm^{-3}$. Thus undershoot in undoped a-Si:H may only occur for non-linear response. However the response of the simulation model in the non-linear régime, presented in §7.5, may indicate that the general features of the Pandya and Schiff analysis for linear response are still valid.

7.4 Discussion of results of theoretical treatment

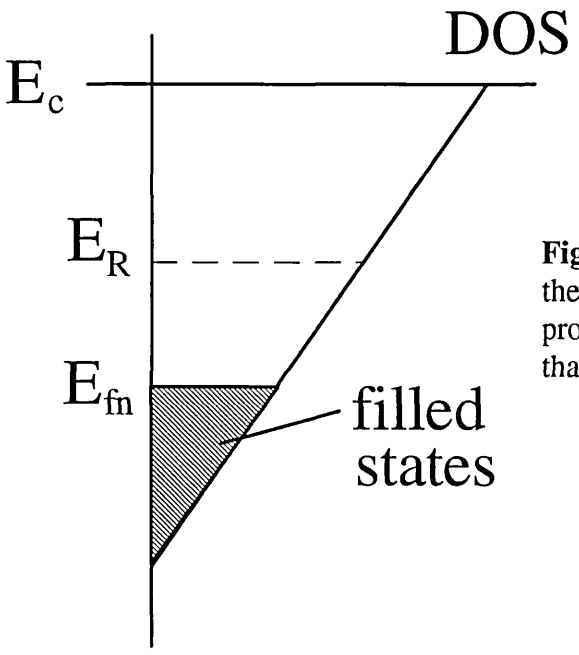

Figure 7.6 Exponential tail with states below the quasi-Fermi level filled. The capture probability for free electrons into states deeper than E_R equals the recombination probability.

Insight into the above results can be gained by considering a simple physical picture. There are three features to be explained: why does undershoot occur for bimolecular recombination, why does $C_n>C_R$ imply that the transient charge completely thermalises (reaches E_{fn}) before recombination starts, and finally why does undershoot *not* occur if the transient charge completely thermalises before recombination starts.

The first question has already been answered by considering equation 7.7 above. The second question can be answered by reference to figure 7.6 illustrating an exponential band tail $g(E)=g_c\exp[-(E_c-E)/KT_c)$ with all states below E_{fn} occupied and therefore not available to capture free charge. A recombination time feature will be observed in the

transient at a time $t_R<t_t$ if there is some energy E_R shallower than E_{fn} the probability for capture of free electrons into tail states deeper than which is equal to the probability of recombination. Mathematically this can be expressed as

$$kT_c g(E_R) C_n \approx N_{tss} C_R \tag{7.9}$$

where $kT_c g(E_R)$ is the integrated tail density deeper than E_R. The steady state density of trapped electrons N_{tss} is just the integrated tail density below E_{fn}:

$$N_{tss} \approx kT_c g(E_{fn}) \tag{7.10}$$

Substituting 7.10 into 7.9 gives

$$\frac{C_n}{C_R} \approx \frac{g(E_{fn})}{g(E_R)} \tag{7.11}$$

Equation 7.11 shows that $C_n<C_R$ implies that $g(E_{fn})<g(E_R)$, i.e.; that E_R is shallower than E_{fn} so that recombination occurs before thermalisation. Equation 7.9 can also be used to show that the transient occupation of deep states δf_d when recombination starts is independent of δN_t. From equation 2.5

$$\delta f_d \approx \frac{\delta N_t}{kTg(E_R)} \tag{7.12}$$

δN_t can be eliminated by substitution from equation 7.9, giving

$$\delta f_d \approx \frac{C_n T_c}{C_R T} \tag{7.14}$$

This still leaves the question as to why no undershoot occurs after thermalisation. The answer lies in the relative magnitudes of the two contributions to the bimolecular recombination rate in equation 7.7. Undershoot occurs under the condition that δn is small enough that the second term, $n_{ss} C_R \delta N_t$, dominates over the first term, $\delta n C_R N_{ss}$. If the first term dominates the decay is simply quasi-monomolecular (Pandya and Schiff, 1983), with $\tau_R = (C_R N_{ss})^{-1}$. If the trapped charge has completely thermalised, i.e.; it cannot become more deeply trapped because the charge packet has reached the Fermi level, then the ratio of free to trapped charge $\delta n/\delta N_t$ is constant because the whole charge packet is in thermal

contact with extended states. Thus $n_{ss}C_R\delta N_t/(\delta nC_R N_{ss})$ becomes constant and no undershoot occurs.

7.5 Comparison of theory with experiment and simulation

Pandya and Schiff state that "the time at which the sign reversal occurs (in the transient photocurrent) is not simply related to the microscopic parameters". However their analysis also predicts a sign reversal in the imaginary part of the *Fourier transform* of the transient photocurrent which can be related to the recombination coefficient. The relation is

$$\omega_- = n_{ss}C_R \qquad (7.15)$$

where ω_- is the angular frequency of the sign reversal. As with the rest of the analysis this result is obtained for the specific case of an exponential tail.

7.5.1 Computer Simulation

It has proved possible to obtain an undershoot in simulated decays when the model parameters are altered to reflect the conditions of the theoretical analysis, ie; recombination occurs through the path of free electron capture into trapped holes, and $C_R > C_n$. The recombination path condition is achieved by setting the capture coefficient for occupied conduction band tail states to zero, so that they cannot capture free holes. In fact it is found sufficient to make the coefficient smaller than that for occupied valence band tail states. The fact that such an asymmetry in the capture coefficients is required to reproduce the undershoot behaviour may be an indication that one recombination path dominates under the experimental conditions in the real material.

Figure 7.7(a) shows simulations for an exponential conduction band tail of characteristic energy kT_c=0.07eV using an initial transient free electron density δG of $10^{14}cm^{-3}$ and varying steady state generation, with the corresponding imaginary parts to the Fourier transform in figure 7.7(b). C_R (ie; the capture coefficient of the trapped holes) was $10C_n=10^{-7}cm^3s^{-1}$. This value was chosen merely to make C_R larger than C_n.

Table 7.1 compares C_R calculated from ω_- using equation 7.15 with the value estimated from n_{ss}. The estimate is made by assuming, as in the derivation of equation 7.11, that the recombination centre density is equal to the density of trapped electrons and that the occupation below the quasi-Fermi level is unity. Using $n_{ss}=G_{ss}\tau$ gives

$$C_R = \frac{G_{ss}}{n_{ss}}\left(\int_{E_f}^{E_{fn}} g(E)dE\right)^{-1} \qquad (7.16)$$

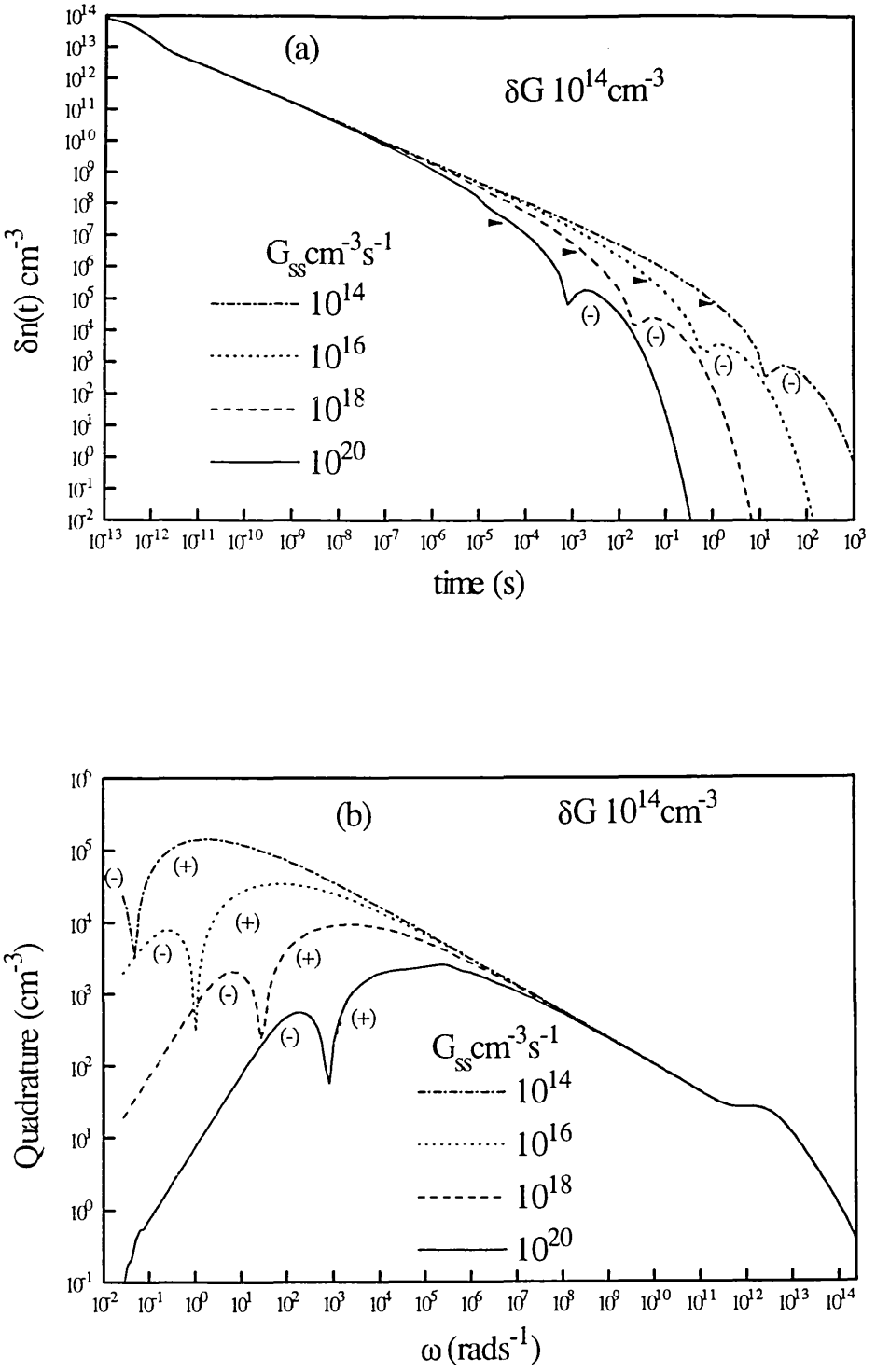

Figure 7.7 (a) Simulated TPC with optical bias for an exponential tail (kT_c=0.07eV) and C_R=10C_n, (b) Fourier transform quadrature spectra calculated from the TPC decays. The bare arrowheads on (a) mark the values of δn^*, see §7.53.

Table 7.1 C_R calculated from simulated data using exponential DOS (kT_c=0.07eV). Actual model $C_R=10^{-7}cm^3s^{-1}$

G_{ss} $cm^{-3}s^{-1}$	δG cm^{-3}	C_R cm^3s^{-1} from ω_-	C_R cm^3s^{-1} from n_{ss}
10^{14}	10^{14}	6.8×10^{-8}	1.9×10^{-7}
10^{16}	10^{14}	6.6×10^{-8}	1.3×10^{-7}
10^{18}	10^{14}	6.3×10^{-8}	1.3×10^{-7}
10^{20}	10^{14}	5.7×10^{-8}	1.3×10^{-7}

The calculated value for C_R from ω_- is within a factor of two of the model value. Curiously the calculated value moves away from $10^{-7}cm^3s^{-1}$ as the steady state generation rate increases. It could be argued that the improvement to the linearisation approximation from the increased steady state density of trapped charge at higher excitation rates would cause the opposite effect. The calculated value for C_R from n_{ss} is also within a factor of two of the model value.

The same simulation procedure can be applied to the DOS profile which was used to obtain a match to TPC in the dark in the Stuttgart samples in §6.1. The results using the same model C_R, figure 7.8, do not match experiment very well. Nevertheless the values of C_R calculated as previously are presented in table 7.2 to gauge how well equation 7.15 applies to a non-exponential DOS.

Table7.2 C_R calculated using simulated data from DOS of figure 6.5(a). Actual model $C_R=10^{-7}cm^3s^{-1}$

G_{ss} $cm^{-3}s^{-1}$	δG cm^{-3}	C_R cm^3s^{-1} from ω_-	C_R cm^3s^{-1} from n_{ss}
10^{14}	10^{14}	8.3×10^{-8}	1.7×10^{-7}
10^{16}	10^{14}	9.6×10^{-8}	
10^{16}	10^{16}	9.6×10^{-8}	1.6×10^{-7}
10^{16}	10^{18}	1.2×10^{-7}	
10^{18}	10^{14}	2.3×10^{-7}	1.3×10^{-7}
10^{20}	10^{14}	5.0×10^{-7}	1.1×10^{-7}

Despite the density of states distribution no longer being a simple exponential, C_R calculated from ω_- is still within a factor of two of $10^{-7}cm^3s^{-1}$ at lower generation rates.

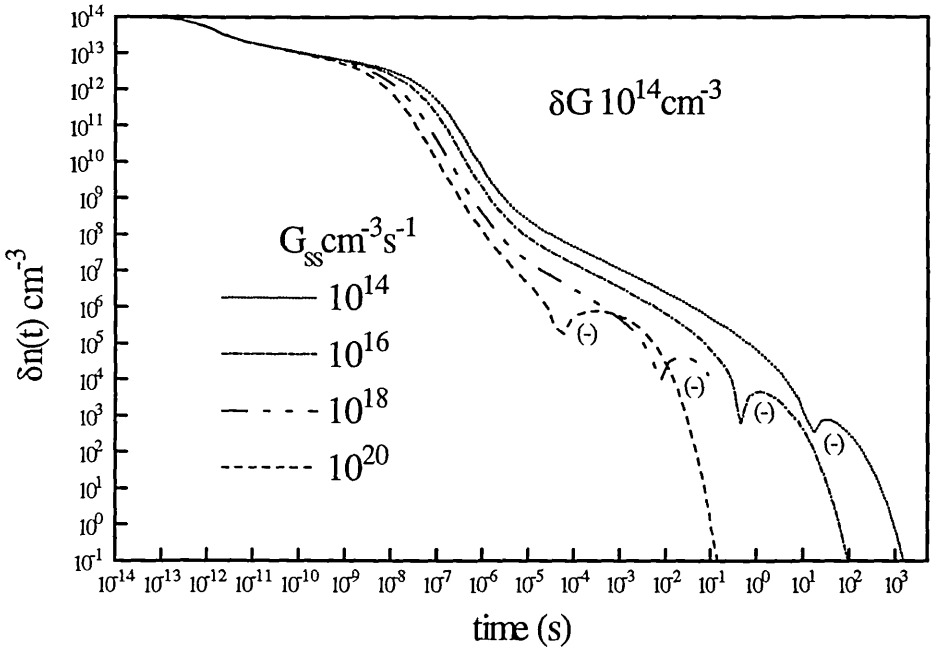

Figure 7.8 Simulated TPC with optical bias using the model DOS of figure 6.5(a) and $C_R=10C_n$.

Raising the initial transient photogeneration intensity, even to $10^{18}cm^{-3}$ which takes the transient behaviour well into the non-linear region, does not greatly affect the calculated value of C_R, while reducing it has no effect. Again C_R calculated from n_{ss} shows reasonable agreement with that used for the simulation.

7.5.2 Experiment

C_R calculated by the same methods for experimental data is presented in the table below. The free electron mobility μ_0 is taken to be $10cm^2(Vs)^{-1}$. N_t is estimated using the measured quasi-Fermi level shift and the density of states obtained from TPC in the dark with the Fourier transform technique treated as one electron states. There are a number of objections to estimating the density of recombination centres this way, for example the appropriate energy for occupation of the deep structure in the DOS distribution may not be the same as that for thermal release, but again the results are presented for purposes of comparison.

Table 7.3 C_R calculated from experimental data, Cambridge a-Si:H

G_{cc} $cm^{-3}s^{-1}$	δG cm^{-3}	C_R cm^3s^{-1} from ω_-	estimated N_{tcc} cm^{-3}	C_R cm^3s^{-1} from I_{cc}
3.2×10^{15}	10^{16}	no undershoot	7.6×10^{15}	8.2×10^{-9}
1.0×10^{17}	10^{16}	no undershoot	1.6×10^{16}	5.2×10^{-9}
2.3×10^{18}	10^{16}	1.6×10^{-8}	2.4×10^{16}	3.4×10^{-9}
3.4×10^{19}	10^{16}	7.2×10^{-9}	3.0×10^{16}	3.0×10^{-9}

Table 7.4 C_R calculated from experimental data, Stuttgart a-Si:H

G_{cc} $cm^{-3}s^{-1}$	δG cm^{-3}	C_R cm^3s^{-1} from ω_-	estimated N_{tcc} cm^{-3}	C_R cm^3s^{-1} from I_{cc}
1.0×10^{18}	10^{17}	no undershoot	2.4×10^{16}	1.9×10^{-9}
1.0×10^{18}	3.0×10^{17}	2.3×10^{-9}		
3.0×10^{18}	10^{17}	2.6×10^{-8}	2.6×10^{16}	2.1×10^{-9}
3.0×10^{19}	10^{17}	1.4×10^{-8}	2.8×10^{16}	2.4×10^{-9}
1.0×10^{20}	10^{17}	1.5×10^{-8}	2.9×10^{16}	2.8×10^{-9}

No firm conclusions can be drawn from the data above because of the degree of variation in the values for C_R. Most of the values for the recombination coefficient calculated from ω_- lie in the range 1 to $3\times10^{-8}cm^3s^{-1}$. This is consistent with a value for the trapping coefficient of around $10^{-8}cm^3s^{-1}$ if we are expecting $C_R>C_n$. Note that a higher δG of $10^{17}cm^{-3}$, in the non-linear response régime, is required to see undershoot in the Stuttgart material. The simulation suggests that using a high intensity does not necessarily affect the value of ω_-, although in table 7.4 it can be seen that increasing δG by a factor of three to $3.0\times10^{17}cm^{-3}$ causes ω_- to increase by a factor of 10. The values of N_{tss} estimated for both materials do not vary greatly, a factor of four for a four order increase in G_{ss} in the Cambridge material and a factor of 1.2 increase for a two order increase in G_{ss} in the Stuttgart material. Such a slow increase of the recombination centre density with increasing excitation is the mechanism invoked by Rose (see §1.7) to explain the observance of a sublinear power dependence of the steady state photocurrent on excitation intensity. The values of C_R calculated from ω_- are consistently larger than those from I_{SS}, implying that N_{tss} is being overestimated by a factor of five.

7.5.3 Alternative approach to investigating the undershoot behaviour

Equation 7.7 for the transient recombination rate offers another approach to investigating the behaviour of the undershoot. As has been pointed out when the first term on the rhs dominates recombination is quasi-monomolecular, later dominance of the second term allows δn to become negative. It is reasonable to attempt to identify some structure in the decay arising from the changeover in recombination behaviour. Such structure should be associated with the point at which

$$\delta n = \delta n^* = \frac{n_{ss}}{N_{tss}} \delta N_t \qquad (7.17)$$

Using a simplified analysis for an exponential tail, see appendix C, it is found that the thermalisation energy E^* for the time at which $\delta n = \delta n^*$ is independent of the initial photogeneration pulse intensity but is at a constant offset from the quasi-Fermi energy E_{fn}. For a tail parameter kT_c of 0.07eV at room temperature the offset varies between 0.03 eV for $C_R/C_n=1$ and 0.09eV for $C_R/C_n=10$.

The points δn^* satisfying equation 7.17 for simulation using the simple exponential conduction band tail are marked in figure 7.7(a). The time at which recombination begins can be seen from the time at which the decays depart from the pre-recombination $t^{-0.63}$ power law. However the change in slope of the decay is then gradual and continuous so it is difficult to point to anything which would allow δn^* to be located reliably for an arbitrary decay. Figures 7.1 and 7.9 show the positions on the decays exhibiting undershoot in the Cambridge and Stuttgart a-Si:H respectively of δn^* calculated using the estimates for the steady state density of trapped charge in tables 7.3 and 7.4. For the Cambridge material δn^* occurs near the time at which the current falls below the transient in the dark. There appears to be no such feature for the Stuttgart material.

7.6 Other features of TPC with optical bias

A notable feature of the decays of figure 7.1 measured in the Cambridge material which is not seen in the single electron DOS simulations is an enhancement of the transient current with optical bias over the transient current in the dark. The enhancement increases with increasing bias and is a factor of three for the highest bias of $3.4\times10^{19}cm^{-3}s^{-1}$. A similar enhancement can be seen with the Stuttgart material in figure 7.10 using a pulse excitation intensity in the linear response region. There is no comparable effect for the data of figure 7.9. The enhancement occurs between 10^{-7} and 10^{-5}s in the region where the TPC is controlled by trapping into deep defect states, so that the phenomenon appears to indicate a

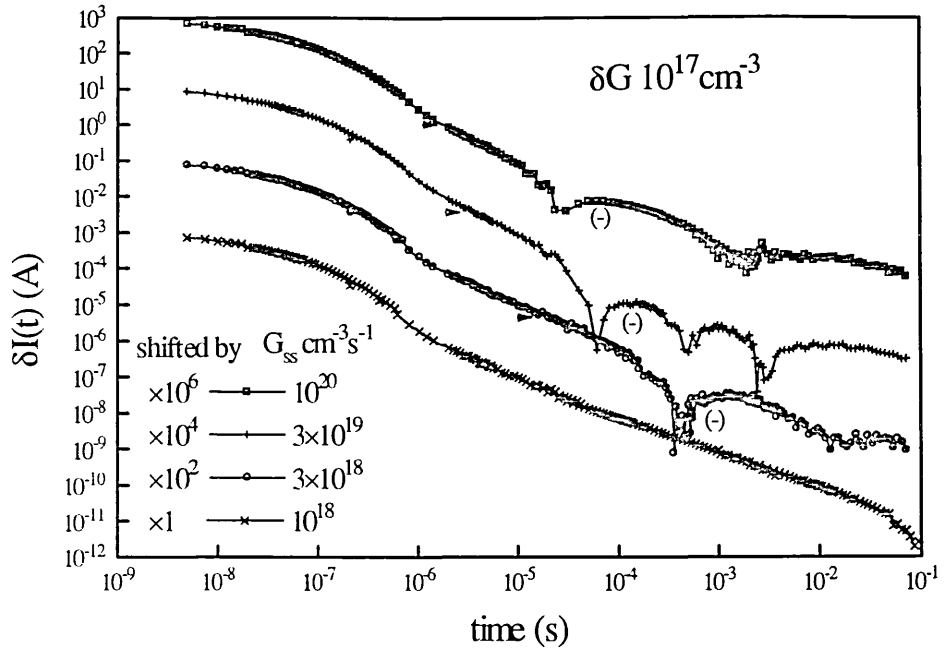

Figure 7.9 TPC with optical bias measured in the Stuttgart a-Si:H in the non-linear variation with pulse intensity régime. A (-) indicates portions of the decays which are negative. The decays have been shifted by the indicated factors for clarity. The bare arrowhead indicates the value of δn^*, see §7.53.

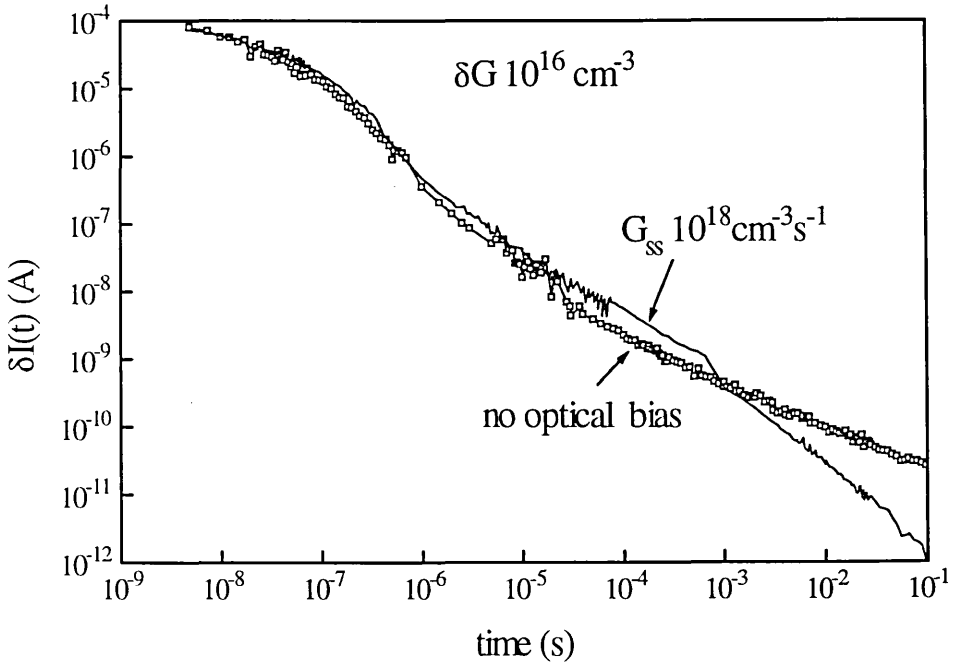

Figure 7.10 Enhancement of TPC by optical bias over TPC in the dark observed in the Stuttgart a-Si:H.

reduction in the number of deep states available for trapping. A decrease in the abundance of the deep trapping states because of the optical bias would have such an effect. However a more complex mechanism has been suggested recently (Han et al, 1993, Schiff et al, 1993) involving slow relaxation of occupied defects to deeper energies.

7.7 Summary

An undershoot or reversal of sign of transient photocurrent in the presence of optical bias is observed in samples of undoped amorphous silicon for large enough steady state generation rate. In the Cambridge material the undershoot is observed at a pulse generation density within the régime of linear TPC variation with pulse intensity ($10^{16}cm^{-3}$), whereas in the Stuttgart material the undershoot can only be observed by using a larger generation density. The time t_{us} at which the sign reversal occurs varies inversely with the steady state generation rate. An experiment performed on the Cambridge material in which G_{ss} is varied to maintain E_{fn} constant as the temperature is varied produces an activation energy for t_{us} of 0.36eV. After taking statistical shifts into account this energy is found to be inconsistent with the thermalisation energy $E_{us}=kTln(\upsilon t_{us})$ and therefore the hypothesis that undershoot occurs when E_c-E_{th} reaches an energy at a temperature independent offset from the quasi-Fermi level is rejected.

A theoretical analysis due to Pandya and Schiff (1985) of a linear with pulse intensity model for TPC in the presence of optical bias predicts an undershoot if recombination is bimolecular and the recombination coefficient $C_R>C_n$. The analysis further predicts that for an exponential tail the imaginary part of the Fourier transform of the transient decay also reverses sign at an angular frequency $\omega_-=n_{ss}C_R$. The Fourier transform spectra of the experimental decays are calculated and sign reversals in the imaginary part are indeed observed. Values for C_R obtained using the above relation from ω_- are mostly of a physically reasonable order of magnitude ($1\text{-}3\times10^{-8}cm^3s^{-1}$), despite the a-Si:H DOS not being a simple exponential and the TPC decays for the Stuttgart material being in the non-linear with intensity régime. However no firm conclusion is drawn on the recombination coefficient because of the degree of variation of the values for C_R. It is found that an undershoot can also be observed in simulated TPC by adopting capture coefficients that force recombination to occur via the path of capture of free electrons by trapped holes.

8.1 Experimental MPC results

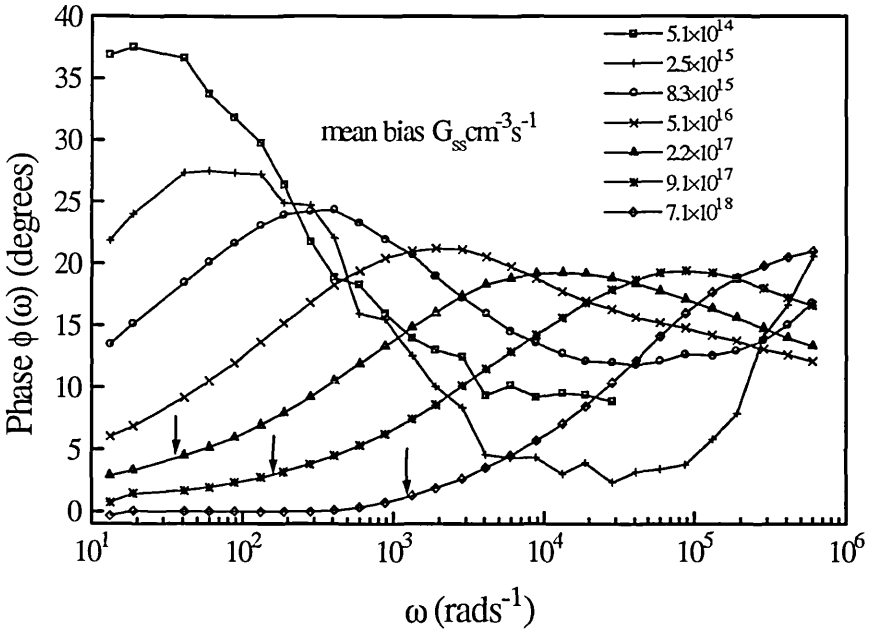

Figure 8.1 MPC phase shift spectra measured in the Stuttgart a-Si:H using 100% modulation. The position of ω_n for the higher generation rates is indicated by an arrow.

Figure 8.1 shows the MPC phase shift spectra measured in the Stuttgart a-Si:H using 100% modulation and average generation rate varying between $5.1\times10^{14}cm^{-3}s^{1}$ and $7.1\times10^{18}cm^{-3}s^{-1}$. Using 10% modulation produced no significant changes in the measured phase. Note that the lowest mean generation spectrum, having been measured using a larger gain than the others, is cut off at a lower frequency by the consequently reduced bandwidth of the amplifier. The position of the angular frequency $\omega_n = \nu\exp[-(E_c - E_{fn})/kT] = n_{ss}C_n$, for which the peak in the selection function W_B is at the quasi-Fermi level, see equations 3.8 and 3.10, is marked for each spectrum where it falls on the graph scale. It can be seen in the spectra that there is a distinct phase peak which moves to larger ω with increasing mean excitation. The large variation in the phase with mean generation rate at a particular frequency is unexpected because of the near invariance of the electron lifetime with generation rate. This point may be appreciated by reference to equation 3.11. At constant ω the only term on the rhs which can change with mean generation rate is τ_n. Equation 3.11 is only valid for $\omega \gg \omega_n$, but this condition is fulfilled for most of the data points in figure 8.1. The large variation in phase with G_{ss} casts doubt on the work of Schumm and Bauer (1989), who interpreted the phase shift as mapping the DOS of undoped a-Si:H directly. The angular frequency of the phase maximum ω_{peak} is plotted against ω_n in figure 8.2. A power law fit gives a superlinear relationship with an index of 1.23.

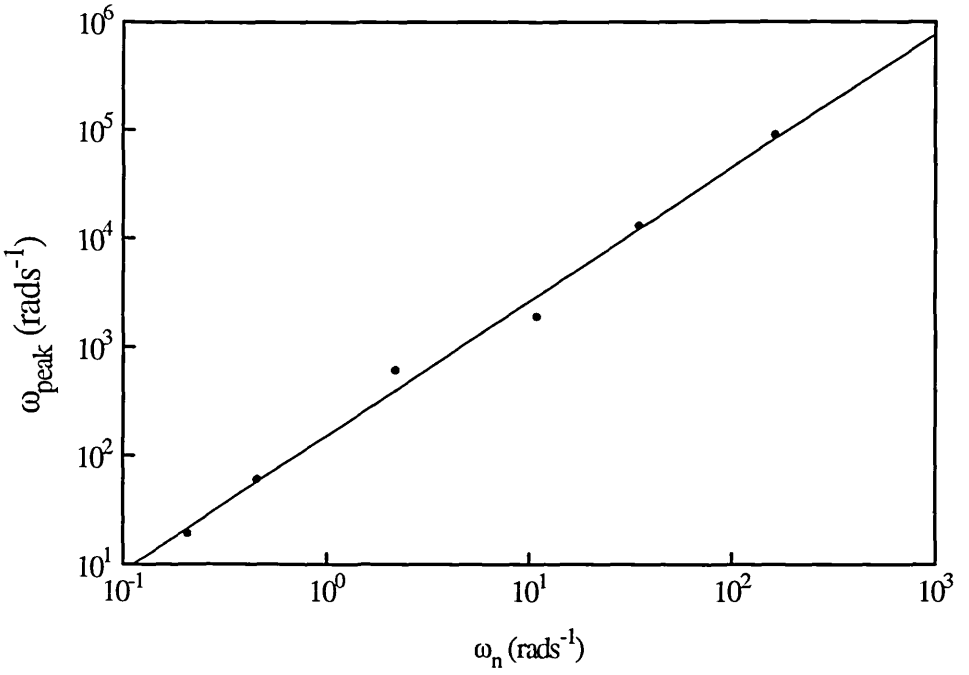

Figure 8.2 Angular frequency of the phase peaks of figure 8.1 plotted against ω_n.

Figure 8.3 shows the spectra of the A component of the complex photocurrent , as defined by equation 3.5. As expected (see §3.4.1) as ω decreases A approaches the values of $1/\tau_n$ calculated from the steady state photocurrent. Note that $1/\tau_n$ changes by only a factor of 3 for a 4 *order* change in the generation rate.

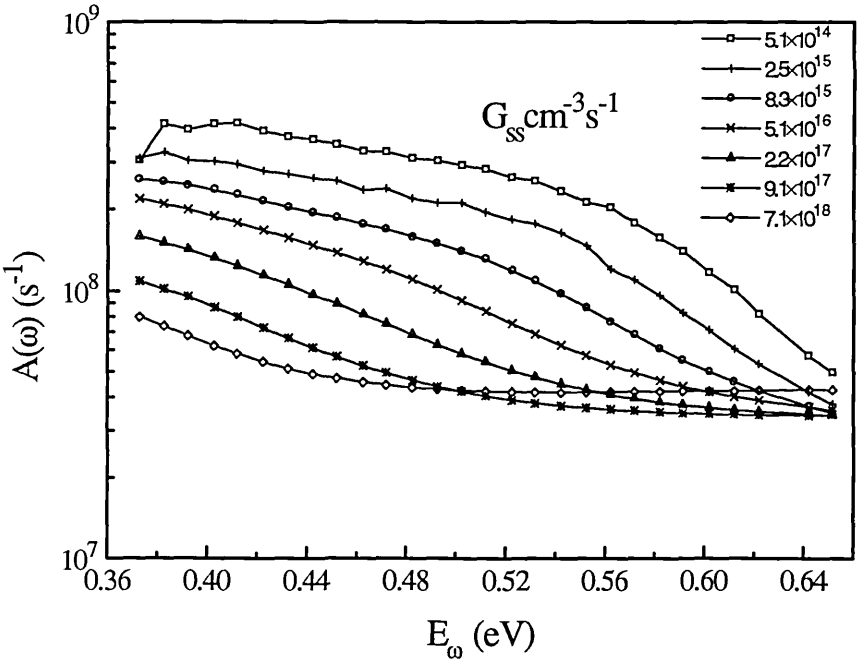

Figure 8.3 A component spectra corresponding to the phase spectra of figure 8.1. The value of $1/\tau_n$ calculated from I_{ss}, to which A is expected to tend at large E_ω, increases from $9.2\times10^6 s^{-1}$ at $G_{ss}=5.1\times10^{14}s^{-1}$ to $2.3\times10^7 s^{-1}$ at $G_{ss}=7.1\times10^{18}s^{-1}$.

Figure 8.4(a) is of the B component spectra presented as DOS plots by the use of equations 3.10 and 3.12. In most of the spectra at large E_ω (small ω) log(B) declines linearly with E_ω, although the highest intensity spectrum behaves anomalously. However the decline indicates a *sublinear* power law relationship between B and ω, rather than the linear relationship expected from equation 3.14. Table 8.1 presents values of the power law index β measured for the five intermediate intensity spectra together with the value of $g(E_{fn})$ calculated from the prefactor C (ie; where $B=C\omega^\beta$), assuming $C=kTg(E_{fn})/G_{ss}$ from equation 3.14.

Table 8.1 Values of parameters obtained by fitting $B=C\omega^\beta$ to the data of figure 8.4

G_{ss} $cm^{-3}s^{-1}$	β	$g(E_{fn})$ $cm^{-3}eV^{-1}$
2.5×10^{15}	0.43	5.2×10^{9}
8.3×10^{15}	0.43	1.0×10^{10}
5.1×10^{16}	0.44	2.6×10^{10}
2.2×10^{17}	0.42	4.3×10^{10}
9.1×10^{17}	0.45	1.1×10^{11}

A further discrepancy between the model prediction and the experimental observation is that the values for $g(E_{fn})$ in the table which were calculated assuming equation 3.14 to be correct are too small by some 6 orders of magnitude. The value of g(E) in mid-gap for good quality undoped a-Si:H is of the order of $10^{16}cm^{-3}eV^{-1}$ (Street, 1991a). However there is a qualitative agreement with the model behaviour in that the value of β is constant within experimental error, suggesting that the low frequency B is indeed independent of the shape of the DOS at E_ω.

The transition to the low frequency régime for each of the intermediate intensity spectra occurs at around the energy corresponding to the phase peak, $E_c-E_{\omega peak}$, rather than at E_{fn}. $E_{\omega peak}$ for the lowest generation rate is at the very edge of the experimental range. It might therefore be expected that the B spectrum calculated from the lowest generation rate data would represent the limiting curve to which the higher generation rate B spectra would tend for $E_\omega<E_{\omega peak}$. The spectra in figure 8.4(a) show some tendency to coalesce for small E_ω but the variation is greater than could be attributed simply to experimental uncertainty. Figure 8.4(b) compares the MPC DOS distributions with a distribution calculated from a TPC measurement without optical bias. The magnitude of the TPC DOS is commensurate with the MPC magnitudes for $E_\omega<E_{\omega peak}$. Note the very much wider range in energy accessible in a single time domain experiment, and that because no optical bias need be used the DOS can be probed to much deeper energies.

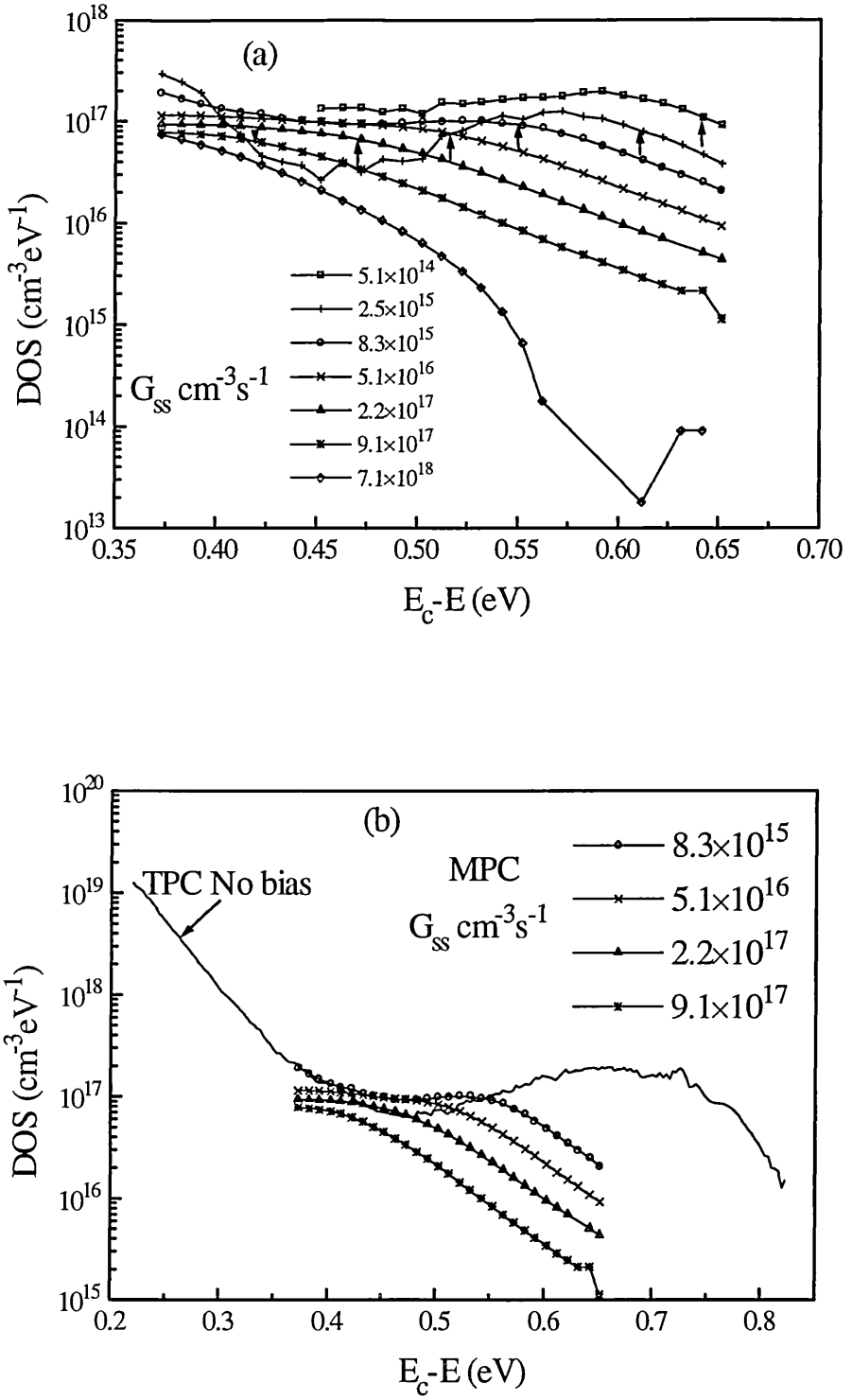

Figure 8.4 (a) Calculated DOS plots corresponding to the phase spectra of figure 8.1. The arrows indicate the position of E_c-$E_{\omega peak}$. (b) Intermediate generation rate DOS plots compared with the DOS calculated from TPC without optical bias ($\delta G=10^{16}cm^{-3}$).

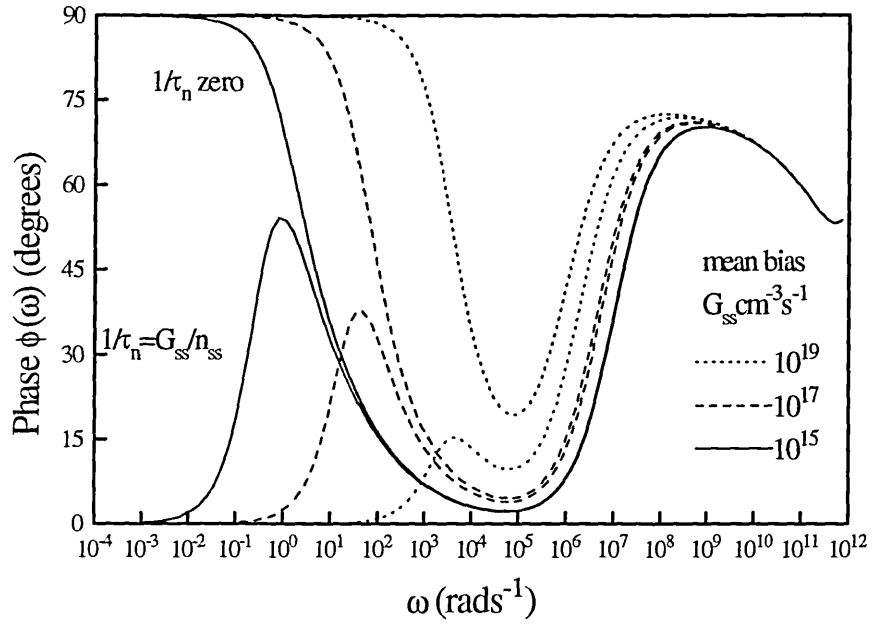

Figure 8.5 Phase spectra calculated from rate equations using the model DOS of figure 6.5(a), with $1/\tau_n$ equated to experimental values and to zero.

Insight into the experimental results can be gained by looking at the behaviour of spectra numerically computed using equations 3.5 to 3.7 and the model DOS of figure 6.5(a) constructed for the Stuttgart a-Si:H from TPC data. In figure 8.5 the values of τ_n and ω_n inserted to represent a given generation rate are calculated from the experimental steady state photocurrents. The basic qualitative experimental observation of a generation rate dependent phase peak is reproduced, but unlike experiment the phase peaks occur within a factor of two of ω_n. It is notable that the computed phase at values of ω many orders larger than ω_n is dependent on the generation rate.

The curves computed ignoring the $1/\tau_n$ term in equation 3.6 are included in the figure to demonstrate that the origin of the low frequency phase bump lies in the interplay between the effect of the occupation term on the weighted integrals over the DOS and that of the recombination term. The product (1-f)g(E) may be regarded as an *effective* DOS $g'(E,E_{fn})$. The weighting functions W_A and W_B, equations 3.8 and 3.9, act on this effective DOS which changes with generation rate. For ω sufficiently larger than ω_n the weighted integrals over g' are the same as for g. However as ω gets smaller the ratios $\int g'(E)W_A(E,\omega)dE/\int g(E)W_A(E,\omega)dE$ and $\int g'(E)W_B(E,\omega)dE/\int g(E)W_B(E,\omega)dE$ get smaller. The W_A ratio gets smaller faster than the ratio for the more energy selective W_B. Thus as ω gets smaller A gets smaller faster than B and the phase rises. Eventually the $1/\tau_n$ term in equation 3.6 causes A to become constant, but B continues to fall with decreasing ω. Thus the phase also falls, forming the observed phase bump.

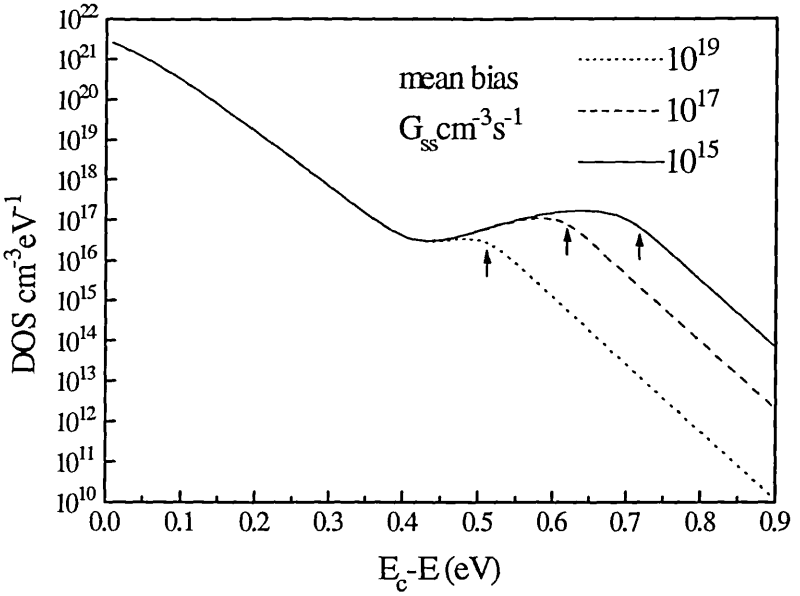

Figure 8.6 Recalculated DOS plots corresponding to the phase spectra of figure 8.5. The arrows indicate the position of E_c-E_{fn}.

The corresponding recalculated DOS distributions to the above spectra are presented in figure 8.6. It can be seen that unlike figure 8.4 for experimental data the shape of the DOS can be clearly identified as the limiting curve. The transitions to DOS independent behaviour for E_c-E_ω<E_{fn} are much sharper than on the experimental plots.

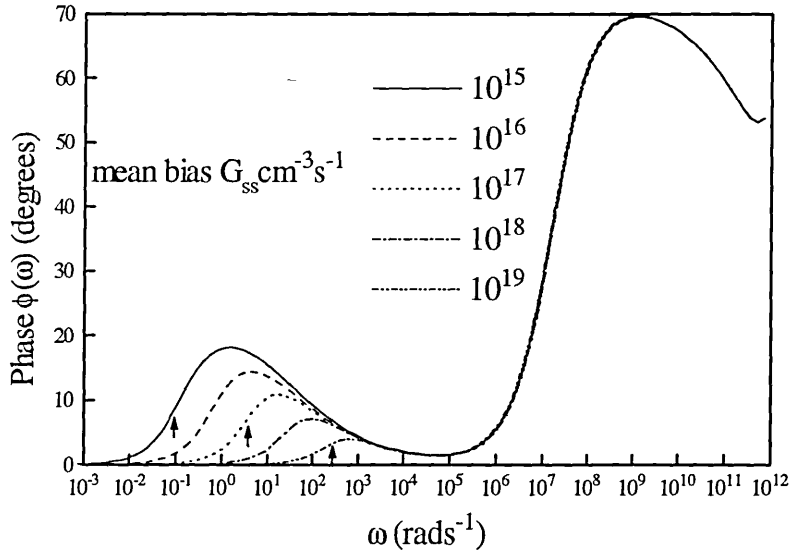

Figure 8.7 Phase spectra calculated from rate equations assuming the model DOS of figure 6.5(a) and $1/\tau_n$ a tenth of experimental values. The arrows show the position ofω_n.

The phase spectra of figure 8.7 were computed with values of free electron density at each generation rate a tenth of those used for figure 8.5, ie: with $1/\tau_n$ ten times larger. The effect has been to shift the phase peak frequencies to a factor of two to three greater than $1/\tau_n$, but at the expense of losing the overlapping behaviour in the phase spectra observed experimentally.

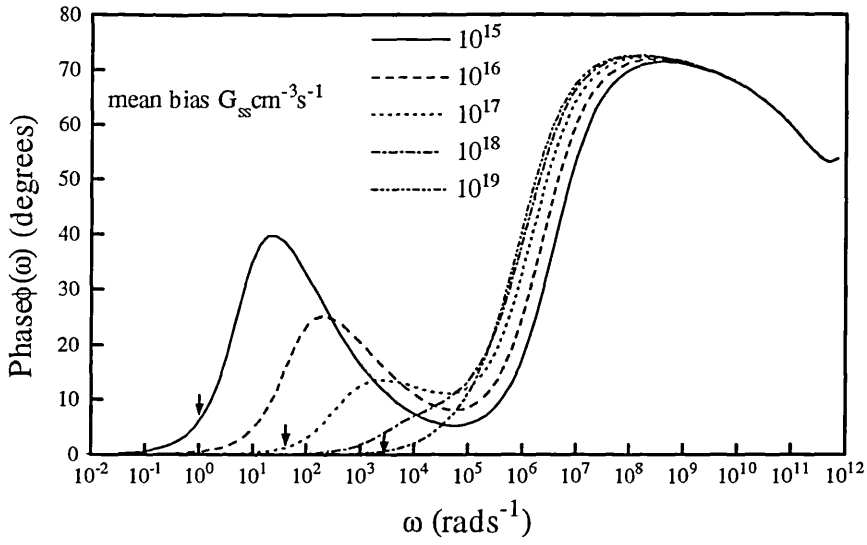

Figure 8.8 Phase spectra calculated from rate equations for a modified version of the model DOS of figure 6.5(a) in which the deep bump consists of a different species of states of capture coefficient $C_{n2}=10C_n$ (using experimental values of $1/\tau_n$). The arrows indicate the position of ω_n.

A possible interpretation of the occurrence of the experimental phase peak at a significantly higher frequency than ω_n is that the capture coefficient for deep states is larger than that for tail states. If the deep state capture coefficient is denoted C_{n2} then the phase peak might be expected to occur at a frequency $\omega_{n2}=n_{ss}C_{n2}$, since the peak of the weighting function W_B operating on the deep state distribution will be at an energy $E_c - E_{\omega 2} = E_c - kT\ln(\upsilon_2/\omega)$, $\upsilon_2=N_cC_{n2}$. Figure 8.8 shows the phase spectra computed for a modified version of the model DOS with $C_{n2}=10C_n$ and values of $1/\tau_n$ and ω_n as for figure 8.5. The phase peak has in fact been shifted to more than a factor of 10 greater than ω_n. The ratio ω_{peak}/ω_n also increases with G_{ss}, in agreement with experiment. The power law index is about 1.2. Unlike experiment however the phase peak vanishes for a G_{ss} of $10^{18}cm^{-3}s^{-1}$ and higher.

Figure 8.9 is of the DOS distributions recalculated using equation 3.12 and the tail state capture coefficient C_n. In order that the recalculated DOS should match the model DOS of figure 6.5(a) the DOS actually used in computing the phase spectra of figure 8.8 was modified to compensate for the effects on the spectra of the different value of the deep state capture coefficient. The modifications consisted of moving the peak of the deep state bump to E_c-(0.65+kTln(C_{n2}/C_n) and reducing the bump total density to $C_n/C_{n2}(4.4\times10^{16}cm^{-3})$. The transitions in the recalculated DOS distributions to the low frequency régime occurs at an energy around E_c-$E_{\omega peak}$ as with the experimental data. The transition is also more gradual than for the recalculated DOS distributions entailing just a single trap species, giving a qualitative similarity to the intermediate

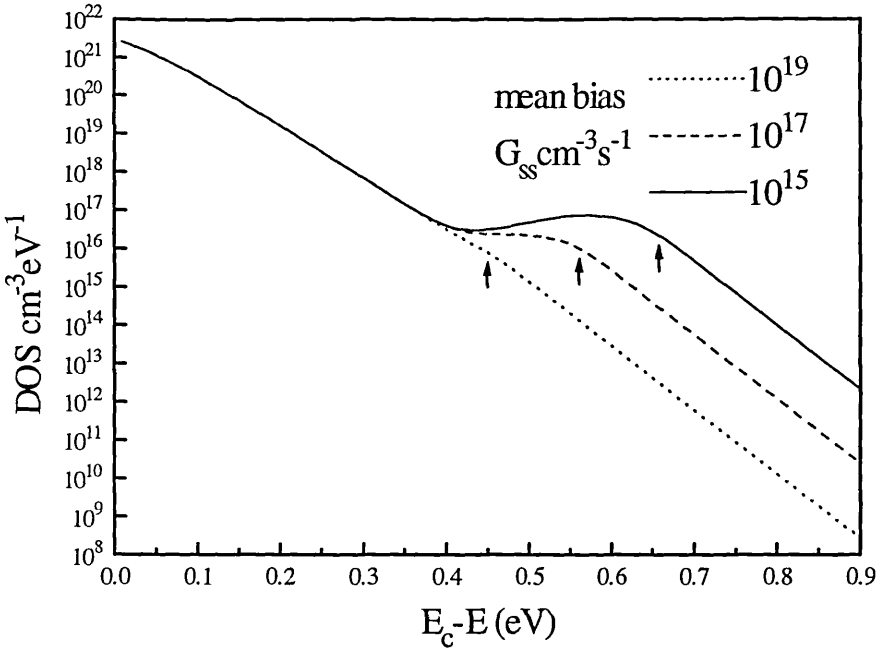

Figure 8.9 Recalculated DOS plots corresponding to the spectra of figure 8.8 using C_n as the scaling capture coefficient. The arrows indicate the position of ω_n.

generation rate experimental distributions in figure 8.4., ie: the four curves for $8.3\times10^{15}cm^{-3}s^{-1}\leq G_{ss}\leq 9.1\times10^{17}cm^{-3}s^{-1}$. Thus a partial match to experiment may be achieved using a capture coefficient for deep states between 10 to 100 times larger than that for tail states. Such a large capture coefficient suggests that the deep states may be charged centres, ie: are D^+. Schumm et al (1993) argue from LESR measurements that the density of charged dangling bonds in undoped a-Si:H is larger than the neutral density. Estimates from time of flight deep trapping $\mu\tau$ measurements give a value for the trapping coefficient for electrons of $2.7\times10^{-8}cm^3s^{-1}$ for D^0 states and $1.3\times10^{-7}cm^3s^{-1}$ for D^+ (Street, 1991b). A value of more than $10^{-7}cm^3s^{-1}$ for the deep trapping capture coefficient is in contradiction to the value of $1\text{-}3\times10^{-8}cm^3s^{-1}$ for the states controlling recombination obtained in chapter 7 from TPC with optical bias measurements.

The above computations have ignored holes, which might be expected to have an influence at low frequencies when the states controlling the material response are deep enough for exchange rates with the valence band to be significant. Figure 8.10 compares the phase spectra computed using the Hattori solution in appendix B for the full electron-hole rate equations and the same DOS and values of ω_n as for figure 8.5, with the spectra of figure 8.5. In the treatment taking account of holes it is not possible to specify τ_n directly, but τ_n can be controlled *indirectly* by specifying the ratio ω_n/ω_p, its value being determined from the low frequency asymptote of A. The spectra in the figure were computed using $\omega_n/\omega_p=10$, giving τ_n within 10% of experiment. The two sets of spectra are broadly similar, in particular the phase peak frequencies are within a factor of three of each other.

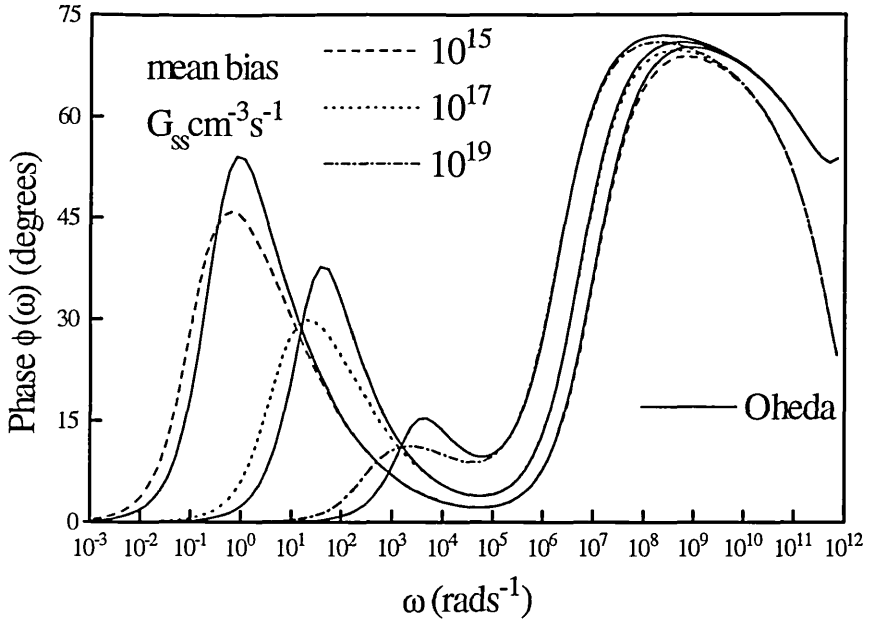

Figure 8.10 Phase spectra calculated from the rate equations including hole transitions explicitly, compared with the spectra including hole transitions only through a recombination term (Oheda). The DOS assumed is that of figure 6.5(a).

Finally it should be noted that the treatment taking account of hole transitions, in common with the treatment ignoring them, predicts $B \propto \omega$ at small ω in contradiction to the experimental observation.

8.3 Comparison of MPC with Fourier transformed TPC spectra.

An obvious test of the validity of the validity of the Fourier transform procedure of chapter 5 is to compare the spectra obtained from the calculated Fourier transform of TPC decays in the linear response régime with MPC spectra measured under equivalent conditions. As has been pointed out in §4.1 from the point of view of linear systems theory the mean generation rate alters the system response. Thus equivalent conditions between TPC and MPC experiments means that the steady state generation rate in the TPC experiment must be the same as the mean generation rate in MPC. and that the initial photogenerated transient free electron density in TPC δG cm^{-3} should be equal to the numerical value of the MPC complex generation rate amplitude G_ω cm^{-3}s^{-1}. The apparent discrepancy in the unit dimensions is taken care of by the Fourier transform formalism, which specifies which unit of time measurement is being used.

Figure 8.11 compares the phase spectra obtained by direct simulation of MPC with 100% modulation index and the phase spectra of the Fourier transform of simulated TPC decays with equivalent conditions, using the model DOS of figure 6.5(a). For $\delta G = 10^{15}$cm^{-3} where the model response is linear the match is almost exact, as expected. At $\delta G = 10^{17}$cm^{-3}, in the non-linear TPC response régime the spectra do not match, again

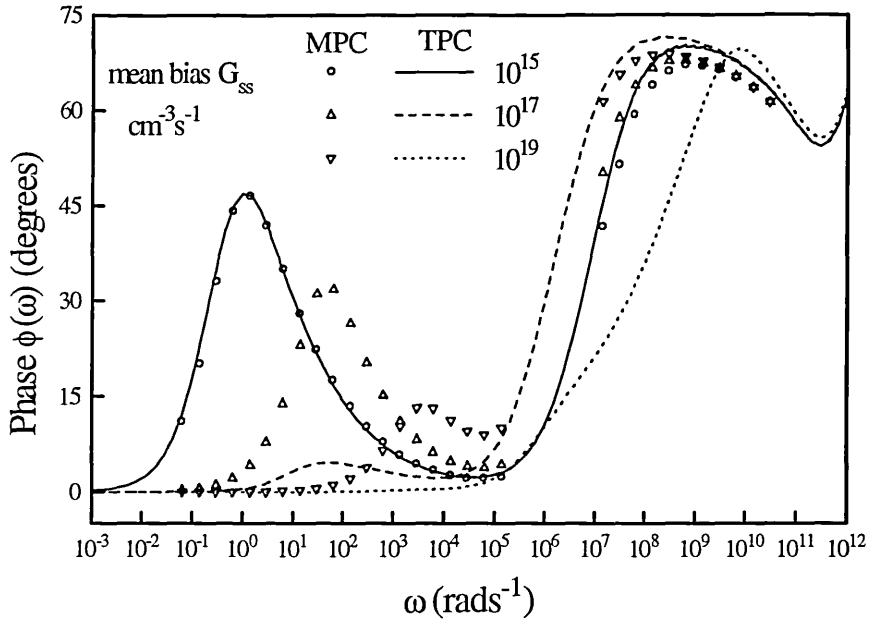

Figure 8.11 Comparison of Fourier transform of simulated TPC with optical bias phase spectra with directly simulated MPC (100% modulation) phase spectra for the model DOS of figure 6.5(a). The values of δG for TPC are numerically equal (cm^{-3}) to G_{ss}($cm^{-3}s^{-1}$).

as expected. The effect of non-linearity on the Fourier transform spectrum appears to be to simply depress the low frequency phase, so that there is still a low frequency bump with the same peak frequency as the corresponding MPC phase bump.

Figure 8.12 demonstrates that the simulated MPC phase spectra also match the computed spectra of figure 8.5, the simulation steady state free electron densities being close to the experimental values used in computing figure 8.5. The match is of interest because of the disparity between the simulation capture coefficients adopted to produce the figure and those used to produce the undershoot in simulated TPC, see §7.5.1. As before C_p for the conduction band tail is set to zero, mimicking the assumption implicit in the derivation of equations 3.5 to 3.7 that hole capture by states above midgap can be ignored. However C_p for the valence band tail is set to $C_n/10$, by contrast in order to observe the undershoot it was necessary make the valence band C_p to be more than C_n (admittedly this is unrealistic).

Figure 8.13 compares the experimental MPC phase spectra with 100% modulation index and the phase spectra of the Fourier transform of TPC decays measured under equivalent conditions. The Fourier transforms were calculated without using an apodisation function on the transient decay data. The match between the lowest generation density $\delta G=2.5\times10^{15}cm^{-3}$ TPC transform spectrum, the only one in the linear response régime of the material, and the corresponding MPC spectrum, is not as good as might be hoped. The Fourier transform phase spectrum is probably more sensitive to the long time non-linearity in the TPC decay than the calculated DOS. At higher generation

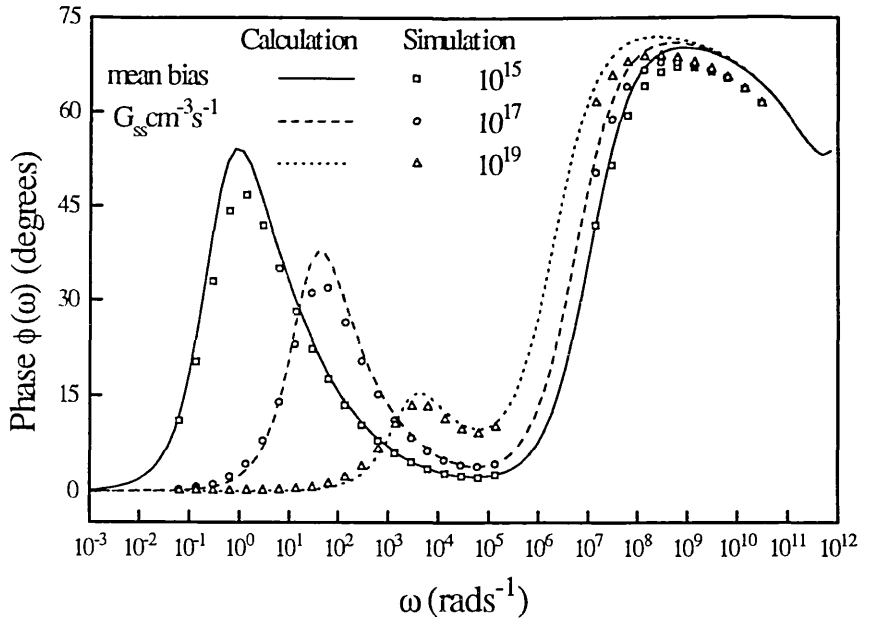

Figure 8.12 Comparison of MPC spectra calculated using rate equations, and simulated, assuming the model DOS of figure 6.5(a). Note that the simulation values of n_{ss} (and hence $1/\tau_n$) are close to the experimental values used for the calculation.

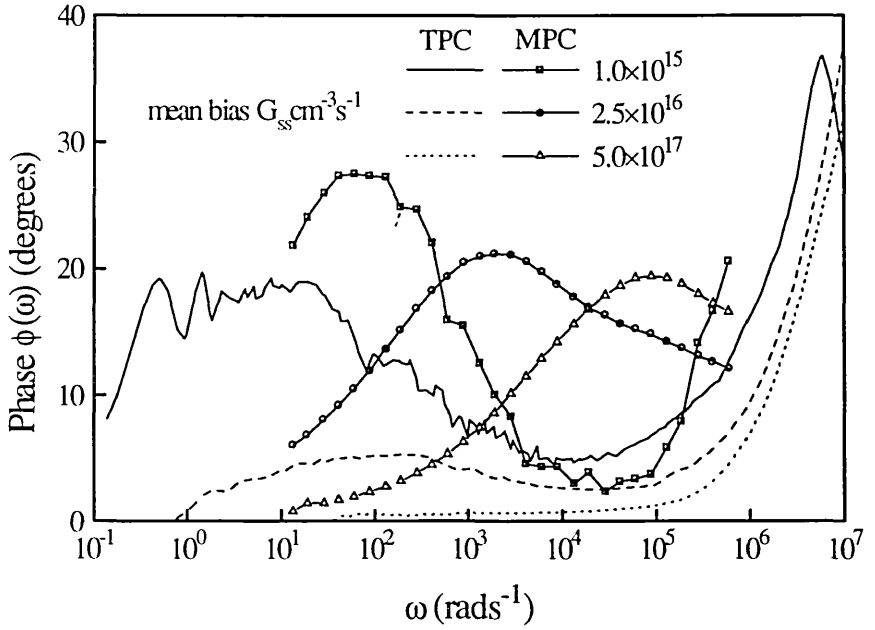

Figure 8.13 Comparison of experimental Fourier transform of TPC measured with optical bias phase spectra and MPC (100% modulation) phase spectra for the Stuttgart a-Si:H. The values of δG for TPC are numerically equal (cm^{-3}) to $G_{ss}(cm^{-3}s^{-1})$.

density the Fourier transform of TPC spectrum appears to be exhibiting the same behaviour observed in the simulation model. However the phase bump peak frequency for the $\delta G=5.1\times10^{16}cm^{-3}$ TPC transform spectrum corresponds more closely to that for the $G_{\omega}=2.5\times10^{15}cm^{-3}s^{-1}$ than to the $\delta G=2.51\times10^{16}cm^{-3}s^{-1}$ MPC spectrum. This suggests that the steady state generation rate calibration for one or other of the MPC or TPC experimental systems may be incorrect, so that n_{ss} is different by a factor of ten for nominally the same generation rate. It has been checked that nominally the same generation rate produces the same photocurrent in the sample for both systems. Therefore the likeliest source for such an error would be a different sample electrode illumination length. However this could account for a discrepancy in n_{ss} of a factor of two at the maximum.

8.4 Summary

MPC measurements on undoped a-Si:H exhibit a peak in the phase spectrum which moves to higher frequency with increasing mean generation rate G_{ss}. Spectra computed from the solution to the MPC rate equations derived by Oheda (1981), assuming the DOS calculated for the Stuttgart a-Si:H in chapter 6 and experimental values of recombination time, show a phase peak having a peak angular frequency ω_{peak} close to the frequency associated with the quasi-Fermi level $\omega_n=v\exp(-(E_c-E_{fn})/kT)$. By contrast the experimental spectra have ω_{peak} two orders larger than ω_n for G_{ss} around $10^{14}cm^{-3}s^{-1}$ moving to almost three orders larger for G_{ss} around $10^{19}cm^{-3}s^{-1}$. In addition it can be shown from the Oheda equations that for $\omega<<\omega_n$ the function $B(\omega)$ (equation 3.7) is independent of the DOS at E_w and that $B=C\omega$, where $C=kTg(E_{fn})/G_{ss}$. It can also be shown that $B\propto\omega$ when $\omega<<\omega_n$ for a fuller treatment solving rate equations which include hole transitions explicitly (Hattori et al, 1994). The experimental B spectra do show DOS independent behaviour for $\omega<<\omega_{peak}$, but fitting to a relation $B=C\omega^{\beta}$ produces $\beta=0.43\pm0.02$ and C around six orders smaller than $kTg(E_{fn})/G_{ss}$.

Spectra computed using an extension of the Oheda analysis to cover a DOS in which the Stuttgart material deep bump is a set of states having a larger trapping coefficient than the tail states replicate the behaviour of ω_{peak} being larger than ω_n. It is estimated however that a capture coefficient for the deep states 10-100 times larger than that for the tail states is required to give the observed ratio of ω_{peak} and ω_n. A value for the trapping coefficient of dangling bonds of more than $10^{-7}cm^3s^{-1}$ is larger than the value for states controlling recombination of $1\text{-}3\times10^{-8}cm^3s^{-1}$ obtained from time domain measurements with optical bias in chapter 7. The computed spectra using the above extension to the Oheda analysis still show $B\propto\omega$ at small ω in contradiction to experiment.

The DOS calculated from the MPC measurements is of the same magnitude as that calculated from TPC without optical bias. The advantage of calculating the DOS

from TPC data is seen from the wider range in energy accessible in a single measurement and the ability to probe deep states because no optical bias need be used. The match between an MPC phase spectrum and the phase spectrum of the calculated Fourier transform of a TPC decay measured with δG in the linear response régime and equal mean generation rate is not very good. The match for the equivalent *simulated* experiment is almost exact.

9.1 Transient Photocurrent measurements

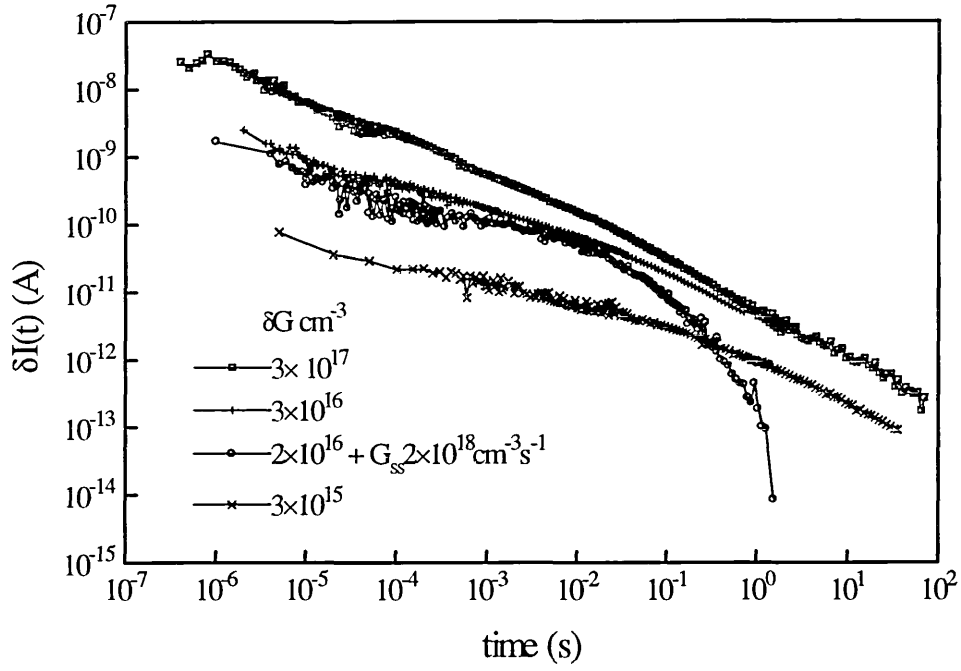

Figure 9.1 TPC decays with and without optical bias measured in a-As_2Se_3.

Figure 9.1 shows transient photodecays measured in a-As_2Se_3 with different pulse intensities. The time range covered is smaller than for a-Si:H because even at the highest intensity the magnitude of the As_2Se_3 transient photocurrent is too small to allow it to be detected at times shorter than 10^{-7}s. The decay shapes show some dependence on the pulse intensity, particularly at long times, though not as pronounced as for silicon at the same intensities. Holes are the majority carrier in the material, so the nearly featureless power law decays can be interpreted as arising from a featureless exponential *valence* band tail, of slope $kT_v \approx 0.06$eV over a range in energy above E_V of 0.3 to 0.7 eV, assuming $\nu = 10^{12}$Hz. However, the photocurrent expected for such a band tail extending to the mobility edge, calculated using equation 2.4 is two to three orders higher than that experimentally observed.

Another observation to be accounted for comes from the interpretation of steady state photocurrent measurements. Figure 9.2 plots the steady state photocurrent versus inverse temperature at a constant generation rate. The high (room) temperature region in which recombination is bimolecular has an activation energy of 0.33eV. Analysis (Adriaenssens et al, 1985, Main and Owen, 1972) based on recombination occurring through a set of defect states places the set centre energy at twice this measured activation energy above the valence band mobility edge, in this case 0.66eV. A set of recombination states at this energy should affect TPC over the observed time range. As has been seen with a-Si:H in chapter 6 a featureless power law decay can arise from a

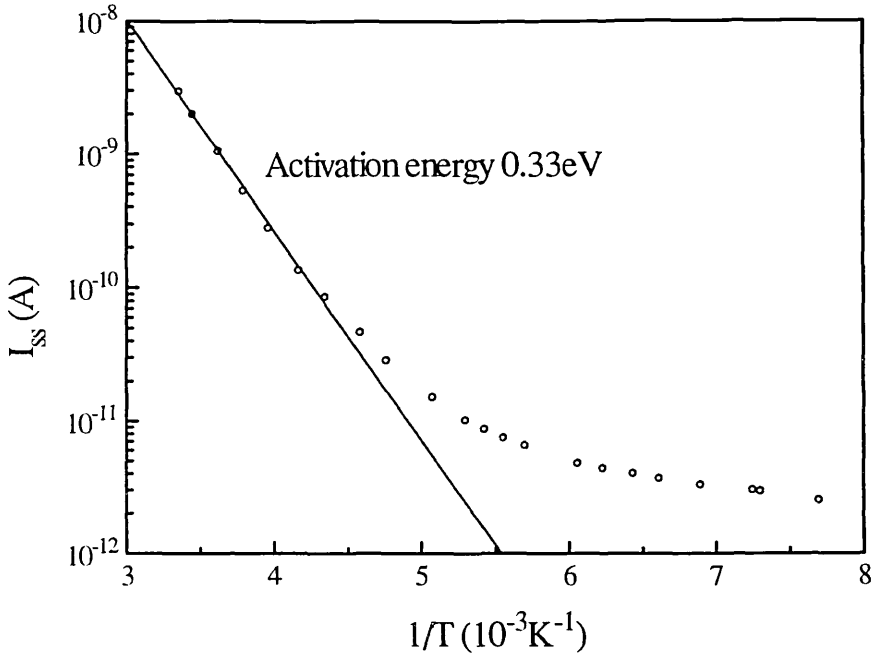

Figure 9.2 Steady state photocurrent at constant G_{ss} versus inverse temperature in a-As_2Se_3 (Webb, 1990).

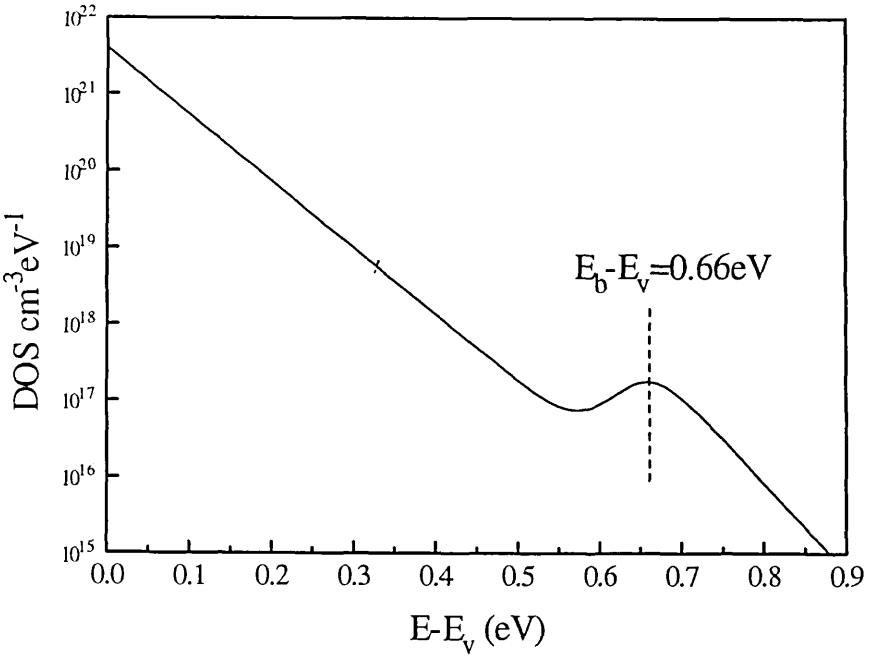

Figure 9.3 Model DOS for a-As_2Se_3 consisting of a 0.05eV tail and a deep bump of density $2\times10^{16}cm^{-3}$ at 0.66eV above E_v.

density of states with significant structure. It is possible to postulate a similar physically reasonable DOS for a-As_2Se_3, illustrated in figure 9.3, which explains both the transient and steady state observations. The deep energy bump consisting of the recombination mediating states has a peak situated at 0.66eV as required by the steady state interpretation. The bump states total density is $2\times10^{16}cm^{-3}$, with a capture probability 30 times larger than for neutral tail states. Figure 9.4 shows a simulation of TPC using the DOS. The total trapping probability into the bump is large enough that the deep trapping signature in the decay occurs before $10^{-6}s$, so that over the experimental time region only a power law is seen. Unfortunately this postulated DOS is not supported by MPC results, as is discussed below.

9.2 Modulated Photocurrent measurements

Figure 9.5 shows the MPC phase response of the sample for three different illumination levels with 100% modulation index (Webb 1990). The Fourier transform phase spectrum of the TPC decay with optical bias of figure 9.1 is superimposed, the steady state generation rate of which is close to that of the lowest intensity MPC measurement. The strong dependence of the MPC phase on the mean generation rate seen in the figure at low frequency is expected because of the bimolecular recombination kinetics in the material in this photoconductivity regime. Unlike the a-Si:H measurements of chapter 8 the free recombination time varies strongly with illumination, so in equation 3.11 at low frequency the denominator varies more strongly with generation rate than at high frequency when the integral over states term is much larger.

The TPC Fourier transform and MPC phase spectra do not match very well, which is unsurprising in view of likely distortions due to the missing short time contribution. However the calculated DOS distributions from TPC and MPC, figure 9.6, do match. The DOS calculated from the TPC with optical bias data of figure 9.1 is close to the MPC DOS, which if the MPC DOS is correct indicates that the short time transient current is not greatly above a continuation of the observed power law. Neither of the calculated state distributions, in particular the MPC DOS which is unaffected by bandwidth problems over the measured frequency range, show any sign of a large bump at 0.66eV. The question arises whether the same effect as has been observed in chapter 8 is affecting MPC here, ie; do the phase peaks indicate a transition from DOS dependent to DOS *independent* behaviour below the phase peak frequency. If so MPC measurements made at a smaller mean generation rate may yet reveal some structure in the DOS. Extrapolation of the DOS distributions of figure 9.6 to the valence band mobility edge yields a value for the effective mobility edge DOS several orders higher than the expected $10^{20}cm^{-3}$, in agreement with the observation that the measured transient photocurrent is several orders *smaller* than that expected for an exponential tail extending to the mobility edge.

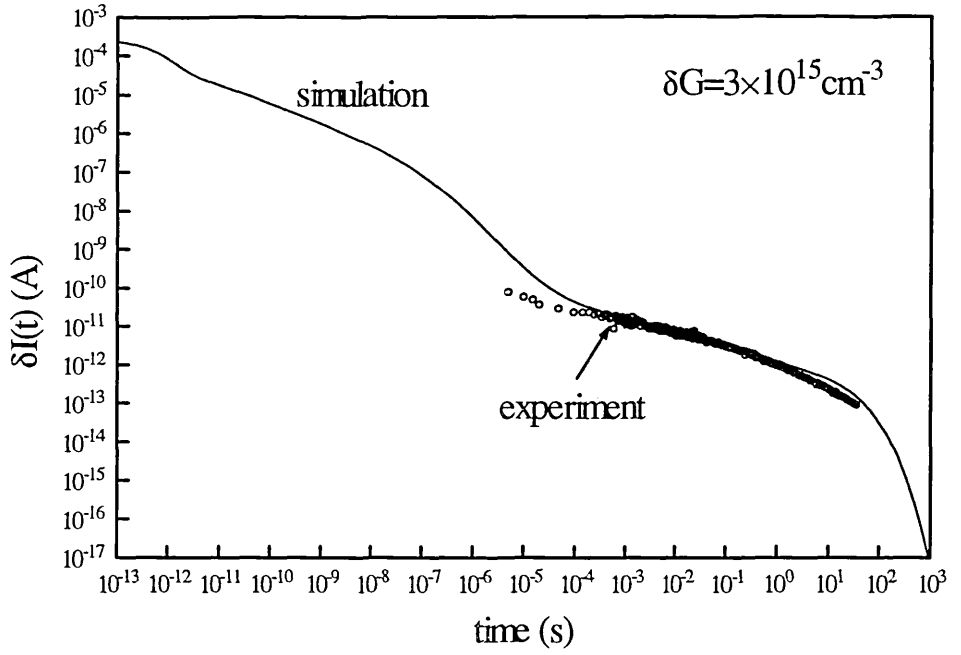

Figure 9.4 Simulated TPC using the model DOS of figure 9.3. The decay has been scaled using $\nu=10^{12}$Hz and $\mu=1cm^2(Vs)^{-1}$.

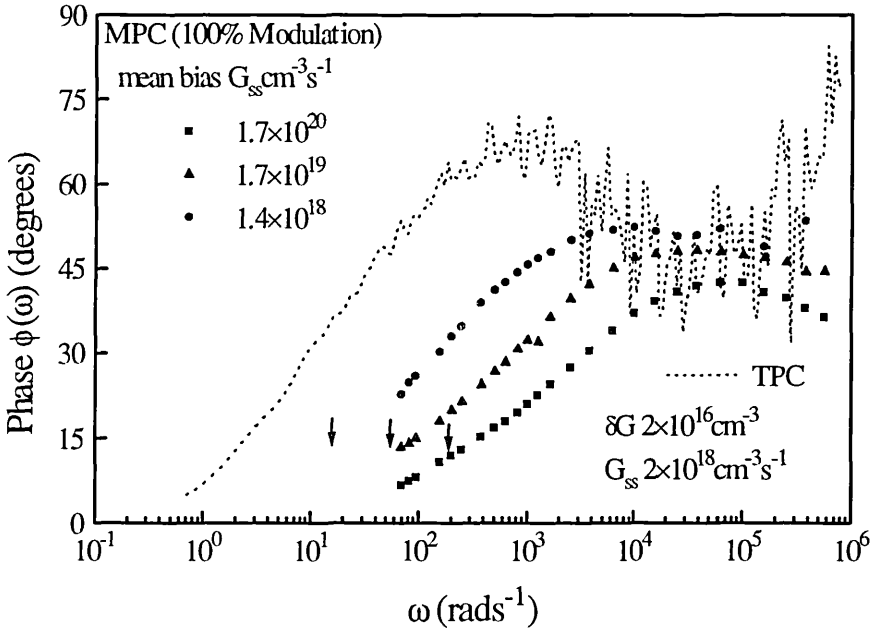

Figure 9.5 MPC phase spectra measured on a-As_2Se_3 (Webb, 1990), together with a TPC with optical bias Fourier transform spectrum. The arorws indicate the position of ω_n for the MPC spectra.

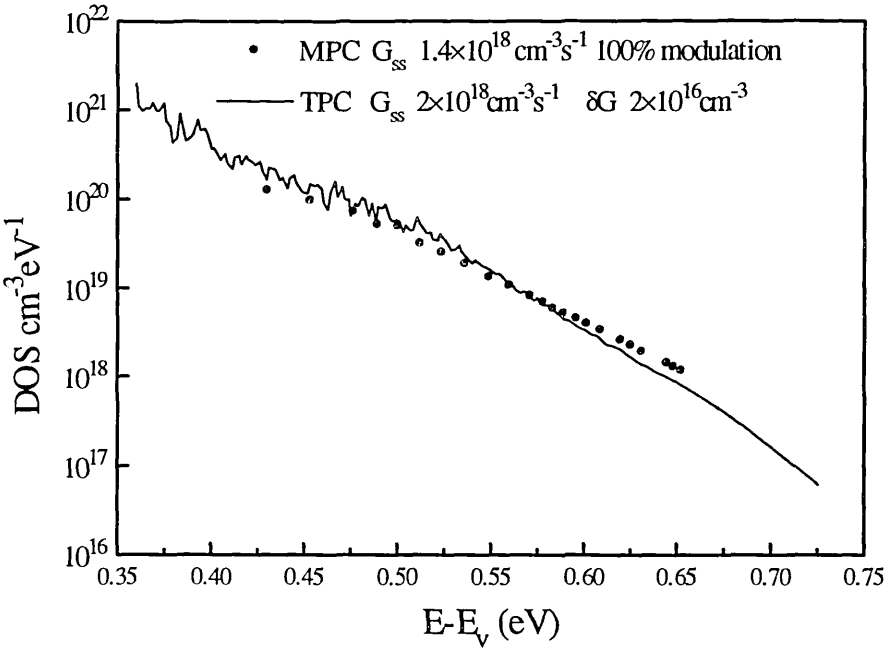

Figure 9.6 DOS calculated from TPC and MPC measurements on a-As_2Se_3.

9.3 Summary

To sum up the interpretation of steady state data that places a large density of recombination states at 0.66eV above E_v is not supported by MPC measurements. Nevertheless both the MPC calculated DOS and the magnitude of TPC indicate that the valence band tail does not consist simply of a featureless exponential tail extending from the mobility edge to 0.7 eV, in fact the density of states from MPC is two orders *greater* in magnitude over the probed range than this. It is suggested that the observed peaks in the MPC phase spectra may indicate a transition to DOS independent behaviour at low frequency, similarly to a-Si:H. MPC at lower G_{ss} may therefore reveal some structure in the DOS.

Chapter 10 Summary and conclusions

The unifying theme of this work is the complementary use of both the time and the frequency domain in investigating the density of states of and associated trapping and recombination processes in amorphous semiconductors by making photoconductivity measurements. In particular it is pointed out that while analysis of the photoconduction rate equations in the multiple trapping model is simplest in the frequency domain, experimentally a wider range in energy of the DOS can be probed by the time domain transient photocurrent (TPC) experiment. As a means of applying frequency domain analysis to time domain data in chapter 4 a method of calculating the Fourier transform of transient photocurrent decays is introduced and tested. Standard FFT algorithms are not suitable because of the many orders in time and magnitude covered by a typical TPC decay. The Fourier transformation of TPC data, measured at low enough pulse photogeneration density δG that the variation with δG is linear (the linear régime), is combined with a suitably modified form of a DOS calculation method devised for the frequency domain modulated photocurrent (MPC) experiment. The result is a novel, wide energy range, accurate probe for the DOS of a semiconductor, valid for both distributed and single levels of states.

In chapter 6 this probe is applied to TPC measurements in the linear régime at varying temperature on undoped a-Si:H from different sources. The DOS calculated consists of a 0.03eV exponential tail at shallow energy and a bump of $4.4\times10^{16}cm^{-3}$ states at 0.65eV below E_c. Such a DOS is consistent with the generally accepted model for undoped a-Si:H, which would attribute the bump to dangling bond defect states. An important observation is the ability of the Fourier transform-TPC method to detect the presence of this structure despite the TPC decay being featureless at the time (0.08s) at which charge deeply trapped in the bump states is released. The accuracy of the calculated DOS is found to depend crucially on the size of the missing contribution to the Fourier transform integrals from the TPC at times shorter than the minimum observed. In the case of the measurements presented in the chapter it is argued that the size of this contribution is small and therefore the calculated DOS accurate.

Self consistency within the multiple-trapping model is shown by using the calculated DOS, together with the estimates of the trapping coefficients used to calculate the DOS, as input parameters to a computer simulation. The simulation reproduces by numerical solution of the multiple-trapping rate equations the observed time dependence and scaling of the transient photodecay. The simulation does not produce a quantitative fit to TPC measurements in the high pulse intensity ($\delta G>10^{16}cm^{-3}$), non-linear response régime. However qualitatively similar behaviour is seen in the simulation, in particular sublinear variation with δG at short times and almost complete insensitivity to δG at long times. These phenomena are attributed to the high intensity decays being controlled at short times by recombination through some other path than *via* the fixed density of

dangling bonds, and at long times by emptying out and recombination of charge trapped in deep states which have been filled to an intensity independent occupation.

Chapters 7 and 8 report on the photoconductive response of undoped amorphous silicon exposed to optical bias in the time and frequency domains. The TPC with optical bias measurements of chapter 7 exhibit an *undershoot* or sign reversal of TPC for G_{ss} larger than about $10^{18}cm^{-3}s^{-1}$, apparently previously unreported in a-Si:H. The undershoot time t_{us} varies inversely and sublinearly with G_{ss}. An experiment in which E_{Fn} is held constant as temperature is varied yielded an activation energy of 0.36eV for t_{us} but an attempt to link this activation energy to the quasi-Fermi energy fails. The undershoot is predicted by an analysis based on the frequency domain solution to the linearised multiple trapping rate equations, for the conditions that (a); the recombination mechanism is bimolecular, and (b); that the recombination coefficient C_R is larger than the trapping coefficient C_n. The analysis further predicts for an exponential tail a sign reversal in the imaginary part of the frequency domain photo-response at a frequency $\omega_- = n_{ss}C_R$. The imaginary part of the Fourier transform spectra calculated for the experimental TPC decays exhibiting undershoot does indeed show such a sign reversal, from which values of C_R mostly but not exclusively in the range $1\text{-}3\times10^{-8}cm^3s^{-1}$ are calculated. It is found possible also to obtain an undershoot in *numerical simulations* of TPC by constraining recombination to occur via the path of free electron capture by trapped holes.

The MPC measurements of chapter 8, which sample the frequency domain photoconductive response directly, have optical bias unavoidably present. The DOS distributions calculated from the spectra at shallow energy/high frequency match the DOS calculated from TPC data. At low frequency the MPC signal is independent of the shape of the DOS. Therefore in making MPC measurements the mean generation rate must be reduced as much as possible, at the cost of reducing the signal magnitude, in order to probe as much of the DOS as possible. TPC measurements by contrast may be made with no optical bias at all - allowing deep states to be probed.

Experimentally the transition from DOS dependent to DOS independent behaviour in the a-Si:H is accompanied by a phase peak observed to occur at $100\times n_{ss}C_n$ and upwards, varying superlinearly with ω_n. Such a transition is described by the frequency domain solution to the linearised multiple trapping equations, occurring in a model for a single species of traps at the lower frequency $\omega_n=n_{ss}C_n$. A modification to the model assigning a larger capture coefficient $C_{n2}=10\text{-}100\times C_n$ to deep states can give a phase peak at $100\omega_n$. However the low frequency "B" (unscaled DOS) spectrum is predicted to be proportional to ω, whereas the experimentally observed variation is $\omega^{0.43}$. The solution to the multiple trapping rate equations which include hole transitions explicitly also predicts $B\propto\omega$.

In chapter 9 the experience gained from the time and frequency domain studies on a-Si:H are used to try and shed light on a problem posed by the interpretation of

steady state photoconductivity measurements on a-As_2Se_3, viz. the placing of a set of recombination states at 0.66eV above E_V from which no emission feature is seen in TPC decays. The featureless power law TPC decays have previously been interpreted as indicating a featureless exponential tail. A DOS similar to that calculated for undoped a-Si:H with a bump at 0.66eV is proposed to explain the discrepancy. Although the DOS calculated from MPC measurements shows no feature at 0.66eV, the question is raised whether this is because the MPC response is in the DOS independent régime, again similarly to a-Si:H. The DOS calculated from TPC measurements cannot be relied on because the signal magnitude is too small to allow times shorter than 10^{-7}s to be observed. However it can be said that the TPC magnitude is two to three orders too small to indicate an exponential tail extending to the band edge.

Further work

The major contribution to the field arising from this work is a new tool for the characterisation of amorphous semiconductors. The Fourier transform DOS calculation method allows unlocks the potential of the TPC experiment as an easily used, accurate, wide energy range DOS probe. The method has a particular potential usefulness for profiling the densities of defect states, for example in experiments involving the creation and annealing of metastable states. Varying the wavelength and absorption depth of the excitation light would give the method depth resolution and allow surface or interface states and bulk states to be distinguished. The method is not restricted to use with materials having distributed densities of localised state. In principle it could be applied to characterise the narrow distributions of defect states in crystalline semiconductors.

There are a number of questions arising from the measurements with optical bias on undoped a-Si:H. The recombination coefficient C_R obtained from TPC with optical bias exhibiting undershoot disagrees with the capture coefficient for defect states indicated by the proposed model to match the MPC measurements. However the degree of variation in the values for C_R in chapter 7 makes the conclusion that C_R is around $1\text{-}3\times10^{-8}cm^3s^{-1}$ unsatisfactory. The Pandya and Schiff analysis needs to be extended to a DOS with a bump of states with a different capture coefficient to see if this accounts for the variation. The undershoot is worth further investigation because it is such a clearly observable feature potentially giving information on trapping and recombination processes, for example the major recombination path. The sublinear variation of B with ω in the DOS independent régime also deserves attention. Since neither of the single valence state treatments examined in this work account for the observed variation the next step would be to examine the solution for correlated states published by Longeaud and Kleider.

Further work on a-As_2Se_3 would be facilitated by an increase of the signal magnitude. This could be achieved for example by using interdigitated electrodes. MPC

measurements could then be made at lower mean generation rate to attempt to identify whether the measurements at higher generation rate are DOS independent. TPC measurements could also be made to shorter times and at lower temperature to attempt to observe a deep trapping signature in the decay.

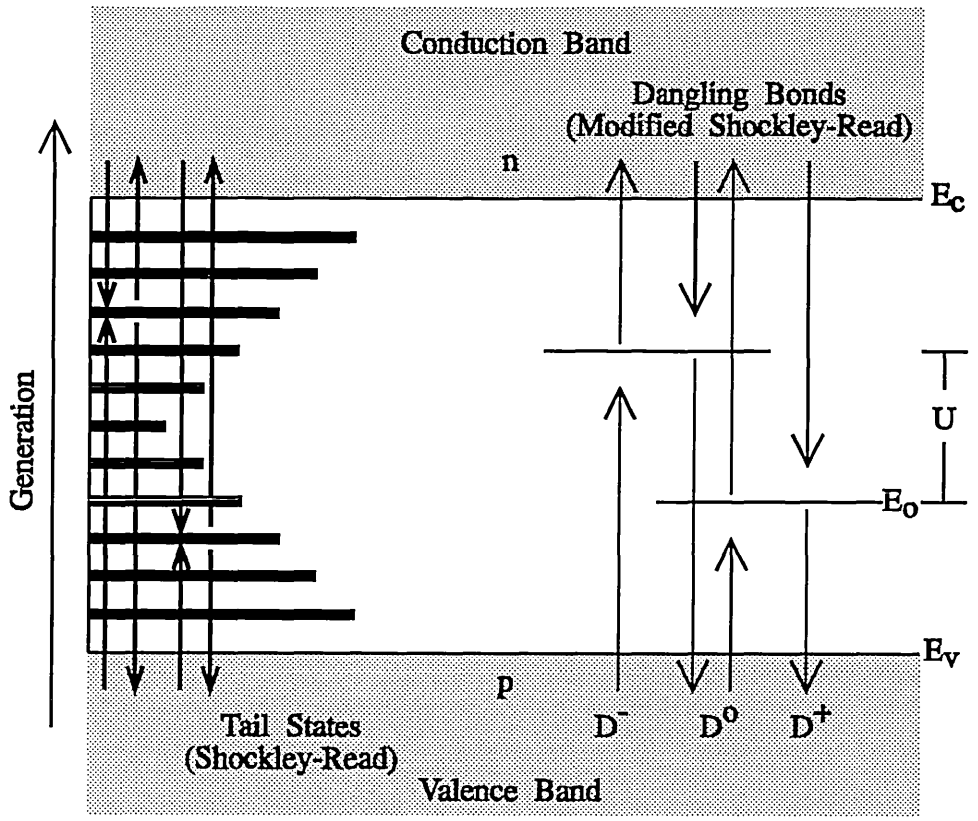

Figure A1 Numerical modelling of multiple trapping photoconductivity: energy level scheme and transitions between states.

Main et al (1991) describe the method used in this work of numerically simulating multiple trapping transport in a homogeneous semiconductor. In the method the DOS is represented as a number, typically one hundred, of discrete levels of localised states distributed throughout the gap, see figure A1. A rate equation for each level describing the electron and hole transitions between the level and the conduction and valence band extended states can be written down, together with the rate equations for the conduction and valence bands themselves. The capture coefficients C_{ni}, C_{pi}, energy E_i and density N_{ti} for each level can be specified individually. If there are N-2 localised levels the result is a set of N coupled non-linear first order differential equations describing the whole system as written below, with y_1=n, the free electron density, y_N=p the free hole density, y_i the electron occupation of the 'i'th localised level and $\overline{n}_i$,$\overline{p}_i$ the electron and hole emission terms from detailed balance for the 'i'th level, and G the *excess* generation rate.

For the conduction band:

$$\frac{dy_1}{dt} = -y_1 \sum_2^{N-1} C_{ni}(N_{ti} - y_i) + \sum_2^{N-1} y_i C_{ni} \bar{n}_i + G \qquad \text{(A1)}$$

electron capture electron release

For the 'i'th localised level:

$$\frac{dy_i}{dt} = \left[y_1 C_{ni}(N_{ti} - y_i) - y_i C_{ni} n_{1i}\right] - \left[y_N C_{pi} y_i + C_{pi} \bar{p}_i (N_{ti} - y_i)\right] \qquad \text{(A2)}$$

electron capture electron release hole capture hole release

and for the valence band:

$$\frac{dy_N}{dt} = -y_N \sum_2^{N-1} C_{pi} y_i + \sum_2^{N-1} C_{pi} \bar{p}_i (N_{ti} - y_i) + G \qquad \text{(A3)}$$

hole capture hole release

Modified forms of the rate equations are used to include correlated states (dangling bonds). The requirement for charge conservation completes the equation set.

The system is solved using a matrix time step method, ie; the values of the variables and derivatives at time t_{k+1} are found from their values at time $t_k = t_{k+1} - \Delta t$. However a standard explicit solution; ie: $f(t_{k+1}) = f(t_k) + \Delta t[df/dt\,|_{tk}]$, cannot be used because the time step Δt would have to be of the order of the trapping time into the whole DOS, ie; of the order of picoseconds. Instead an *implicit* solution is used, $f(t_{k+1}) = f(t_k) + \Delta t[df/dt\,|_{tk+1}]$, with the value of $[df/dt\,|_{tk+1}]$ being found to a chosen precision by an iteration. In this way the time step Δt can be allowed to increase as the simulation proceeds.

Using the procedure sketched out above the solutions to the rate equations for all the variables in the system can be found for a variety of excitation conditions. The thermal equilibrium densities are found by setting G=0, making an initial guess for the set of variables, taking short time steps to allow for the initial rapid redistribution of charge and then very long time steps ($\Delta t = 10^{16}$s). The steady state generation rate densities are found by starting from the thermal equilibrium densities and taking very long time steps, the solution being very stable and convergence rapid. TPC is simulated by starting from the thermal equilibrium or steady state solution for TPC with optical bias and introducing an excess number of electrons and holes at t=0. The ensuing relaxation of the charge distribution can be followed by setting the step length Δt to be a fraction of the elapsed time, say a tenth. MPC is simulated by starting from the steady state solution for the mean generation rate and then taking constant time steps of a fraction of the generation

rate sinusoidal variation period, say a fiftieth. The solution usually becomes periodic within two oscillations of the generation rate.

Modelling parameters

The modelling parameters used in this work are as follows:

All simulations:

Valence band tail extends from E_v=0eV to 0.9eV, conduction band tail extends from 0.9eV to E_c=1.8eV, both tails divided into 90 levels. Density of states at E_c and E_v is $4\times10^{21}cm^{-3}eV^{-1}$. Valence band tail consists of an 0.1eV slope exponential extending to E_v. Attempt-to-escape frequencies determined from detailed balance.

Chapter 6, parameters used to produce simulated decays of figures 6.5 and 6.14:

Conduction band tail: $C_n=C_p=10^{-8}cm^3s^{-1}$
Valence band tail: $C_p=C_n=10^{-8}cm^3s^{-1}$

Chapter 6, parameters used to produce simulated decays of figure 6.15:

Conduction band tail: $C_n=10^{-8}cm^3s^{-1}$, $C_p=0$
Valence band tail: $C_p=10^{-8}cm^3s^{-1}$, $C_n=0$
Additional single level of $4.4\times10^{16}cm^{-3}$ dangling bonds located at 0.9eV, with all capture coefficients=$10^{-8}cm^3s^{-1}$, correlation energy=0

Chapter 7, parameters used to produce simulated decays of figures 7.7 and 7.8:

Conduction band tail: $C_n=10^{-8}cm^3s^{-1}$, $C_p=0$
Valence band tail: $C_p=10^{-8}cm^3s^{-1}$, $C_n=10^{-7}cm^3s^{-1}$

Chapter 8, parameters used to produce simulated MPC spectra of figure 8.11

Conduction band tail: $C_n=10^{-8}cm^3s^{-1}$, $C_p=0$
Valence band tail: $C_p=10^{-8}cm^3s^{-1}$, $C_n=10^{-9}cm^3s^{-1}$

Chapter 9, parameters used to produce simulated decay of figure 9.4

Conduction band tail: $C_n=C_p=10^{-8}cm^3s^{-1}$
Valence band tail: $C_p=C_n=10^{-8}cm^3s^{-1}$

Appendix B Treatment for MPC including hole transitions explicitly

Hattori et al (1994) gave a treatment for MPC covering both electron and hole transitions explicitly for a DOS consisting of single valence states. The rate equations are:

$$\frac{dn}{dt} = G - \sum_j \int_{E_v}^{E_c} \left\{ n\left[1 - f^j\right] - \overline{n} f^j \right\} C_n^j g^j dE \qquad \text{(B1)}$$

$$\frac{dp}{dt} = G - \sum_j \int_{E_v}^{E_c} \left\{ p f^j - \overline{p}\left[1 - f^j\right] \right\} C_p^j g^j dE \qquad \text{(B2)}$$

$$\frac{df^j}{dt} = \left[n + \overline{n}\right] C_n^j \left[1 - f^j\right] - \left[p + \overline{p}\right] C_p^j f^j \qquad \text{(B3)}$$

The symbols have the same meaning as in the body of this work, but the rate equations here are formulated in terms of multiple species of states identified by the subscript "j". The linearised solution for the free electron density for a sinusoidal generation rate (definitions as in chapter 3 equations 3.1-3.4) is:

$$\frac{n_\omega}{G_\omega} = \frac{i\omega + P}{(i\omega + N)(i\omega + P) + (i\omega + N)\overline{P} + (i\omega + P)\overline{N}} \qquad \text{(B4)}$$

and for free holes:

$$\frac{p_\omega}{G_\omega} = \frac{i\omega + N}{(i\omega + N)(i\omega + P) + (i\omega + N)\overline{P} + (i\omega + P)\overline{N}} \qquad \text{(B5)}$$

with

$$N = \sum_j \int_{E_v}^{E_c} C_n^j \left[1 - f_{ss}^j\right] g^j \frac{i\omega}{i\omega + R_{ss}^j} dE \qquad \text{(B6)}$$

$$P = \sum_j \int_{E_v}^{E_c} C_p^j f_{ss}^j g^j \frac{i\omega}{i\omega + R_{ss}^j} dE \qquad \text{(B7)}$$

$$\overline{N} = \sum_j \int_{E_v}^{E_c} C_n^j \left[1 - f_{ss}^j\right] g^j \frac{\omega_p^j + \omega_h^j}{i\omega + R_{ss}^j} dE \qquad \text{(B8)}$$

$$\overline{P} = \sum_j \int_{E_v}^{E_c} C_p^j f_{ss}^j g^j \frac{\omega_n^j + \omega_e^j}{i\omega + R_{ss}^j} dE \qquad \text{(B9)}$$

where $\omega_n^j = n_{ss} C_n^j$, $\omega_p^j = p_{ss} C_p^j$, $\omega_e^j = \overline{n} C_n^j$, $\omega_h^j = \overline{p} C_p^j$, and

$$f_{ss}^j = \frac{(n_{ss} + \overline{n}) C_n^j}{(n_{ss} + \overline{n}) C_n^j + (p_{ss} + \overline{p}) C_p^j} = \frac{\omega_n^j + \omega_e^j}{R_{ss}^j} \tag{B10}$$

ie: the steady state Shockley-Read occupation (equation 1.15). Note that n_{ss} and p_{ss} must be determined numerically for a particular DOS and G_{ss}.

The present author reduces equation B4 to a simpler form for a single species of localised states in order to obtain an expression for the behaviour of MPC at small ω. We can neglect the $i\omega$ terms in B4 by comparison with the imaginary parts of N and P except for the very highest frequencies:

$$\frac{n_\omega}{G_\omega} \approx \frac{P}{NP + N\overline{P} + P\overline{N}} \tag{B11}$$

We can also neglect the portions of the integrals in equations B6-B9 for which f_{ss} or $(1-f_{ss})$ is approximately zero. B6 and B8 reduce to integrals between E_c and E_{tp}, in which range ω_h can also be neglected compared with ω_p, and B7 and B9 to integrals between E_{tn} and E_v, in which range ω_e can also be neglected compared with ω_n. From the reduced forms for B6 and B8 we obtain:

$$\frac{\overline{N}}{N} = -i\frac{\omega_p}{\omega} \tag{B12}$$

and from B7 and B9:

$$\frac{\overline{P}}{P} = -i\frac{\omega_p}{\omega} \tag{B13}$$

Substituting B12 and B13 into B11 results in

$$\frac{n_\omega}{G_\omega} = \left[N\left\{1 - \frac{i}{\omega}(\omega_n + \omega_p)\right\}\right]^{-1} \tag{B14}$$

Defining B as in equation 3.5 we can therefore write

$$B(\omega) = \int_{E_{tp}}^{E_c} C_n (1 - f_{ss}) g(E) \frac{\omega_e \omega}{R_{ss}^{\,2} + \omega^2} dE \tag{B15}$$

where $\omega_e = \overline{n} C_n$. For $\omega << \omega_n$ B15 reduces to equation 3.15.

Appendix C Derivation of the time at which $\delta n=\delta n^*$

We define δn^*, δN^* to be the transient free and trapped electron densities at which the two recombination terms in equation 7.7 have equal magnitude and t^* to be the time at which this occurs:

$$\delta n^*(t^*)N_{tss} = n_{ss}\delta N_t^*(t^*) \tag{C1}$$

From equation 2.9 of the "emission rate" treatment for post-recombination TPC we have:

$$\delta n^* \approx \delta f_d kTg\left[E_c - E_{th}(t^*)/kT\right]\tau_R/t^* \tag{C2}$$

We make the approximation that $\delta N_t << N_{tss}$ so that the recombination time is given by:

$$\tau_R \approx 1/(N_{tss}C_R) \tag{C3}$$

We also make the approximation that all states below E_{fn} are full so:

$$\delta N_t^* \approx \delta f_d \int_{E_{fn}}^{E_c-E_{th}} g(E)dE \tag{C4}$$

Then for an exponential tail $g(E) = g_c \exp\left[-(E_c - E)/kT\right]$, substituting C2-C4 into C1 we obtain:

$$t^* = \frac{\alpha}{n_{ss}C_R} \tag{C5}$$

which is independent of δG (as expected for a linear with δG model) but dependent on G_{ss}. Equation C5 gives a steady state generation rate independent energy offset from E_{fn} for E_c-$E_{th}(t^*)$ as was posited and not observed for t_{us} in chapter 7:

$$E_c - E_{th}(t^*) = E_{fn} - kT\ln\left(\frac{C_n\alpha}{C_R}\right) \tag{C6}$$

Note that $\ln(\alpha C_n/C_R)$ is *negative* for $C_R > C_n$.

References

Adler, D and Yoffa, J.Y. 1976. Physical Review Letters, **36**: 1197

Adriaenssens, G.J. Seynhaeve G. and de Greef, S. 1985. Journal of Non-Crystalline Solids, **77&78**: 1187

Antoniadis, H. and Schiff, E.A. 1992. Physical Review B, **46**: 9482

Arkhipov, V.I. and Rudenko, A.I. 1978. Journal of Non-Crystalline Solids, **30**: 163

Biegelsen, D.K. 1981. In: *Nuclear and electron resonance spectroscopies applied to material science*, edited by Kaufmann and Shenoy. Amsterdam: North Holland

Brüggemann, R. Main, C. Berkin, J. and Reynolds, S. 1990. Philosophical Magazine B, **62**: 29

Carasco, F. and Spear, W.E. 1983. Philosophical Magazine B, **47**: 495

Deane, S.C. and Powell, M.J. 1993. Physical Review Letters, **70**: 1654

Dick F. 1994. M.Sc. Thesis, University of Dundee

Han, D. Melcher, D.C. Schiff, E.A. and Silver, M. 1993. Physical Review B, **48**: 8658

Hattori, K. Niwano, Y. Okamoto, H. and Hamakawa , Y. 1991. Journal of Non-Crystalline Solids, **137&138**: 363

Hattori, K Adachi, Y. Anzai, M. et al 1994. Journal of Applied Physics, **76**: 2841

Jackson, W.B. and Amer, N.M. 1982. Physical Review B, **25**: 5559

Jackson, W.B. Kelso, S.M. Tsai, C.C. et al 1985. Physical Review B, **31**: 5187

Juška, G. Kočka , J. Vili ũnas, M. and Arlauskas, K. 1993. Journal of Non-Crystalline Solids, **164-166**: 579

Keithley Instruments 1992. *Low level measurements*

Ley L. 1984. In: *The physics of hydrogenated amorphous silicon II*, edited by J.D.Joannopoulos and G.Lucovsky. Berlin: Springer-Verlag

Longeaud, C. and Kleider, J.P. 1993. Physical Review B, **48**: 8715

Mackenzie, K.D. LeComber, P.G. and Spear, W.E. 1982. Philosophical Magazine, **46**: 377

Main, C. 1988. Unpublished

Main, C. and Owen, A.E. 1972. In: *Electronic and structural properies of amorphous semiconductors*, edited by P.G.LeComber and J.Mort. London: Academic Press

Main, C. Berkin, J. and Merazga, A. 1991. In: *New physical problems in electronic materials*, edited by M.Borissov, N.Kirov, J.M.Marshall and A.Vavrek. Singapore: World Scientific, 55

Main, C. Brüggemann, R. Webb, D.P. and Reynolds, R. 1992. Solid State Communications, **83**: 401

Marshall, J.M. and Main, C. 1983. Philosophical Magazine B, **47**: 471

Marshall J.M. Berkin, J. and Main C. 1987. Philosophical Magazine B, **56**: 641

Melcher, D. and Schiff, E.A. (unpublished)

Merazga, A. 1990. Ph.D. Thesis, Dundee Institute of Technology

Michiel, H. Marshall, J.M. and Adriaenssens, G.J. 1983. Philosophical Magazine B, **48**: 187

Mourchid, A. Vanderhaghen, R. Hulin, D. Fauchet, P.M. 1990. Physical Review B, **42**: 7667

Mott,N.F. and Davis, E.A. 1979. *Electronic processes in non-crystalline materials*, Oxford: Clarendon press, 15ff

Müller, H.P. and Thomas, P. 1983. Physical Review Letters, **51**: 5337

Oheda, H. 1981. Journal of Applied Physics, **52**: 6693

Okamoto, H. and Hamakawa, Y. 1977. Solid State Communications, **24**:23

Orenstein, J. and Kastner, M.A. 1981. Physical Review Letters, **46**: 1421

Orenstein, J. Kastner, M.A. and Vaninov,V. 1982. Philosophical Magazine B, **46**: 23

Pandya, R. and Schiff, E.A. 1983. Journal of Non-Crystalline Solids, **59&60**: 297

Pandya, R. and Schiff, E.A. 1985. Philosophical Magazine B, **52**: 1075

Rose, A. 1978. *Concepts in photoconductivity and allied problems* (revised ed.), Krieger: New York, 38ff

Schiff, E.A. 1985. In: *Tetrahedrally bonded amorphous semiconductors*, edited by D.Adler and H.Fritzsche, New York: Plenum, 357

Schiff, E.A. 1987. Philosophical Magazine Letters, **55**: 87

Schiff, E.A. Branz, H. Melcher, D.C. et al 1993. Journal of Non-Crystalline Solids, **166**: 331

Schmidlin, F.W. 1977. Physical Review B, **35**: 2363

Schumm, G. and Bauer, G.H. 1989. Journal of Non-Crystalline Solids, **114**: 660

Schumm, G. and Bauer, G.H. 1991. Philosophical Magazine B, **64**: 515

Schumm, G. Jackson, W.B. and Street, R.A. 1993. Physical Review B, **48**: 14198

Seynhaeve, G.F. Barclay, R.F. Adriaenssens G.J. and Marshall, J.M. 1989. Physical Review B, **39**: 10196

Shockley, W. and Read, W.T. 1952. Physical Review, **87**: 835

Spear, W.E. and Steemers, H. 1983. Philosophical Magazine B, **47**: L77

Spiegel, M.R. 1974. *Theory and problems of Fourier analysis with applications to boundary value problems*, New York: McGraw-Hill, 174

Street, R.A. 1991. *Hydrogenated amorphous silicon*, Cambridge: Cambridge University Press, a 21, b 313

Stuke, J. 1987. Journal of Non-Crystalline Solids, **97&98**: 1

Taylor, G.W. and Simmons, J.G. 1972. Journal of Non-Crystalline Solids, **8-10**: 940

Tiedje, T. and Rose, A. 1980. Solid State Communications, **37**: 49

Wake, D.R. and Amer, N.M. 1983. Physical Review B, **27**: 2598

Wake, D.R. and Amer, N.M. 1983. Journal of Non-Crystalline Solids, **59&60**: 389

Webb, D.P. 1990. M.Sc. thesis, University of Dundee

Weiser, K. and Ritter, D. 1988. In: *Amorphous silicon and related materials*, edited by H.Fritzsche. Singapore: World Scientific, 871

Winer, K. 1990. Physical Review B, **41**: 12150

Winer, K. and Ley, L. 1989. In: *Amorphous silicon and related materials*, edited by H.Fritzsche. Singapore: World Scientific, 365

Publications and conference presentations arising from this work

Publications

" Techniques for the analysis of transient and modulated photoconductivity in disordered semiconductors"
C.Main, D.P.Webb and S.Reynolds
Proceedings to be published
Eighth International School on Condensed Matter Physics, Varna, Bulgaria 1994

" Transient photoconductivity as a probe for the density of defect states in amorphous silicon: evaluation of a Fourier transform analytical technique"
D.P.Webb, C. Main, R. Brüggemann, and S. Reynolds
Proceedings to be published
12th European Photovoltaic Solar Energy Conference, Amsterdam, The Netherlands 1994

" Time and frequency domain studies of photoconductivity in amorphous semiconductors"
C. Main, R. Brüggemann, D.P. Webb and S. Reynolds
Journal of Non-Crystalline Solids (1993), 164-166, pp 481-484
15th International Conference on Amorphous Semiconductors - Science and Technology, Cambridge, U.K. 1994

" Determination of gap-state distributions in amorphous semiconductors from transient photocurrents using a Fourier transform technique"
C. Main, R. Brüggemann, D.P. Webb and S. Reynolds
Solid State Communications (1992), 83, 6, pp 401-405

" Modulated and transient photoconductivity in a-As_2Se_3 "
C. Main, D.P.Webb, R. Brüggemann and S. Reynolds
Journal of Non-Crystalline Solids (1991), 137 & 138, pp 951-954
14th International Conference on Amorphous Semiconductors - Science and Technology, Garmisch-Partenkirchen, FRG 1991

Conference presentations without published proceedings

" Computer Modelling - photoresponse of a-Si:H p.i.n. devices"
C. Main, D.P.Webb, S. Reynolds and R. Brüggemann
Chelsea Amorphous and Liquid Semiconductors Meeting, 1993

" Transient and modulated photoconductivity in amorphous semiconductors: a synthesis"
C. Main, R. Brüggemann, D.P. Webb and S. Reynolds
Conference on Condensed Matter and Materials Physics, Sheffield 1992

" Frequency and time-resolved photoconductivity studies on a-As_2 Se_3"
C. Main, D.P.Webb, R. Brüggemann and S. Reynolds
Chelsea Amorphous and Liquid Semiconductors Meeting, 1991